



**POLITECNICO**  
MILANO 1863

SCUOLA DI INGEGNERIA INDUSTRIALE  
E DELL'INFORMAZIONE

# Modelling Strategies for Non-Invasive Assessment of Coronary Fractional Flow Reserve

TESI DI LAUREA MAGISTRALE IN  
BIOMEDICAL ENGINEERING - INGEGNERIA BIOMEDICA

Author: **Giulia Frigerio**

Student ID: 968914

Advisor: Prof. Alberto Redaelli, PhD

Co-advisor: Guido Nannini, MSc

Academic Year: 2021-22



# Contents

<b>Contents</b>	<b>i</b>
<b>Acronyms</b>	<b>v</b>
<b>List of Figures</b>	<b>ix</b>
<b>List of Tables</b>	<b>xv</b>
<b>Abstract</b>	<b>xix</b>
<b>Abstract in lingua italiana</b>	<b>xxi</b>
<b>1 Introduction</b>	<b>1</b>
1.1 Anatomy and Physiology of the Cardiovascular System . . . . .	1
1.1.1 The Heart . . . . .	1
1.1.2 Blood Vessels . . . . .	3
1.2 Coronary Arteries . . . . .	3
1.2.1 Physiology of the Coronary Arteries . . . . .	4
1.2.2 Pathologies of the Coronary Arteries . . . . .	4
1.2.3 Atherosclerosis . . . . .	5
1.3 Overview of Current Techniques to Diagnose and Treat CAD . . . . .	5
1.3.1 Fractional Flow Reserve . . . . .	8
1.4 Available Treatments . . . . .	10
1.4.1 Percutaneous Coronary Intervention or Angioplasty . . . . .	11
1.4.2 Coronary Artery Bypass Graft Surgery . . . . .	12
1.4.3 Treatment Choice Criteria . . . . .	12
1.5 Future Diagnostic Strategy . . . . .	12
<b>2 State of the Art</b>	<b>17</b>
2.1 Related Works . . . . .	19

2.1.1	Segmentation and Meshing . . . . .	19
2.1.2	Assumptions on Coronary Flow . . . . .	19
2.1.3	Boundary Conditions . . . . .	20
2.1.4	Post-processing . . . . .	21
2.2	Boundary Conditions . . . . .	25
2.3	Results . . . . .	27
2.3.1	Impact of Geometry . . . . .	28
2.3.2	Impact of Flow Partition Criteria . . . . .	29
2.3.3	Impact of LPM used as Outlet BC . . . . .	30
2.3.4	Other Hemodynamic Indices . . . . .	31
2.3.5	Impact of Blood Viscosity . . . . .	34
2.3.6	Conclusions on Literature Review . . . . .	34
2.4	Aim of the Thesis . . . . .	35
<b>3</b>	<b>Materials and Methods</b>	<b>37</b>
3.1	Ideal Geometry . . . . .	39
3.1.1	Boundary Conditions . . . . .	40
3.1.2	Computational Scheme and Parameters . . . . .	41
3.2	Patient-Specific Geometry . . . . .	42
3.2.1	CT-image Acquisition . . . . .	42
3.2.2	CT-image Segmentation and 3D Anatomy Reconstruction . . . . .	42
3.2.3	Meshing . . . . .	45
3.2.4	Material Properties . . . . .	45
3.2.5	Boundary Conditions . . . . .	45
3.2.6	CFD Simulations . . . . .	52
3.2.7	Post-Processing . . . . .	54
<b>4</b>	<b>Results</b>	<b>55</b>
4.1	Idealized Geometry . . . . .	55
4.2	Patient-Specific Geometry . . . . .	59
4.2.1	Sensitivity Analysis . . . . .	59
4.2.2	Patient-Specific Geometry with BCs Estimated from Average Population Data . . . . .	61
4.2.3	Patient-Specific Geometry with BCs based on Patient-Specific Data . . . . .	67
<b>5</b>	<b>Discussion</b>	<b>73</b>
<b>6</b>	<b>Conclusions</b>	<b>79</b>

<b>Bibliography</b>	<b>81</b>
<b>A Appendix A</b>	<b>91</b>
<b>B Appendix B</b>	<b>103</b>
<b>Acknowledgements</b>	<b>109</b>



# Acronyms

**2WK:** 2 Element Windkessel

**3WK:** 3 Element Windkessel

**ACS:** Acute Coronary Syndrome

**ATP:** Adenosine Triphosphate

**AUC:** Area Under the Curve

**BCs:** Boundary Conditions

**BSA:** Body Surface Area

**C:** Compliance

**CABG:** Coronary Artery Bypass Graft

**CAD:** Coronary Artery Disease

**CCTA:** Computed Tomography Coronary Angiography

**CFD:** Computational Fluid Dynamics

**CFR:** Coronary Flow Reserve

**CO:** Cardiac Output

**CT:** Coronary Tomography

**CTP:** stress Computed Tomography Perfusion

**CVDs:** Cardiovascular Diseases

**DBP:** Diastolic Blood Pressure

**FFR:** Fractional Flow Reserve

**FFR<sub>CT</sub>:** Fractional Flow Reserve Computed Tomography

**FFR<sub>SS</sub>:** Steady-State Fractional Flow Reserve

**FFR<sub>T</sub>**: Transient Fractional Flow Reserve

**GCI**: Grid Convergence Index

**HR**: Heart Rate

**HU**: Hounsfield unit

**ICA**: Invasive Coronary Angiography

**iFFR**: Invasive Fractional Flow Reserve

**iFR**: Instantaneous Wave-Free Ratio

**IVUS**: Intravascular Ultrasound

**L**: Impedence

**LAD**: Left Anterior Descending

**LCA**: Left Coronary Artery

**LCX**: Left Circumflex

**LL**: Lesion Length

**LM**: Left Main

**LPM**: Lumped Parameter Model

**LVM**: Left Ventricular Mass

**LVSV**: Left Ventricular Stroke Volume

**MI**: Myocardial Infarction

**ML**: Machine Learning

**MLD**: Minimum Lumen Diameter

**MRI**: Magnetic Resonance Imaging

**NSEs**: Navier-Stokes Equations

**OCT**: Optical Coherence Tomography

**PCI**: Percutaneous Coronary Intervention

**PDEs**: Partial Differential Equations

**PET**: Positron Emission Tomography



**QFR:** Quantitative Flow Ratio

**R:** Resistance

**SA:** Sinatrial

**SBP:** Systolic Blood Pressure

**SIMPLE:** Semi-Implicit Method for Pressure Linked Equations

**SV:** Stroke Volume

**TAG:** Transluminal Attenuation Gradient

**TCRI:** Total Coronary Resistance Index

**TTE:** Transthoracic Echocardiography

**UDF:** User-Defined Functions

**URF:** Under Relaxation Factors

**US:** United States

**WSS:** Wall Shear Stress



## List of Figures

1.1	Heart internal structure [7]. . . . .	2
1.2	External view of the heart structure and coronary arteries [7]. . . . .	3
1.3	Illustration of the interaction of physiological conditions and biomechanical stresses in the regulation of atherosclerosis. <b>(A)</b> Characteristics of a stable plaque with stable calcification and small lipids pools. Mild narrowing of the lumen without disturbing the physiological blood flow. <b>(B)</b> Rupture-prone vulnerable plaque with a large lipid-rich necrotic core, neovascularization, spotty calcium, thin fibrous cap and presence of inflammatory cells. Severe narrowing that can lead to ischemia. The lesion also causes endothelial shear stress variations proximally and distally to the plaque [16].	6
1.4	Atherosclerotic plaques seen from CCTA images. Extraction of coronary arteries plaque from CT images is usually based on difference in attenuation value. <b>(A) Calcified plaque.</b> It is easy to extract due to high attenuation value. The brightness of the plaque could affect the neighbouring pixels creating a blooming effect and thus overestimating the calcification size. <b>(B) Non-calcified plaque.</b> The contrast in grayscale values between plaques, arterial walls and surrounding tissue is very low. To accurately separate the plaque from the surrounding tissue the morphological properties of the non-calcified plaques need to be considered [35]. It is still a challenge to differentiate between fibrotic and lipidic plaques. The two images are taken from the dataset used in this study. . . . .	8
1.5	<b>(A)</b> Schematic representation of the pressure wire used in the ICA during the pullback procedure. Pa and Pd are respectively the aortic (i.e.proximal) and distal pressure.[50]. <b>(B)</b> Pressure recordings during the invasive FFR measurement. Data from a patient present in the dataset of this study. . .	9

- 1.6 (A) Relationship between myocardial blood flow and degree of stenosis [68]. (B) Simplified representation of a coronary artery stenosis and the supplied myocardium. In this example myocardial perfusion pressure would be 100mmHg if no stenosis were present. Due to the stenosis, pressure has decrease to 70mmHg. Hence, the FFR that represents the fraction of normal maximum flow that is preserved despite the presence of the stenosis is represented by  $(70-0)/(100-0)$ . This means that in this case  $FFR = 0.70$  [51]. 10
- 1.7 Revascularization treatments [20]. (A) Coronary artery stenosis. (B) Revascularization through angioplasty with stent. (C) Coronary artery bypass graft surgery. (D) Invasive coronary angiography or ICA. . . . . 11
- 1.8 Results of iFFR and non-invasive  $FFR_{CT}$  in patients with mild, intermediate and severe stenosis. Agreement between the two methods in detecting which stenosis are ischemia causing ( $FFR \leq 0.80$ ). [48] . . . . . 15
- 1.9 (A) Example of an HeartFlow  $FFR_{CT}$  analysis. (B) In the graph in shown the superiority of Precision Pathway ( $FFR_{CT}$  analysis) with respect to the Traditional Testing consisting in the functional stress testing and Invasive Coronary Angiography. HeartFlow  $FFR_{CT}$  demonstrated to significantly reduce all-cause of death, nonfatal MI or catheterization without obstructive disease at 1 year. . . . . 16
- 2.1 Main steps required to perform an  $FFR_{CT}$  analysis. CT images acquisition followed by image segmentation and reconstruction of the 3D anatomical model. Later a mathematical model of the coronary physiology is created and appropriate boundary conditions must be imposed at the outlet surfaces of the domain. Finally the governing equations of fluid-dynamics are solved and  $FFR_{CT}$  value is estimated during the post-processing. . . . . 17
- 2.2 Different LPM adopted as outlet BC. (A) RCRCR model by Boileau et al. [6] with the contribution of the intramyocardial pressure. (B) 2WK model adopted by Lo et al [38]. In this case the contribution of intramyocardial pressure is considered only in the left coronary artery as in the right side of the heart the pressure exerted by the ventricle is lower. (C) Closed-loop model proposed by Kim et al [29], the first group to use a LPM to model the outlet BC in a coronary artery tree. . . . . 26
- 2.3 Comparison between iFFR, obtained by ICA, and  $FFR_{CT}$  in both the models with and without the aorta. The reported results are representative cases for mild (a), intermediate(b) and severe(c) stenosis. In all degree of stenosis a good correlation is shown [33]. . . . . 28

2.4	Correlation between $FFR_{CT}$ obtained by the 1D and 3D geometry. (A) Model used by Yin et al [77], considering aorta, LCA and RCA. (B) Boileau et al. [6] results for two different degrees of stenosis. Both the works demonstrated that also the 1D model is able to reproduce accurate results.	29
2.5	Results obtained from the simulations run using TAG as a method to distribute the flow-rate in the coronary subbranches. (A) CT-image, (B) $FFR_{CT}$ map on the coronary tree, (C) ICA image and (D) invasive measured FFR obtained using the pressure-wire and pullback procedure. The results obtained by the computational model agree with the invasive measurement [64].	30
2.6	Comparison between the results obtained by a steady-state or transient simulation with respect also to invasive measured FFR. Both the simulations showed similar results meaning that a simpler and less computational demand model could be used to evaluate the severity of a coronary stenosis.	31
2.7	$FFR_{CT}$ for different % stenosis. The influence of the studied parameters in the uncertainty of FFR values is shown. As can be seen, MLD exhibit the highest sensitivity for stenosis >50%.	32
2.8	Influence of diameter reduction(%), LL and MLD on the different hemodynamic parameters (FFF, iFR and CFR). As can be seen from the reported graphs, the indices decreases with an increase in diameter reduction and LL and a decrease in MLD [62].	33
3.1	Summary of the different models and BCs investigated.	39
3.2	Mesh of the ideal geometry with a 50% of stenosis. (a) shows the mesh boundary layer in the inlet section. (b) shows the refinement of the mesh in the stenosis region.	40
3.3	Ideal geometry with specified the imposed boundary conditions for either the steady or transient simulation.	40
3.4	3WK LPM imposed as outlet boundary condition.	41
3.5	Workflow adopted to estimate the $FFR_{CT}$ starting from medical CT images. (A) CCTA images. (B) Segmentation of LCA (in yellow), RCA (in green) and plaque (in white). (C) 3D model reconstruction. (D) Centre-line extraction. (E) Refined geometry ready to be meshed. (F) Meshed geometry. (G) Imposition of appropriate boundary conditions. (H) CFD simulations and (I) analysis of the obtained results. (I) represents the FFR map for a patient with a severe degree if stenosis.	43

3.6	Difference between calcified (on the left) and non-calcified plaque (on the right) in CT-images from the dataset used in this study. . . . .	44
3.7	Inlet surface of a patient-specific coronary geometry. The applied mesh had a max element size of 0.1 mm. . . . .	45
3.8	( <b>A</b> ) Pressure-curve imposed at the inlet BC when using average literature data. ( <b>B</b> ) Approximation of the pressure-curve with Fourier coefficients. . .	46
3.9	Inlet and outlet BC assigned at the boundaries of the domain in the transient simulations. Specifically, a pressure curve at the inlet surface and a 3WK model at the outlet boundaries. . . . .	47
4.1	Comparison between the FFR maps generated by steady and transient simulations, for progressively increasing degrees of stenosis. . . . .	56
4.2	Comparison of vorticity (steady-state vs transient simulation) for the different levels of disease. The figure displays streamlines and highlights vorticity values in a cross-sectional plane located within the stenosis region. . . . .	58
4.3	Sensitivity mesh analysis results. . . . .	59
4.4	The mesh used had an element size of 0.1 mm, and an analysis of the element metrics was conducted. The metrics evaluated were Aspect Ratio, Orthogonal Quality, and Skewness, with the results displayed in a top-to-bottom order. A good mesh quality was indicated by an aspect ratio of approximately 3, an orthogonal quality near 1, and a skewness close to 0. .	60
4.5	Comparison between $FFR_{CT}$ maps obtained from steady-state and transient simulation. The relative difference between the two is illustrated in the last column. . . . .	65
4.6	Comparison between vorticity generated by steady-state and transient simulations. Particular attention is given to the highest value detected in the cross-sectional plane located at the stenosis center. . . . .	66
4.7	Comparison between the $FFR_{CT}$ map obtained using the first ( <b>A</b> ) and the second approach ( <b>B</b> ) for estimating inlet coronary flow-rate. . . . .	68
4.8	CFD-derived FFR for both steady-state and transient simulations run using patient-specific BCs. . . . .	71
B.1	Pressure field obtained in the idealized geometry with varying degrees of stenosis. . . . .	104
B.2	Velocity field obtained in the idealized geometry with varying degrees of stenosis. . . . .	105
B.3	Pressure field obtained in the patient-specific geometry for the four analysed patients. BCs were derived from average literature data. . . . .	106

B.4 Pressure field obtained in the patient-specific geometry for the four analysed patients. BCs were derived from the available patient-specific data. . . 107





## List of Tables

1.1	Comparison between ICA and CCTA imaging modalities. Main advantages and disadvantages. ICA image from [15] and CCTA image from the dataset used in this study. . . . .	7
2.1	Analysed works. For each study are reported: imaging modality from which the segmentation has been performed, reduced-order model, anatomical geometries that have been considered, steady-state or transient simulation, BCs imposed at the inlet and outlet surfaces and indexes that have been analysed. The subscripts denote which works belong to the same research group. (Pmyo: intramyocardial pressure, Pv: venous pressure, OSI: oscillatory shear index, TAWSS: time-average wall shear stress, RRT: relative resistance time, TAP: time-average pressure). . . . .	24
3.1	Patients with related iFFR measurement. Patients were subdivided according to the degree of stenosis. From severe to mild: $FFR \leq 0.7$ (red), $0.70 < FFR < 0.80$ (orange), $0.80 < FFR < 0.90$ (yellow), $FFR \geq 0.90$ (green). One patient from each group was randomly selected. . . . .	38
3.2	Available patient-specific data. . . . .	49
3.3	Available patient-specific data. . . . .	49
3.4	Simulation settings. . . . .	53
4.1	Boundary conditions imposed at the inlet and outlet surface of the idealized geometry. Pressure, resistance and compliance are respectively in $mmHg$ , $Pa \cdot s/m^3$ and $m^3/Pa$ . . . . .	56
4.2	Inlet flow-rate resulting from the steady-state and transient simulations. Q-Transient is the average value calculated over the last cycle. The reported values are in $m^3/s$ . . . . .	56
4.3	Highest value of vorticity found in the cross-sectional plane positioned at the center of the stenosis. . . . .	57

4.4	Optimized resistance and compliance values for Patient-1, using BCs based on average-population data. The values are reported for each outlet branch. Resistances and compliance are respectively in $Pa \cdot s/m^3$ and $m^3/Pa$ . . . .	62
4.5	Optimized resistance and compliance values for Patient-6, using BCs based on average-population data. The values are reported for each outlet branch. Resistances and compliance are respectively in $Pa \cdot s/m^3$ and $m^3/Pa$ . . . .	62
4.6	Optimized resistance and compliance values for Patient-9, using BCs based on average-population data. The values are reported for each outlet branch. Resistances and compliance are respectively in $Pa \cdot s/m^3$ and $m^3/Pa$ . . . .	63
4.7	Optimized resistance and compliance values for Patient-10, using BCs based on average-population data. The values are reported for each outlet branch. Resistances and compliance are respectively in $Pa \cdot s/m^3$ and $m^3/Pa$ . . . .	63
4.8	Inlet pressure and flow-rate for both the steady-state and transient simulations. Pressure is in $mmHg$ while flow-rate is in $m^3/s$ . . . . .	64
4.9	Comparison between the $FFR_{CT}$ values obtained from steady-state and transient simulations, with the relative error between the two displayed in the last column. . . . .	65
4.10	Highest value of vorticity found in the cross-sectional plane positioned at the center of the stenosis (Patient-specific geometry with BCs based on average population data). . . . .	67
4.11	Inlet pressure and flow-rate for both steady-state and transient simulations.	68
4.12	Optimized resistance and compliance values for Patient-1, using BCs based on patient-specific data. The values are reported for each outlet branch. Resistances and compliance are respectively in $Pa \cdot s/m^3$ and $m^3/Pa$ . . . .	69
4.13	Optimized resistance and compliance values for Patient-6, using BCs based on patient-specific data. The values are reported for each outlet branch. Resistances and compliance are respectively in $Pa \cdot s/m^3$ and $m^3/Pa$ . . . .	69
4.14	Optimized resistance and compliance values for Patient-9, using BCs based on patient-specific data. The values are reported for each outlet branch. Resistances and compliance are respectively in $Pa \cdot s/m^3$ and $m^3/Pa$ . . . .	70
4.15	Optimized resistance and compliance values for Patient-10, using BCs based on patient-specific data. The values are reported for each outlet branch. Resistances and compliance are respectively in $Pa \cdot s/m^3$ and $m^3/Pa$ . . . .	70
4.16	Comparison of the obtained $FFR_{CT}$ from steady-state and transient simulations against the iFFR. The highlighted columns indicate the relative difference, important to validate the model, while the last column displays the agreement between $FFR_{CT}$ and iFFR. . . . .	72

A.1 Authors using a model comprising Aorta, LCA and RCA. The subscripts denote which works belong to the same research group. (Pmyo: intramyocardial pressure, Pv: venous pressure, OSI:oscillatory shear index, TAWSS: time-average wall shear stress, RRT: relative resistance time, TAP: time-average pressure). . . . . 93

A.2 Authors using a more simplified model without the aorta. The subscripts denote which works belong to the same research group. (Pmyo: intramyocardial pressure, Pv: venous pressure, OSI:oscillatory shear index, TAWSS: time-average wall shear stress, RRT: relative resistance time, TAP: time-average pressure). . . . . 95

A.3 Works in which a comparison of  $FFR_{CT}$  against iFFR have been performed. The subscripts denote which works belong to the same research group. (Pmyo: intramyocardial pressure, Pv: venous pressure, OSI:oscillatory shear index, TAWSS: time-average wall shear stress, RRT: relative resistance time, TAP: time-average pressure). . . . . 97

A.4 Analysed works in which a steady-state simulation was used to estimate  $FFR_{CT}$  value. The subscripts denote which works belong to the same research group. (Pmyo: intramyocardial pressure, Pv: venous pressure, OSI:oscillatory shear index, TAWSS: time-average wall shear stress, RRT: relative resistance time, TAP: time-average pressure). . . . . 99

A.5 Analysed works in which a Transient simulation was used to estimate  $FFR_{CT}$  value. The subscripts denote which works belong to the same research group. (Pmyo: intramyocardial pressure, Pv: venous pressure, OSI:oscillatory shear index, TAWSS: time-average wall shear stress, RRT: relative resistance time, TAP: time-average pressure). . . . . 101



# Abstract

**Introduction:** Coronary artery disease (CAD) is the leading cause of death globally. Invasive fractional flow reserve (iFFR) measurement is the gold standard technique for CAD severity assessment. Advancement in medical imaging and computational fluid dynamics (CFD) technique have led to the development of a non-invasive diagnostic tool: computed tomography (CT)-derived FFR ( $FFR_{CT}$ ). This work aimed to test CFD techniques for coronary flow simulation and explore simple models for accurate  $FFR_{CT}$  computation. **Methods:** Three incrementally more complex scenarios were simulated, for each of which mild to severe stenosis were considered: *i*) Idealized stenosis geometries coupled to boundary conditions (BCs) based on average population data; *ii*) Patient-specific geometries reconstructed from CT, coupled with both average population and *iii*) patient-specific BCs. The feasibility of using a less expensive steady-state rather than a transient simulation was investigated. The developed model was validated by comparing the computed  $FFR_{CT}$  against the iFFR clinically measured. In all simulated models a pressure waveform was set as BC at the inlet and a 0-D Windkessel model was coupled at the outlets. **Results:** As the degree of stenosis increased, steady simulations in the idealized geometries scenario yielded significantly lower FFR results compared to transient ones (maximum difference was 52.6%). Additionally, an increase in the obstruction level resulted in a corresponding rise in the difference between the maximum vorticity observed in the two simulation approaches. Contrary, in the patient-specific geometry scenarios, the maximum difference between the two obtained  $FFR_{CT}$  resulted to be less than 1% in all patients. No significant difference in vorticity was found. A good agreement was established between  $FFR_{CT}$  and iFFR for patients with a CAD in the right branch ( $\epsilon_r \leq 6.5\%$ ), while a larger difference was observed for patients with a stenosis in the left branch (10-20%). **Conclusions:** Steady-state simulations provides  $FFR_{CT}$  estimation comparable to transients ones, with the same BCs. The proposed method provides  $FFR_{CT}$  in good agreement with iFFR for patients presenting a stenosis in the right branch, while more elaborated models may be necessary for patients with CAD in the left branch.

**Keywords:** Atherosclerosis, Computational Fluid-Dynamics, Coronary Hemodynamic, CT-based Fractional Flow Reserve, Patient-specific Model



## Abstract in lingua italiana

**Introduzione:** La coronaropatia (CAD) è la principale causa di morte a livello globale. La misura invasiva della riserva frazionale di flusso (iFFR) è il gold standard per la valutazione della gravità della CAD. I progressi dell'imaging medico e della fluidodinamica computazionale (CFD) hanno portato allo sviluppo di uno strumento diagnostico non invasivo: FFR derivata dalla tomografia computerizzata (TC) ( $FFR_{CT}$ ). Questo lavoro mira a testare tecniche CFD per la simulazione del flusso coronarico e ad esplorare modelli semplici per una stima accurata dell' $FFR_{CT}$ . **Metodi:** Sono stati simulati tre scenari progressivamente più complessi, ciascuno considerando stenosi da lievi a gravi: *i*) geometrie idealizzate con condizioni al contorno (BC) basate su dati medi della popolazione; *ii*) geometrie paziente-specifiche ricostruite dalla TC, accoppiate a BC sia medie della popolazione che *iii*) paziente-specifiche. È stata valutata la possibilità di utilizzare simulazioni stazionarie, meno costose, anziché transitorie. Il modello sviluppato è stato convalidato confrontando la  $FFR_{CT}$  calcolata, con la iFFR. In tutti i modelli simulati sono stati imposti una forma d'onda di pressione come BC all'ingresso e un modello Windkessel 0-D alle uscite. **Risultati:** Considerando le geometrie idealizzate, all'aumentare del grado di stenosi, la FFR è significativamente inferiore nelle simulazioni stazionarie rispetto a quelle transitorie (differenza massima del 52.6%). All'aumentare del livello di ostruzione, aumenta anche la differenza tra la massima vorticità osservata con i due metodi di simulazione. Al contrario, nella geometria paziente-specifica, la differenza massima tra le due  $FFR_{CT}$  ottenute risulta inferiore all'1% in tutti i pazienti. Non è stata riscontrata alcuna differenza significativa nella vorticità. È stato osservato un buon accordo tra  $FFR_{CT}$  e iFFR per i pazienti con CAD nel ramo destro ( $\epsilon_r \leq 6.5\%$ ), mentre è stata osservata una differenza maggiore per i pazienti con stenosi nel ramo sinistro (10-20%). **Conclusioni:** Le simulazioni allo stato stazionario forniscono stime di  $FFR_{CT}$  paragonabili a quelle in transitorio, considerando le stesse BC. Il metodo proposto fornisce  $FFR_{CT}$  in buon accordo con l'iFFR per i pazienti che presentano una stenosi nel ramo destro, mentre per i pazienti con CAD nel ramo sinistro potrebbero essere necessari modelli più elaborati.

**Parole chiave:** Aterosclerosi, Fluidodinamica Computazionale, Emodinamica Coronarica, Riserva Frazionale di Flusso basata su TC, Modello Paziente-Specifico





# 1 | Introduction

## 1.1. Anatomy and Physiology of the Cardiovascular System

The cardiovascular system is an hydraulic system and consists of a pump, the heart, and a network of tubes, the blood vessels. Its main purpose is to deliver oxygen, nutrients, hormones, cells of the immune system, and other substances to body tissues and remove waste products of cellular metabolism [25]. Blood flow through the wide vascular network is achievable only with the aid of sufficient pressure exerted on the blood vessels by the pumping action of the heart [7]. The system is subdivided into two main loops: the small and the greater circulation. The small circulation is the pulmonary one and allows the oxygenation of blood, while the greater one is the systemic circulation; it provides oxygenated blood and nutrients to the whole body. The right atrium receives blood from the systemic circulation and the right ventricle pumps it in the pulmonary circulation; the left atrium accumulates blood from the pulmonary circulation and the left ventricle sends it to the systemic circulation[41].

### 1.1.1. The Heart

All the functions of the cardiovascular system depend on the heart. The heart is a complex organ that pumps blood through the body thanks to a system of chambers, valves, and muscles. It guarantees a consistent and uninterrupted flow of blood [7]. It is a muscle organ that contracts about 100.000 times a day; each year the heart pumps about 7.5 million litres of blood [41]. The heart's pumping action is controlled by electrical impulses that originate in the sinoatrial(SA) node, a specialized group of cells in the right atrium. These impulses cause the heart muscle to contract in a coordinated way, resulting in the rhythmic beating of the heart.

The wall of the heart is made up of three layers: the pericardium, the myocardium, and the endocardium (from outside to inside). The myocardium is the middle layer of the heart wall and the thickest one. It is also referred to as the cardiac muscle because its muscular

contractions facilitate the ejection of blood from the heart chambers. The cardiac muscle cells are small cells called cardiomyocytes. These cells are dependent on aerobic respiration for Adenosine Triphosphate (**ATP**) synthesis necessary for the contraction.

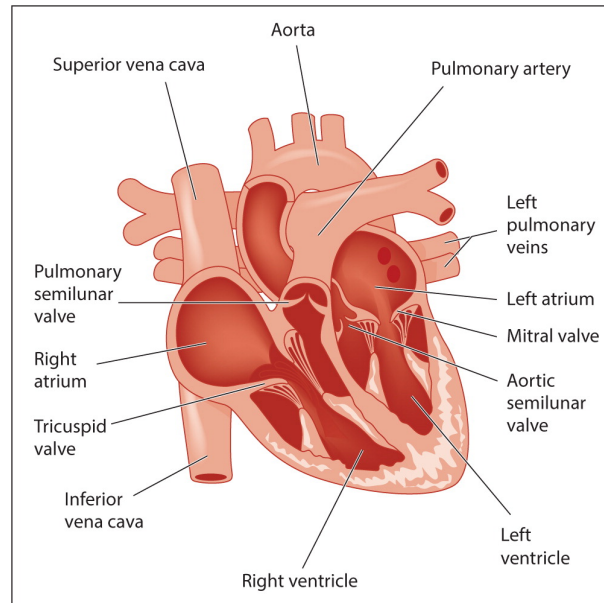


Figure 1.1: Heart internal structure [7].

The heart is a four-chamber organ consisting of the right atrium and ventricle, as well as the left atrium and ventricle. (**Figure 1.1**). The chambers work together to guarantee the pumping of the blood through an extent network of blood vessels that connect the heart and the peripheral tissues. A septum between the left and right sides prevents the oxygen-rich blood of the left-hand side of the heart from mixing with the deoxygenated blood of the right-hand side of the heart [7].

One-way blood flow through the heart is ensured by the four heart valves as well as the pressure gradients that they maintain. The valves open and close passively due to a through-valve pressure gradient. Pulmonary and aortic valve separate the ventricle from the pulmonary artery and the aorta, respectively. Mitral, and tricuspid valve are located between the atria and ventricle.

The cardiac cycle is the period comprised between the beginning of two heartbeats. It comprised alternating period of contraction and relaxation. When the ventricles relax (diastole) they fill up with blood from the atria, and when the ventricles contract (systole), blood is ejected into circulation. The contraction and relaxation of the myocardial layer is what constitutes the pumping action of the heart [3, 7].

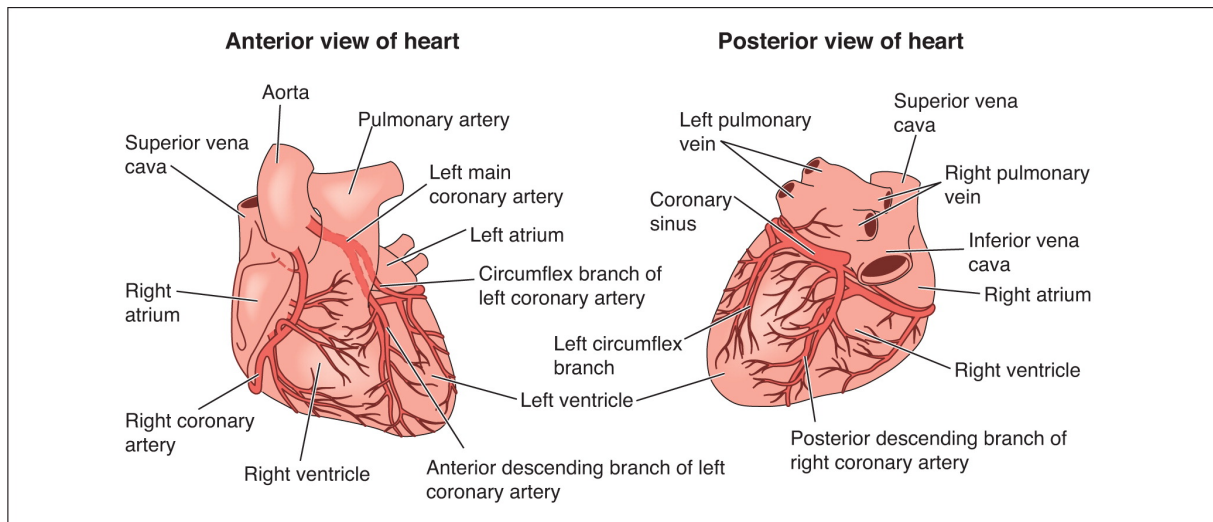


Figure 1.2: External view of the heart structure and coronary arteries [7].

### 1.1.2. Blood Vessels

The blood vessels are the channels through which blood flows and can be subdivided into arteries, veins, and capillaries. Arteries carry blood rich of oxygen and nutrients to the periphery, veins bring deoxygenated blood back to the heart. The capillaries are tiny blood vessels with a thin wall that connect arteries and veins; they are defined as *exchange vessels* as the very thin wall allows the exchange of nutrients, gasses and waste products between blood and surrounding tissues.

## 1.2. Coronary Arteries

Coronary arteries arise from the sinuses of Valsalva and supply blood to the heart muscle. The heart works continuously and the cardiomyocytes need a considerable amount of oxygen and nutrients. Myocardial oxygen demand is approximately  $8 - 10 \text{ ml/min}/100\text{g}$  of tissue [50]. The coronary circulation comprises a large amount of vessels that wrap around the external surface of the heart. Small branches dive into the heart muscle to bring it blood (**Figure 1.2**).

The two main coronary arteries are the left main (**LM**) and right coronary artery (**RCA**). They are the first two branches of the coronary arteries and originates from the aortic root. LM artery supplies blood to most of the left ventricle, a small portion of the right ventricle, to the left atrium and the anterior two thirds of the intraventricular septum. It is then subdivided into left anterior descending (**LAD**) coronary artery, that supplies blood to the front of the left side of the heart and circumflex artery (**LCX**) that encircles

the heart muscle and supplies blood to the outer and back side of the heart. The RCA supplies blood to the right atrium and ventricle and the sinoatrial and atrioventricular nodes that regulate the heart rhythm [41].

### 1.2.1. Physiology of the Coronary Arteries

The heart is the organ that has the highest oxygen consumption and the coronary circulation is responsible for delivering blood to the myocardium meeting its high metabolic activity. The quantity of blood entering the coronary arteries is approximately 4-5% of the cardiac output [50]. An adequate flow rate is of key importance to avoid ischemia and maintain the integrity of the cardiac tissue.

In contrast with the other tissues in which blood flow peaks during systole, due to increased pressure in the aorta, blood flow in the coronary arteries peaks in diastole. This seems paradoxical but it is the result of external compression of the coronary vessels by myocardial tissue during systole. Pressure and flow waveform in coronary arteries are not synchronized and this is caused by the intramyocardial pressure. During diastole as the ventricles relaxes, the coronary vessels are no longer compressed and this allows to restore a normal blood flow [54].

### 1.2.2. Pathologies of the Coronary Arteries

Despite the advances in medical therapy and the development of invasive and non-invasive cardiovascular diagnostic testing, cardiovascular diseases (**CVDs**) are still the main cause of death globally. CVDs take approximately 17.9 million lives each year, an estimated 32% of deaths worldwide. About 8% of deaths are due to heart attack and stroke. Almost one third of deaths occur prematurely in people under 70 years of age. The main of these disorders include coronary arteries disease (**CAD**), cerebrovascular disease and rheumatic heart disease [72].

CAD represents the most common heart disease with high morbidity and mortality. It is the leading cause of death globally [40]. In one study, it was estimated that CAD represented 2.2% of the overall global burden of disease and 32.7% of cardiovascular diseases [70]. In the United States (**US**) alone, by year 2035 the number of people with CAD is expected to increase to 24 million [16]. CAD is a condition in which there is an inadequate supply of blood and oxygen to the myocardium. The reason for such disease is typically related to the build-up of atherosclerotic plaques inside the arterial lumen leading to coronary stenosis. The impairment in blood flow and thus to oxygen delivery to the myocardium is manifested by stable angina, unstable angina, myocardial

infarction (**MI**) or sudden cardiac death [40]. Myocardial ischemia caused by coronary artery stenosis is the main reason of CAD. The high incidence of this pathology is mainly related to the silent atherosclerotic plaque progression toward erosion and rupture, known as acute coronary syndrome (**ACS**). The risk factors of CAD include diabetes mellitus, hypertension, smoking, family history, hyperlipidaemia, obesity, lifestyle, age, gender and psychosocial stress [3, 40].

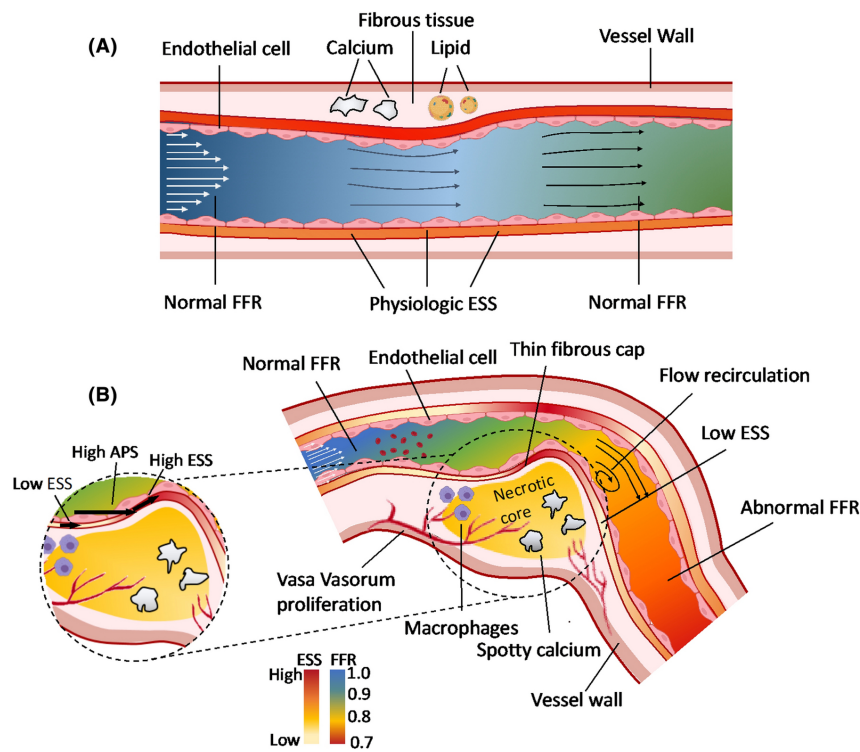
### 1.2.3. Atherosclerosis

CAD is mostly caused by the accumulation of lipoproteins in the intimal layer of coronary arteries, resulting in atherosclerosis. Atherosclerosis may be seen as an ongoing inflammation in response to local endothelial dysfunction, a process that continuously weakens the vessel wall. The disease process involves the build-up of a plaque made up of fatty materials, fibrous elements, smooth muscle cells, inflammatory cells and calcium in the vessel lumen (**Figure 1.3**). It can progress from early, benign lesions to more severe, rupture prone ones, over time. There are two forms of CAD: stable ischemic heart disease, which presents as stable angina, and acute coronary syndrome, which occurs when a vulnerable plaque suddenly ruptures and leads to a heart attack. When blood supply to the cardiac tissue is cut off for more than a few minutes, the heart cells start to die, and normal heart tissue is replaced with scar tissue. Plaque rupture, usually of a precursor lesion known as “*vulnerable plaque*”, is the main cause of thrombosis [3, 4, 53].

Coronary stenosis can be stratified based on its severity. If the level of obstruction is less than 50%, the stenosis is mild, between 50% and 70%, it is moderate, greater than 70% it is classified as severe [34]. The level of obstruction typically refers to the extent to which the coronary arteries are narrowed or obstructed by atherosclerotic plaques. It is often measured as the relationship between the open and narrowed vessel.

## 1.3. Overview of Current Techniques to Diagnose and Treat CAD

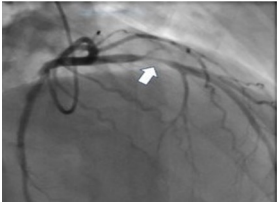
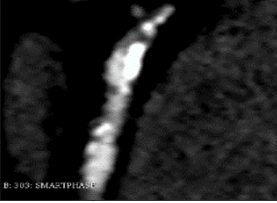
Identifying those patients at highest risk of CAD with an early diagnosis, and ensuring they receive appropriate and individualized treatments, can prevent premature deaths. Coronary disease can be quantified by means of anatomical parameters (e.g.. diameter and area of the stenosis) and hemodynamic indices (e.g. coronary flow reserve and fractional flow reserve). Different invasive and non-invasive imaging technologies have been used to evaluate and quantify the severity and physiological significance of CAD. These



**Figure 1.3:** Illustration of the interaction of physiological conditions and biomechanical stresses in the regulation of atherosclerosis. **(A)** Characteristics of a stable plaque with stable calcification and small lipid pools. Mild narrowing of the lumen without disturbing the physiological blood flow. **(B)** Rupture-prone vulnerable plaque with a large lipid-rich necrotic core, neovascularization, spotty calcium, thin fibrous cap and presence of inflammatory cells. Severe narrowing that can lead to ischemia. The lesion also causes endothelial shear stress variations proximally and distally to the plaque [16].

include invasive coronary angiography (**ICA**), intravascular ultrasound (**IVUS**), computed tomography (**CT**), magnetic resonance imaging (**MRI**), optical coherence tomography (**OCT**), positron emission tomography (**PET**) and transthoracic echocardiography (**TTE**) [78].

At present the two main imaging techniques that are used in clinical practice are ICA and CT. ICA with its high spatial and temporal resolution has been for years the gold standard for the evaluation of coronary artery lumen and anatomic diagnosis of CAD. The invasive procedure, however, presents different risks of potential complications, considerable costs and high radiation exposure [30]. In the last decades computed tomography coronary angiography (**CCTA**) appeared as a robust, reliable and non-invasive modality for assessment of CAD. Compared to IVUS and MRI, CT is less expensive, non-invasive, and accessible for patients with implants [35]. Correct extraction and reconstruction of coronary plaques from CT images plays an important role in improving the quality of diagnosis of CAD. A comparison between the two diagnostic modalities is presented in **Table 1.1**.

IMAGING MODALITY	Advantages	Disadvantages
 ICA	Gold standard to obtain FFR guided PCI, high spatial and temporal resolution	Invasive, high medical costs, not feasible to determine histology of the plaque, X-ray and contrast use
 CCTA	Non-invasive, low-cost identification of plaque morphology	Radiation exposure and contrast allergy, presence of artifacts

**Table 1.1:** Comparison between ICA and CCTA imaging modalities. Main advantages and disadvantages. ICA image from [15] and CCTA image from the dataset used in this study.

In the clinic, X-ray ICA is the most used imaging modality. Projection images of the arteries are taken and assessed visually by an expert to determine the percentage of the artery cross-section that is obstructed. The anatomically significant threshold to determine whether revascularization procedure or medical therapy is more appropriate, is a

50% diameter stenosis [19]. When multivessel CAD is present, coronary angiography however, may result in overestimation or underestimation of a lesion’s severity and often it is also inaccurate in determining which is the lesion causing ischemia. The limitations and the poor correlation with functional stenosis severity in terms of blood flow obstruction of this method led to the development of alternative approaches. The continuous technological advancements of the last years have brought to faster CT scanners with lower radiation and contrast dose and CCTA has become an attractive non-invasive first-line imaging modality for CAD. It is able to accurately assess coronary artery stenosis severity and atherosclerotic plaque composition (**Figure 1.4**). Nowadays it can be used as an alternative to ICA in patients with suspected ACS who have low or intermediate probability of CAD. In patients with high probability of CAD, ICA should be considered as the gold standard imaging modality due to the lower negative predictive value of CCTA in this group [47].



**Figure 1.4:** Atherosclerotic plaques seen from CCTA images. Extraction of coronary arteries plaque from CT images is usually based on difference in attenuation value. **(A) Calcified plaque.** It is easy to extract due to high attenuation value. The brightness of the plaque could affect the neighbouring pixels creating a blooming effect and thus overestimating the calcification size. **(B) Non-calcified plaque.** The contrast in grayscale values between plaques, arterial walls and surrounding tissue is very low. To accurately separate the plaque from the surrounding tissue the morphological properties of the non-calcified plaques need to be considered [35]. It is still a challenge to differentiate between fibrotic and lipidic plaques. The two images are taken from the dataset used in this study.

### 1.3.1. Fractional Flow Reserve

Fractional Flow Reserve (**FFR**) is a “*lesion-specific index reflecting the effect of the epicardial coronary stenosis on myocardial perfusion*” [51]. It is a clinically used, accurate and selective index of physiological importance of a coronary stenosis. By definition, FFR is the ratio between the maximum achievable blood flow in the presence of a stenosis and normal maximum blood flow of an artery:



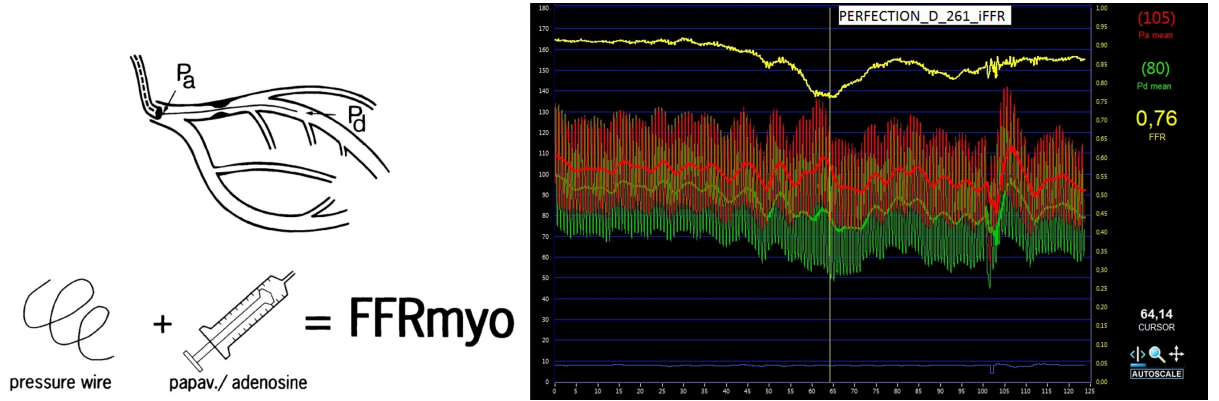


Figure 1.5: (A) Schematic representation of the pressure wire used in the ICA during the pull-back procedure. Pa and Pd are respectively the aortic (i.e. proximal) and distal pressure.[50]. (B) Pressure recordings during the invasive FFR measurement. Data from a patient present in the dataset of this study.

$$FFR = \frac{Q_{max,stenosis}}{Q_{max,normal}} \quad (1.1)$$

Therefore the index represents the fraction of maximum flow which can still be maintain in spite of the presence of the stenosis. It exactly tells to what extent a patient is limited by his coronary artery disease. It is currently the gold standard diagnostic hemodynamic factor for ischemia detection and it's measured during ICA under adenosine-induced hyperaemia. Maximum hyperaemia is usually reached with an intravenous adenosine dose of  $140 \mu g \cdot kg^{-1} \cdot min^{-1}$  [37, 73]. Adenosine administration activates a A2A receptor causing coronary artery vasodilation, leading to 3.5 to 4-folds increase in myocardial flow in healthy humans [39]. During maximum hyperaemia, coronary flow and pressure achieve a linear correlation, as coronary resistance is kept stable and minimal. By translating coronary flow into a pressure ratio, FFR becomes independent of haemodynamic conditions. FFR can be thus approximated as the ratio between distal and proximal pressure [19, 52]:

$$FFR = \frac{P_{distal}}{P_{proximal}} \quad (1.2)$$

FFR is clinically estimated by invasively inserting a pressure wire and measuring the distal (i.e. the downstream) and proximal (i.e., the upstream) pressure to a stenosis during maximum vasodilation. (Figure 1.5) The pressure sensor is inserted into the femoral or radial artery and guided by angiography toward the site of interest. The pressures are recorded and mediated during several cardiac cycles by a pullback procedure. The guidelines suggests to take the value 20-30 mm after the stenosis. [51, 77]

FFR value ranges from 0 (complete occlusion) to 1 (no occlusion). An FFR of 0.80 is commonly accepted, with an accuracy of 90%, as the threshold below which a stenosis is considered ischemia causing and thus used as clinical indicator for coronary revascularization (i.e., stenting). An FFR of 0.80 means that a given stenosis causes a 20% drop in blood pressure. Blood flow to the myocardium diminishes as the luminal diameter progressively narrows. During hyperaemia, flow progressively decreases when the degree of stenosis is about 40% or more and does not differ significantly from basal flow when stenosis is 80% or greater [68] (**Figure 1.6**).

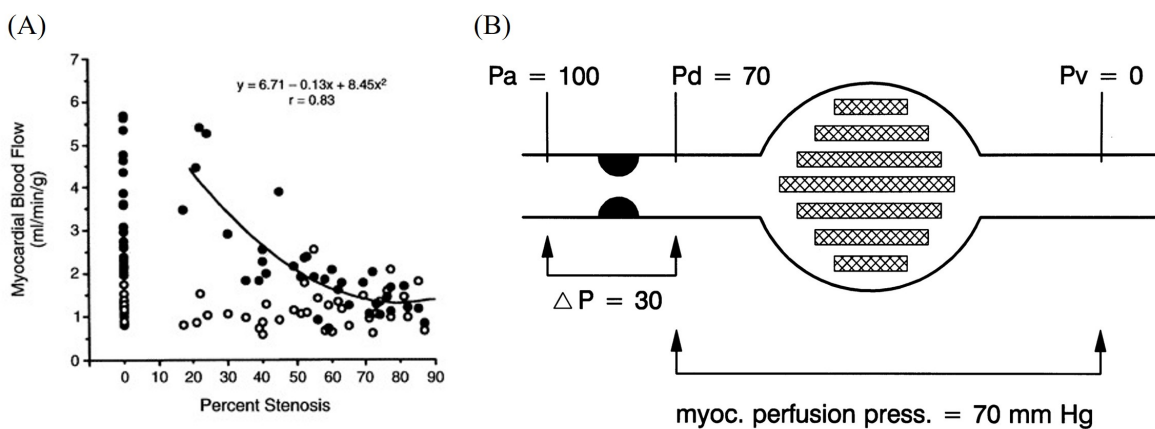


**Figure 1.6:** (A) Relationship between myocardial blood flow and degree of stenosis [68]. (B) Simplified representation of a coronary artery stenosis and the supplied myocardium. In this example myocardial perfusion pressure would be 100mmHg if no stenosis were present. Due to the stenosis, pressure has decrease to 70mmHg. Hence, the FFR that represents the fraction of normal maximum flow that is preserved despite the presence of the stenosis is represented by  $(70-0)/(100-0)$ . This means that in this case  $\text{FFR} = 0.70$  [51].

The use of FFR to guide revascularization in patients with angina and angiographically intermediate stenosis is a Class I recommendation according to the 2021 Guidelines approved by the major cardiovascular societies worldwide [34]. However, despite this recommendation, its application in cardiac catheterization laboratories has been low due to excessive costs, extra time involved, procedural complications, contrast use and adenosine-related contraindications. It is currently utilized in fewer than 10% of CAD assessments [19, 38].

## 1.4. Available Treatments

Treatment of CAD varies based on the severity and location of the occluded vessel. After diagnosis, effective interventions can be performed either non-invasively, controlling risk factors and symptoms through a pharmacological approach, or invasively through revascularization, when dealing with more severe stenosis. Revascularization can reduce the

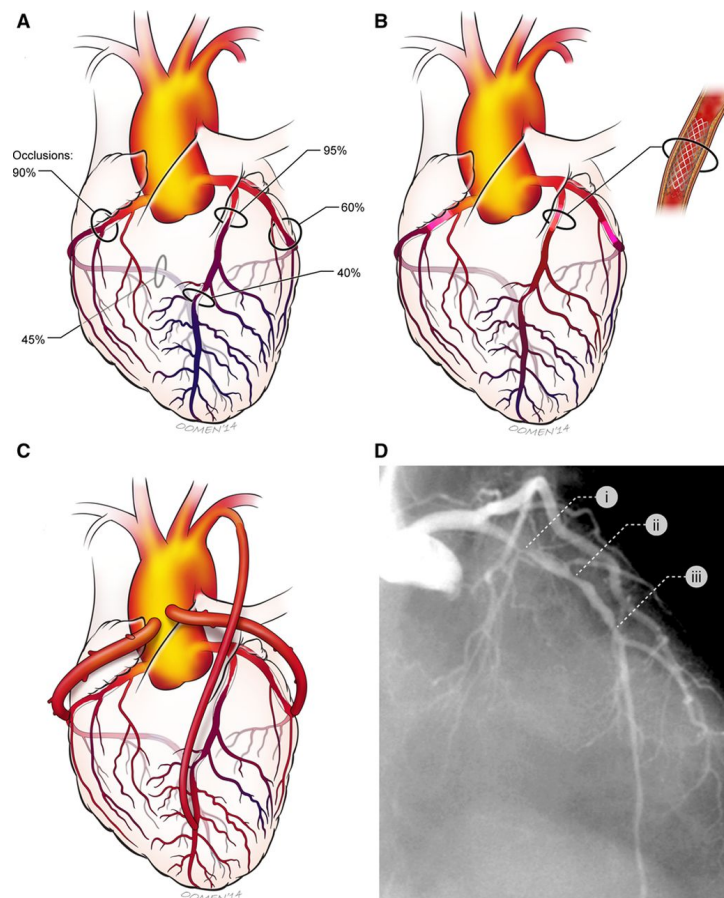


**Figure 1.7:** Revascularization treatments [20]. **(A)** Coronary artery stenosis. **(B)** Revascularization through angioplasty with stent. **(C)** Coronary artery bypass graft surgery. **(D)** Invasive coronary angiography or ICA.

risk of MI and improve patient outcomes when applied to ischemic lesions, whereas if it is applied to non-ischemic lesions it is controversial [19]. Revascularization requires a procedure or a surgery to reestablish a physiological blood flow to the heart. It is possible to implant a stent in the area where the vessel is occluded (angioplasty) or to entirely bypass the blocked segment of the artery surgically (bypass surgery) (**Figure 1.7**).

#### 1.4.1. Percutaneous Coronary Intervention or Angioplasty

Percutaneous coronary intervention (**PCI**) is a non-surgical, invasive procedure used to reduce the narrowing or occlusion of the coronary artery and improve the blood supply to the heart. The procedure is realized by introducing a catheter via a peripheral artery and inflating a balloon in the region of interest where the artery is blocked. In most patients a coronary stent is then placed to keep the artery open and reduce the possibility of recurrent narrowing. The evolution of stents plays a significant role in the result of the procedure. Stents are frequently coated with medications to prevent clot development

and the risk of narrowing [20, 22].

### 1.4.2. Coronary Artery Bypass Graft Surgery

Coronary artery bypass graft (**CABG**) surgery is instead an open-heart surgery procedure that requires anaesthesia. The heart is stopped and a heart-lung bypass machine is used to pump the blood throughout the body. The aim is to create a new route for blood to flow that bypasses the narrowed or blocked coronary artery. Veins taken from the leg and an artery taken from within the chest are used to bypass the coronary artery blockages. The bypass grafts have a high chance of remaining open in the first 5 to 8 years after the operation [20].

### 1.4.3. Treatment Choice Criteria

Patients who have experienced a recent heart attack have a better chance of survival if the blocked artery is unblocked quickly. In cases where the heart muscle is damaged and there are multiple blockages, bypass surgery can extend life, even if there are no symptoms present. When only one artery is blocked, angioplasty is the preferred method as it is less invasive and allows for faster recovery. When multiple obstructions are present, both options are viable, and the decision is based on the location of the lesions and the patient's condition. Studies comparing the two methods have shown that angioplasty and surgery result in similar control of chest pain and similar survival rates over a five-year period [13]. However, patients who undergo angioplasty may need more repeated procedures. Neither CABG or PCI can entirely prevent heart attacks in patients with stable CAD, but CABG provides better blood flow to a larger portion of the heart muscle since not all blockages can be treated with PCI. Revascularization does not stop the development of atherosclerosis, so it is important to adopt a healthy lifestyle, control cholesterol and blood pressure, take part in physical activity, and quit smoking to reduce the risk [22].

## 1.5. Future Diagnostic Strategy

FFR has been widely accepted as the gold standard for assessing the functional significance of coronary stenosis. Its use has been shown to improve clinical outcomes in patients undergoing PCI. The FAME and FAME II [11, 17, 23, 66] trials demonstrated the benefits of using FFR-guided revascularization in comparison to angiographically-guided strategies alone. The results showed a significant reduction in the rate of major adverse cardiac events, which highlights the importance of using functional assessments in the

management of patients with stable CAD. Additionally, FFR-guided therapy has shown to help identifying patients who may not benefit from revascularization, thus avoiding the risks and costs associated to the procedure and improving patients outcomes. The use of FFR in the management of patients with stable CAD has become an essential part of the diagnostic and therapeutic methods for interventional cardiologists. Considering the threshold value of 0.80 the cardiologists can identify the best treatment.

In the last years continuous advancements and improvements in clinical images, mathematical models and computational power has led to a new way to assess functional severity of CAD. Fractional Flow Reserve Computed Tomography (**FFR<sub>CT</sub>**) has emerged as a new diagnostic tool for non-invasively predicting FFR from CCTA. The index combines image information with computational models to estimate the hemodynamic assessment of coronary lesions. It provides an alternative to the gold standard invasive FFR (**iFFR**) measurements. CCTA may play an important role as a first step in the screening, diagnosis, decision making and treatment planning of CAD. It would be beneficial for the patient and cost effective for the health economies. In the US CCTA (\$301) with  $FFR_{CT}$  (~\$930) is \$1138 cheaper than ICA (\$2838) with FFR [2, 58]. NICE (The National Institute for Health and Care Excellence, United Kingdom) have suggested that the selective use of  $FFR_{CT}$  may lead to cost savings of £391/patient/year and a reduction in ICA by 60%.

$FFR_{CT}$  has demonstrated high diagnostic accuracy as compared to FFR and has been shown to significantly decrease unnecessary diagnostic cardiac catheterizations without adverse clinical events [43, 48]. Several clinical trials such as DISCOVER-FLOW [31], DE-FACTO [42] and NXT [48] (**Figure 1.8**) trials, have compared  $FFR_{CT}$  and standard FFR and demonstrated the superiority of  $FFR_{CT}$  in the diagnosis of ischemic lesions. NXT trial also demonstrated that the diagnostic accuracy of  $FFR_{CT}$  was significantly greater than CCTA alone. Another study is the PACIFIC study [10] that, comparing diagnostic accuracy of various imaging modalities using FFR as reference standard, found significantly better results for  $FFR_{CT}$  with respect to CCTA, SPECT and PET. FORECAST trial [9] results instead, showed that in patients with stable angina, CCTA with selective  $FFR_{CT}$  strategy did not differ significantly from standard care in terms of costs or clinical outcomes. However, it did lead to a significant reduction in the use of ICA. Different follow-up studies have proved the prognostic accuracy of  $FFR_{CT}$  in predicting outcomes from 1 to 5 years. The ADVANCE registry [49], a large multi-centre study, provided evidence of the practical applications of  $FFR_{CT}$  in clinical practice. It revealed that introduction of  $FFR_{CT}$  into the decision-making process alongside CCTA, results in reduced unnecessary invasive angiographies and a better prediction of individuals at low

risk of adverse cardiac events.

Overall, these results provide strong evidence for the potential of  $FFR_{CT}$  as a diagnostic tool in the management of CAD. An integration of CCTA before selective invasive testing in the evaluation of suspected CAD could significantly lower diagnostic expenses and decrease the requirement for angiography. Using CCTA, a patient's non-invasive assessment will guide the patient's therapy decision. If the patient needs an invasive treatment, either PCI or CABG will be performed. The FASTTRACK CABG study [27] was the first study to assess safety and feasibility of planning and execution of surgical revascularization in patients with complex CAD, solely based on coronary CCTA combined with  $FFR_{CT}$ .

For patients with non-obstructed CAD, sophisticated assessments such as plaque characterization, can be performed to identify high-risks plaques and target primary prevention strategies. This can help reduce the risk of future cardiovascular events. Revascularization guidelines recommend physiological assessment of stenotic lesions with treatment targeted at only functionality significant lesions. Due to the cost of  $FFR_{CT}$ , one alternative would be to analyse only patients who continue to suffer from symptoms despite medical treatment. The assessment procedure of borderline obstructive lesions in these patients still needs to be improved [58]. Despite the potential of this new diagnostic tool, there are also some limitations. It requires high quality CCTA, difficult in patients with morbid obesity and suboptimal heart rate. Imaging artifacts and low resolution images may affect CCTA interpretability, including calcification, motion, misregistration and beam hardening effect cause by a potential stent in the arteries [16, 21]. Present CCTA have typically an in-plane spatial resolution of  $0.3 \times 0.3 \text{ mm}^2$  and a through plane resolution of  $0.7 \text{ mm}$ , which limits its use to coronary arteries of  $1 \text{ mm}$ . However, CAD is not generally characterized nor FFR calculated in such small vessels. Usually clinician analyse a coronary stenosis in diameters of  $2 \text{ mm}$  or greater [32, 37, 79].

At present  $FFR_{CT}$  analysis is solely available via a centralized commercial web-based service by HeartFlow <sup>®</sup> company. HeartFlow (Mountain View, CA, United States) is a medical technological company focusing on the diagnosis of CAD. Their main product is a non-invasive personalized cardiac test that provides visualization of the patient's coronary arteries and enables clinicians to create more effective treatment plans. HeartFlow  $FFR_{CT}$  is actually the only U.S Food and Drug Administration-approved computational fluid dynamics (CFD) technique for measuring coronary blockages non-invasively. Nowadays it can be used in clinical practice and an HeartFlow  $FFR_{CT}$  analysis costs \$930.34 [2]. It is the first company producing a software based on mathematical models and CFD analysis that, given a cardiac CT, reconstructs 3D patient-specific model of coronary arteries, calculates the FFR using a finite element mesh model and uses CFD methods to

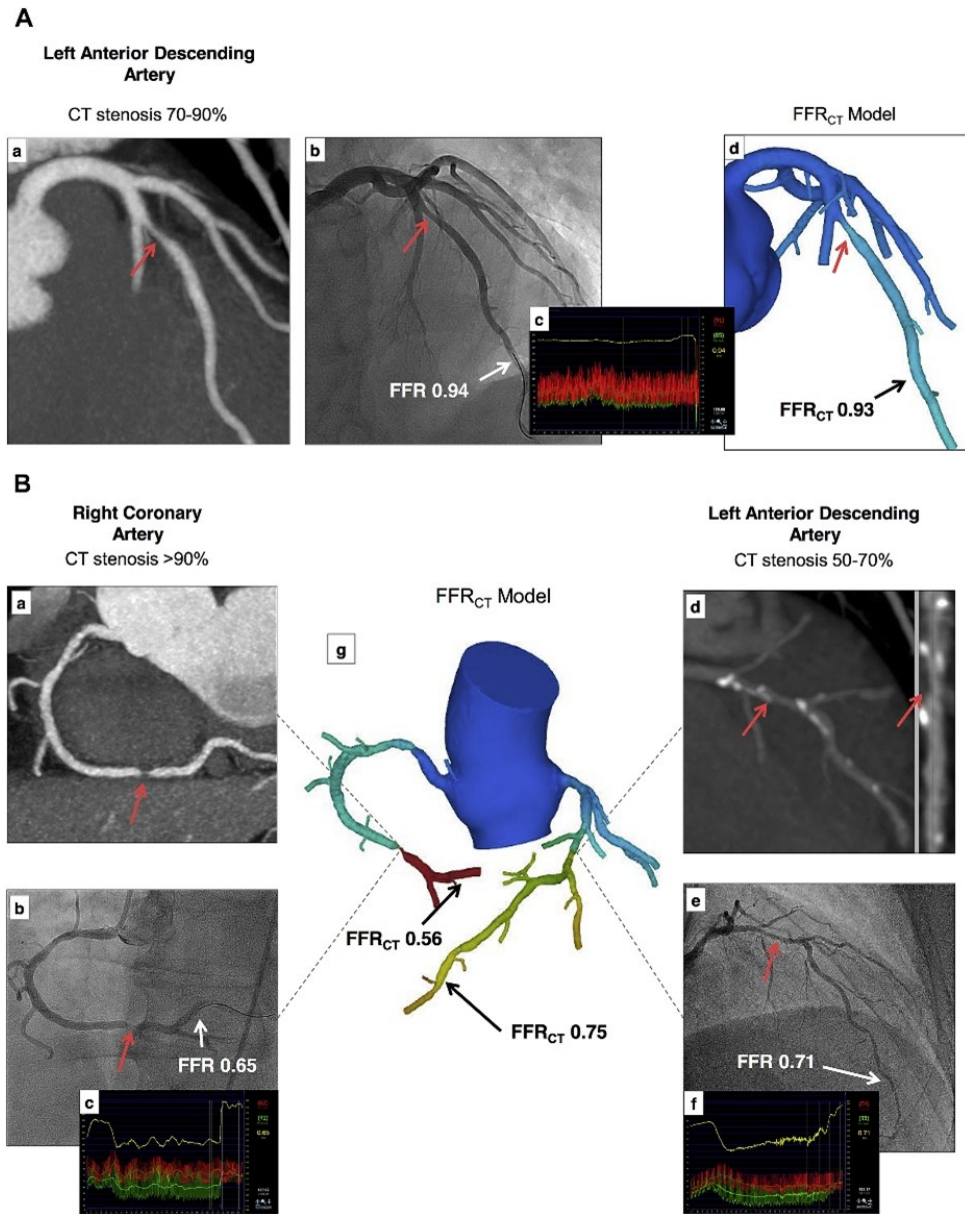


Figure 1.8: Results of iFFR and non-invasive  $FFR_{CT}$  in patients with mild, intermediate and severe stenosis. Agreement between the two methods in detecting which stenosis are ischemia causing ( $FFR \leq 0.80$ ). [48]

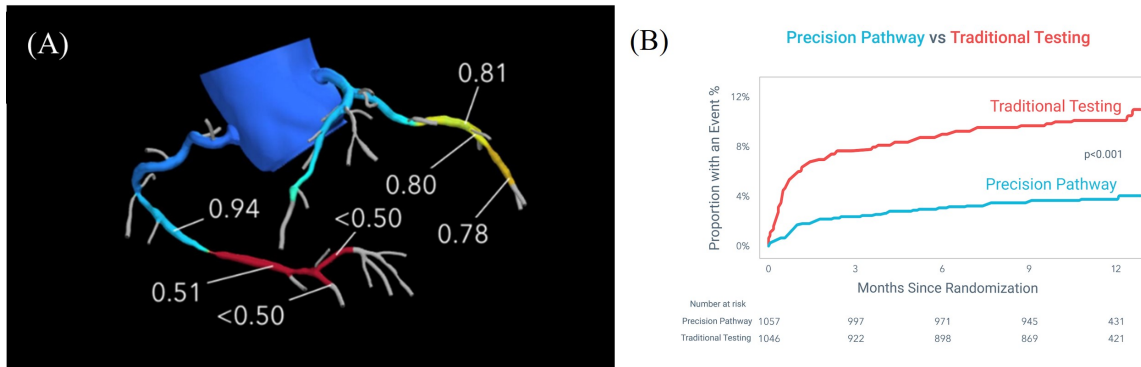


Figure 1.9: (A) Example of an HeartFlow  $FFR_{CT}$  analysis. (B) In the graph in shown the superiority of Precision Pathway ( $FFR_{CT}$  analysis) with respect to the Traditional Testing consisting in the functional stress testing and Invasive Coronary Angiography. HeartFlow  $FFR_{CT}$  demonstrated to significantly reduce all-cause of death, nonfatal MI or catheterization without obstructive disease at 1 year.

solve fluid dynamics governing equations. The result is a 3D solution of  $FFR_{CT}$  throughout the coronary tree. In **Figure 1.9** is shown the potential of this new diagnostic tool with respect to traditional testing analysis nowadays used in clinical practice.



## 2 | State of the Art

CFD has made significant advancements in recent years. Its application to the calculation of coronary flow and pressure field has led to the development of various mathematical models for the assessment of  $FFR_{CT}$  (i.e., FFR evaluated non-invasively from CT, by means of CFD models). CFD-based models can provide valuable information about the hemodynamic of coronary circulation. Although CFD analysis applied in the study of coronary arteries' flow is challenging, especially due to their complex and tortuous shape, the development of different computational techniques has received great attention. These models require large computational resources, but at the same time have the potential to transform the way FFR is measured. The study of coronary artery stenosis based on CFD simulations can be retrospectively traced to the 2000s with Banarjee and colleagues [5]. The main objective of their study was to examine the local hemodynamic implications of coronary artery stenosis post-angioplasty. Up to date different models, from ideal geometries to more complex patient-specific coronary trees, have been proposed. The main steps required to perform an  $FFR_{CT}$  analysis are the ones reported in **Figure 2.1**.

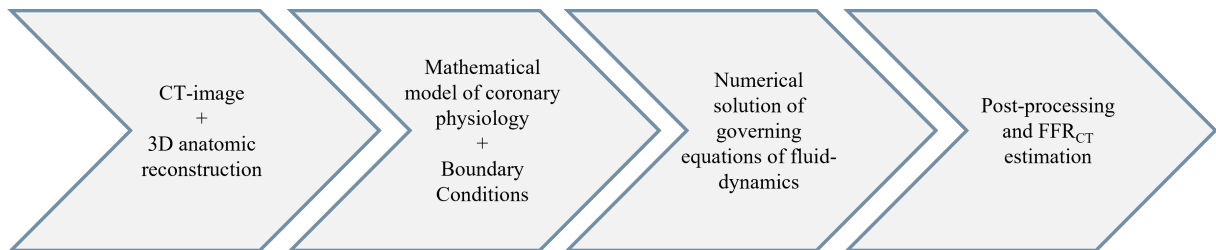


**Figure 2.1:** Main steps required to perform an  $FFR_{CT}$  analysis. CT images acquisition followed by image segmentation and reconstruction of the 3D anatomical model. Later a mathematical model of the coronary physiology is created and appropriate boundary conditions must be imposed at the outlet surfaces of the domain. Finally the governing equations of fluid-dynamics are solved and  $FFR_{CT}$  value is estimated during the post-processing.

Accurate coronary segmentation and realistic physiological modelling of BCs are crucial steps to ensure a high diagnostic performance of the model. Accurate segmentation is essential to ensure that the model can accurately detect and diagnose the presence of any CAD. Proper choice of BCs is also critical. This involves modelling the behaviour of

blood flow and pressure within the coronary arteries, as well as the interaction between the arteries and the surrounding tissue. Each of the steps outlined above requires a thorough understanding of medical image analysis and cardiovascular physiology, as well as meticulous attention to detail.

**NAVIER-STOKES EQUATIONS.** Flow and pressure in the coronary arteries can be computed by numerically solving the governing equations of fluid-dynamics known as Navier-Stokes Equations (**NSEs**). These equations are based on conservation of mass principle and generalization of Newton's second law to a fluid. The mass conservation and momentum formulas are reported below:

$$\nabla \cdot u = 0 \quad (2.1)$$

$$\rho \frac{\partial u}{\partial t} + \rho u \cdot (\nabla u) = -\nabla p + \mu \nabla^2 u \quad (2.2)$$

where  $u$  is the velocity vector,  $p$  is the pressure and  $\mu$  and  $\rho$  are respectively the viscosity and density of the blood. Blood density and viscosity are known when solving the equations and, despite the complex rheological properties of blood, it can be approximated as an incompressible Newtonian fluid with constant density and viscosity [67]. NSEs can only be solved analytically under certain circumstances (steady or pulsatile flow in an idealized cylindrical geometry). Despite they are conceptually simple, they are really complex to solve and this preclude their direct solution. Numerical methods are thus needed in order to discretize each term of the equation. In this work finite volumes method was used to solve numerically NSEs. Finite volume methods is one of the possible approaches used to solve numerically partial differential equations (**PDEs**). Briefly, it consist in discretizing the computational domain into a set of control volumes, which are small regions of space over which the conservation equations are applied. The method involves the discretization of the equations, both in terms of space and time, leading to a system of algebraic equations that can be solved numerically. Finite volume methods are widely used in CFD and have proven to be very effective for solving a wide range of problems in fluid-dynamics. The accuracy of the method can depend on the specific details, the problem being solved and the numerical implementation of the method.

NSEs on their own are insufficient to solve blood flow problems: a domain of interest and appropriate boundary conditions need to be specified.

## 2.1. Related Works

Several different models have been implemented in the literature to study the coronary lesions from medical images, in a non-invasive way. In the last years the focus has been mainly on CFD models developed from CCTA images. Some groups also explored innovative machine learning (ML) approaches.

Each of the developed models has its own strengths and limitations, and the choice of the model depend on the specific research question and available resources.

### 2.1.1. Segmentation and Meshing

Segmentation of coronary arteries and 3D model reconstruction is the first step to be performed to achieve a computational model of coronary flow. Manual [44], semi-automatic [37], automatic or deep-learning algorithms have been used [60, 64]. Manual editing and refinement of the segmentation results is finally performed and lastly the accuracy of the 3D geometry is checked by experts(i.e. radiologists) [64]. As second step, geometries are meshed. Almost all the authors used tetrahedral elements to discretize the coronary volume and obtained a number of mesh elements in the order of  $10^6$ .

The reconstructed model could include the aorta with LCA and RCA or LCA or RCA alone in order to reduce time and computational costs (see **Table A.1 and A.2 in Appendix A**). Few authors performed the simulation just on the coronary branch of interest [44, 75].

Different truncation strategies have been implemented and studied. Most of the works decided to keep the coronary branches up to a diameter of 2 mm, due to the resolution of the CCTA images. Shi et al. [60], studied the influence of subbranch removal, Liu et al.[37], tested an in-house standardized truncation strategy on the straight vascular segment of the first-generation branch of the main coronary and Wu and colleagues [74] investigated instead the influence of coronary tree expansion to smaller arteries in the calculation of the  $FFR_{CT}$ .

### 2.1.2. Assumptions on Coronary Flow

In order to have an accurate model, realistic pressure and flow-rates need to be considered. Resting coronary flow is usually supposed to be 4-5% [50] of the cardiac output (CO). The total coronary flow is then subdivided in LCA flow and RCA flow with a 6:4 [6, 77] or 7:3 [24, 56] proportion or based on coronary artery dominance [55]. Different methods

have been adopted to simulate inlet flow and distribution: total inlet flow was either assumed to be proportional to some power of Left Ventricular Mass (**LVM**) (i.e. [65]), constant and equal to the average flow among the patients or based on patient-specific data as Systolic Blood Pressure (**SBP**), Heart-Rate (**HR**), gender and age (i.e. [37]).

With the aim of assigning proper outlet BCs, flow-rate must be correctly subdivided in the coronary branches. The most adopted method is based on flow proportion to vessel diameter (**Equation 2.3**). The relationship used is Murray's law [46]. It describes the physical principles for fluid flow through branched networks and it is based on minimum work hypothesis.

$$Q \propto d^k \quad (2.3)$$

in which  $Q$  is the flow-rate through a blood vessel and  $d$  is its diameter.  $k$  is a constant derived empirically that Murray set to 3. Coronary blood flow in the  $i_{th}$  outlet branch can be calculated according to the following equation:

$$Q_{out_i}^{rest} = Q_0 \frac{d_i^\beta}{\sum_{i=1}^N d_i^\beta} \quad (2.4)$$

where  $Q_0$  is the blood flow of the parent vessel,  $d_i$  is the diameter of the  $i_{th}$  outlet branch and  $N$  the number of outlets after each bifurcation. In human coronary arteries the real value of the beta exponent remains unknown but some studies have used 2.6 (i.e. [60]).

Some authors have compared this method with the partition of inlet flow-rate based on Transluminal Attenuation Gradient (**TAG**) [64], PET-perfusion [39] or stress-computed tomography perfusion (**CTP**) [76]. The obtained results and their comparison will be later discussed in Section 2.3.2.

### 2.1.3. Boundary Conditions

At the inlet, most authors prescribed flow or pressure waveforms. To mimic the conditions at the outlet boundaries of the domain of interest, reduced-order model are generally used. Since it is impossible to know a priori flow and pressure waveforms, coupling 3D-0D or 1D-0D models is a commonly used solution. Thus, the 3D pressure and flow fields of the coronary arteries are coupled to a Lumped Parameter Model (**LPM**) at the boundaries, representing the downstream circulation.

#### 2.1.4. Post-processing

Once the simulation results were obtained, post-processing was performed to calculate the indexes of interest.  $FFR_{CT}$  have been compared between transient and steady simulations and, most-importantly, the validation with the invasively measured FFR have been analysed. FFR standards in invasive measurements specify to place the distal monitor point at least 2-3 cm distally to the stenosis [61]. If available the same invasive location is used to assess the validity of  $FFR_{CT}$ , otherwise a value 2-4 cm distally to the coronary lesion is analysed.

Other indexes as Instantaneous Wave-free Ratio (**iFR**), Wall Shear Stress (**WSS**), Coronary Flow Reserve (**CFR**) or Quantitative Flow Ratio (**QFR**) have also been investigated.

A schematic synthesis of the systematic literature review is reported below in **Table 2.1**.

Authors	Imaging	Geometry	Steady/ Transient	Inlet BC	Outlet BC	Indexes
<i>Kim et al., 2010 [29]</i> <sup>(1)</sup>	CCTA	Model of the heart and arterial system	Transient	Inflow BC coupling the heart and a closed loop model	Upper branch vessels and thoracic aorta: 3WK Coronary outlets: RCRCR+Pmyo	WSS
<i>Sharma et al., 2012[59]</i> <sup>(2)</sup>	CCTA	LAD	Steady	$MAP = DBP + [1/3 + (HR \cdot 0.0012)] \cdot (SBP - DBP)$	R	$FFR_{CT}$
<i>Taylor et al., 2012 [65]</i> <sup>(1)</sup>	CCTA	Aorta+LCA+RCA Idealized	Idealized: steady Patient-specific: transient	LPM of the heart	Aorta outlet: 3WK Coronary outlet: RCRCR+Pmyo Pv: 0mmHg	$FFR$ , $FFR_{CT}$
<i>Kwon et al., 2014[33]</i> <sup>(3)</sup>	CCTA	Aorta+LCA+RCA RCA/LCA alone Idealized	Transient	LCA/RCA simulation: Pao waveform based on patient's HR, SBP, DBF Model with the aorta: inlet flow-rate	Aorta outlet: Pao Coronary outlets: RCRCR+Pmyo Pv: 0mmHg	$FFR$ , $FFR_{CT}$ WSS
<i>Sankaran et al., 2016[57]</i> <sup>(1)</sup>	CCTA	Aorta+LCA+RCA Idealized	Idealized: steady Patient-specific: transient	Idealized: Pao Patient-specific:parabolic velocity profile	Resistance model	$FFR_{CT}$ + impact of MLD, LL, R, viscosity
<i>Boileau et al., 2017[6]</i> <sup>(4)</sup>	CCTA	LAD with artificial stenosis	Transient	Flow waveform	RCRCR+Pmyo Pv: 5mmHg	$FFR_{CT}$
<i>Morris et al., 2017[44]</i> <sup>(5)</sup>	Angiography	Vessel of interest	Pseudo-transient	Patient-specific pressure invasively measured	R	$FFR$ , $vFFR$

<i>Tang et al., 2018[63]</i> (6)	CCTA	3D-0D	LCA/RCA	Steady	$MAP = \frac{SBP}{3} + 2 \cdot \frac{DBP}{3}$	R	FFR, $FFR_{CT}$ ESS
<i>Lo et al., 2019[38]</i> (7)	CCTA	3D-0D	Aorta+LCA+RCA	Quasi-steady + transient	4 different flow-rates: steady, pulsatile patient-specific, population average	2WK (transient) R (quasi-steady) Pmyo in LAD Pv: 0mmHg	FFR, iFR baseline Pd/Pa
<i>Yin et al., 2019[77]</i> (8)	3D model from an open source imaging repository	3D-0D 1D-0D	Aorta+LCA+RCA	Transient	Patient-specific flow waveform	RCRCR+Pmyo Pv: 0mmHg	$FFR_{CT}$
<i>Muller et al., 2019[45]</i> (9)	CCTA	3D-0D 1D-0D	LCA/RCA	Steady	Pressure	Prescribed flow-rate or resistive elements	FFR, $FFR_{CT}$
<i>Tang et al., 2020[64]</i> (10)	CCTA	3D-0D 1D-0D	Aorta+LCA+RCA	Steady	MAP Hyperemia: $P_{hyp} = 0.8 \cdot P_{rest}$	R	FFR, $FFR_{CT}$
<i>Tajeddini et al., 2020[62]</i> (11)	CCTA	3D-0D 1D-0D	LAD/LCX	Transient	Pao waveform	RCRCR+Pmyo	$FFR_{CT}$ , iFR CFR+influence LL, MLD, D% +WSS, OSI, TAWSS, RRT
<i>Lo et al., 2020[39]</i> (7)	CCTA	3D-0D	Aorta+LCA+RCA	Steady	Patient-specific steady inflow	2WK	FFR
<i>Liu et al., 2021[37]</i> (12)	CCTA	3D-0D	LCA/RCA	Steady	$MAP = 0.4 \cdot (SBP - DBP) + DBP$	R	FFR, $FFR_{CT}$

<i>Wu et al.</i> , 2021[74] <sup>(13)</sup>	CCTA	3D-0D	Aorta+LCA+RCA	Transient	Patient-specific inflow $MAP = DBP + [1/3 + (HR \cdot 0.0012)] \cdot (SBP - DBP)$	Resistive model [69]	FFR, FFR <sub>CT</sub>
<i>Liu et al.</i> , 2022[36] <sup>(14)</sup>	CCTA	3D-0D	Aorta+LCA+RCA	Steady		RL	FFR, FFR <sub>CT</sub>
<i>Xi et al.</i> , 2022[39] <sup>(14)</sup>	CCTA	FSI-0D	Vessel of interest	Transient	Pao waveform	RLC	FFR, FFR <sub>CT</sub>
<i>Shi et al.</i> , 2022[60] <sup>(15)</sup>	CCTA	3D-0D	LCA	Transient	Pressure waveform	Time dependent blood flow	TAP, TAWSS OSI, RRT
<i>Xue et al.</i> , 2023[76] <sup>(12)</sup>	CCTA	3D-0D	LCA/RCA	Steady	$MAP = 0.4 \cdot (SBP - DBP) + DBP$	R Pv: 5mmHg	FFR, FFR <sub>CT</sub>

**Table 2.1:** Analysed works. For each study are reported: imaging modality from which the segmentation has been performed, reduced-order model, anatomical geometries that have been considered, steady-state or transient simulation, BCs imposed at the inlet and outlet surfaces and indexes that have been analysed. The subscripts denote which works belong to the same research group. (Pmyo: intramyocardial pressure, Pv: venous pressure, OSI: oscillatory shear index, TAWSS: time-average wall shear stress, RRT: relative resistance time, TAP: time-average pressure).



## 2.2. Boundary Conditions

Inlet and outlet Boundary Conditions (**BCs**) adopted by the different authors are schematically reported in **Table 2.1**.

At the inlet surface pressure or flow-rate have been imposed by the majority of the groups. The waveform or average value were assigned depending on whether the simulation was transient or steady-state. BCs based on either population-average or patient-specific data have been investigated. Some authors decided instead to adopt a more complex inlet BC (i.e. LPM of the heart [29, 65]).

Particular attention should be paid in the choice of outlet BCs. In all of the examined models a reduced order, 0D model was used to include the contribution of the downstream microcirculation that is not included in the coronary artery 3D model. A 0D model is a type of computational model that uses an electric analogue circuit to represent the cardiovascular system. In this model, the resistance to blood flow in vessels is represented as resistors (**R**), while the inertial properties of blood flow are represented by inductors or impedances (**L**). Vessel compliance, which is the ability of vessels to expand and contract in response to changes in blood pressure, is represented by capacitors (**C**). This reduced-order model is also referred to as LPM, as it uses a simplified, lumped approach to represent, in this kind of research focus, the coronary microcirculation. The model is useful for simulating hemodynamic conditions in large and small blood vessels, as well as for predicting the response of the cardiovascular system to changes in HR, blood pressure and other physiological parameters. Overall, the 0D model is a powerful tool for studying cardiovascular physiology and can provide valuable insights into the functioning of the cardiovascular system under various conditions. However, it should be noted that this model is just a simplified representation of the complex cardiovascular system, and as such, its predictions may not be accurate in all situations. Different LPM have been adopted, from simpler ones (i.e. 2-element Windkessel (**2WK**) [38]) to more complex closed loops models [29]. The circuits most frequently used in the literature are reported in **Figure 2.2**.

Suitable modifications such as including a source in the LPM can be implemented to create an out of phase with respect to the systemic circulation. Intramyocardial pressure contribution is important as in the coronary arteries flow and pressure are out of phase and compressive force of the heart acting on the coronary vessels should be included. The intramyocardial pressure contribution is more important in the LCA, as in the RCA the pressure exerted by the right ventricle is lower [38].

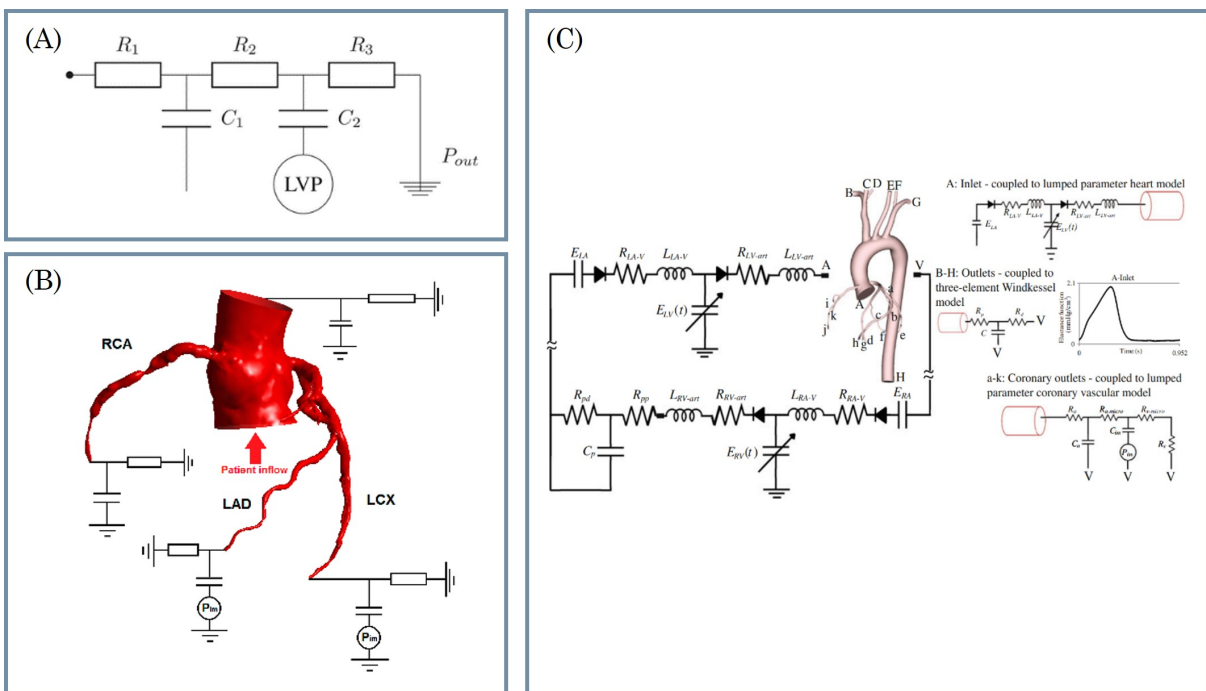


Figure 2.2: Different LPM adopted as outlet BC. (A) RCRCR model by Boileau et al. [6] with the contribution of the intramyocardial pressure. (B) 2WK model adopted by Lo et al [38]. In this case the contribution of intramyocardial pressure is considered only in the left coronary artery as in the right side of the heart the pressure exerted by the ventricle is lower. (C) Closed-loop model proposed by Kim et al [29], the first group to use a LPM to model the outlet BC in a coronary artery tree.

In order to calculate resistance and compliance values, different methodologies have been proposed. Morphometry studies are necessary to correctly determine patient-specific physiological parameters present in the reduced-order model. Generally, resistance and compliance values are subdivided based on total coronary flow-rate and cross-sectional area of the coronary branches. In most of the works, Murray's law was used for flow distribution in the coronary vessels. Once the flow was determined, resistance values in each branch can be calculated using the following relationship:

$$R_i = \frac{\Delta p}{Q_i} = \frac{MAP - P_v}{Q_i} \quad (2.5)$$

in which  $MAP$  is the Mean Aortic Pressure,  $P_v$  is the venous pressure and  $Q_i$  is the flow-rate in each coronary branch. Venous pressure is usually set to 0 or 5 mmHg.

In order to obtain hyperaemic resistance values, resting resistance needs to be multiplied by the Total Coronary Resistance Index (**TCRI**). This coefficient represents the vasodilation of coronary vessels after adenosine administration. In the literature values ranging from 0.16 to 0.30 have been used. According to different studies (i.e. Yin et al. [77]) this index could influence the accuracy in the calculation of  $FFR_{CT}$  as it is representative of the hyperaemic condition usually created in the patient during the invasive procedure. According to the state of the art review, total coronary resistance and compliance values are respectively in the order of  $10^{10} Pa \cdot s/m^3$  and  $10^{-10} m^3/Pa$ .

## 2.3. Results

Among the works presented in **Table 2.1**,  $FFR_{CT}$  was not always compared against the invasive measured FFR (see **Table A.3 Appendix A**), but the authors who did the comparison have shown an high correspondence between the two diagnostic tools, supporting the new challenge of using computational models for the assessment of coronary artery lesions. There are several reasons why this new method has not yet gained popularity in clinical practice, including its high computational demands, long time required to obtain results, and high costs. Recent studies and advancements in computational power have supported the idea that even simpler models could led to accurate  $FFR_{CT}$  results. This is a very important result that should be further studied but, at the same time, the potential that has been demonstrated is already very significant.

### 2.3.1. Impact of Geometry

Starting from the reconstructed geometry, Kwon et al. [33] demonstrated that the model with LCA or RCA alone was computationally more efficient with respect to the one comprising the aorta. It has less mesh nodes and no iterative computation between aorta CFD model and LPM and, most importantly, almost the same results (difference below 2%) in terms of  $FFR_{CT}$  were obtained for the both geometries. Validation against iFFR was achieved as well, with good agreement (difference below 6%). The obtained results for patients with mild, intermediate or severe stenosis are shown in **Figure 2.3**.

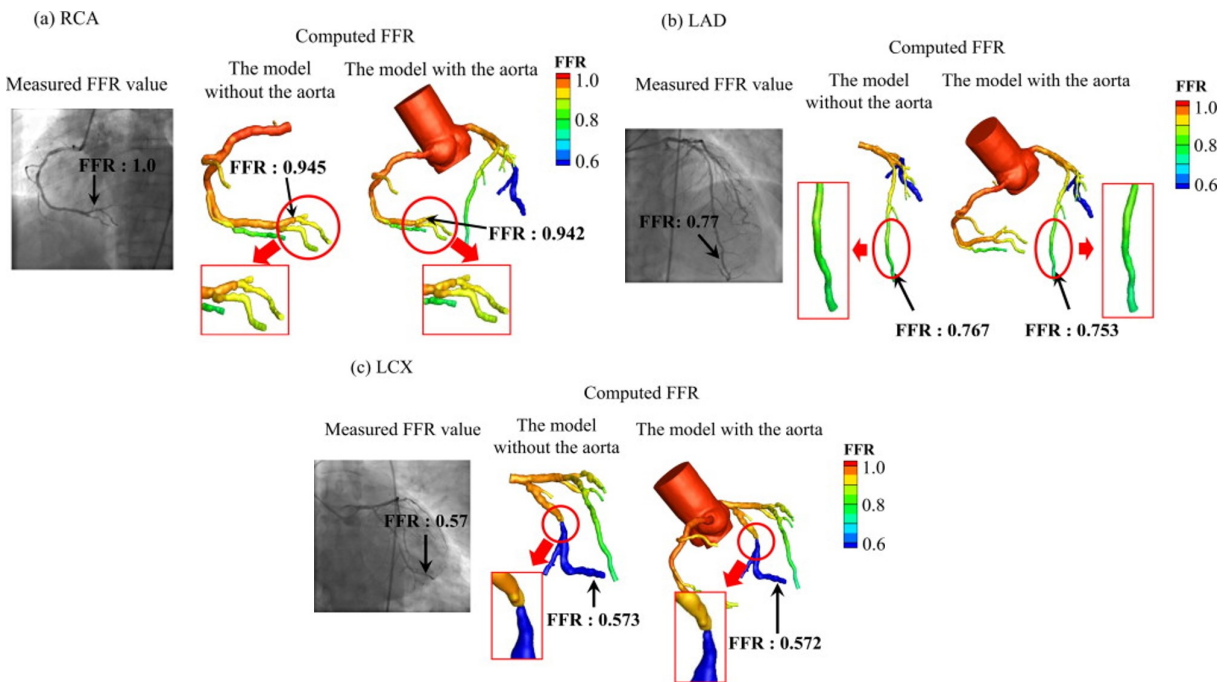


**Figure 2.3:** Comparison between iFFR, obtained by ICA, and  $FFR_{CT}$  in both the models with and without the aorta. The reported results are representative cases for mild (a), intermediate (b) and severe (c) stenosis. In all degree of stenosis a good correlation is shown [33].

Even simpler reduced-order models have been studied: coupling between 1D-0D models have been investigated. At the state of art just few studies have analysed this approach (e.g. Boileau et al [6], Yin et al [77]) but the obtained results are positive, showing that also a 1D model could be used to accurately evaluate  $FFR_{CT}$ . In **Figure 2.4** the  $FFR_{CT}$  map achieved by the two mentioned studies in both 1D and 3D model is reported. Boileau and colleagues created different axisymmetric and non-axisymmetric artificial stenosis in the patient-specific geometry and found out an overall good correlation between 1D and 3D model, with less accurate but not so significant results for  $FFR < 0.80$  (as can be seen in the figure). The conclusion of their study was that stenosis degree and shape are the most critical factors accounting for the difference in the two methods.

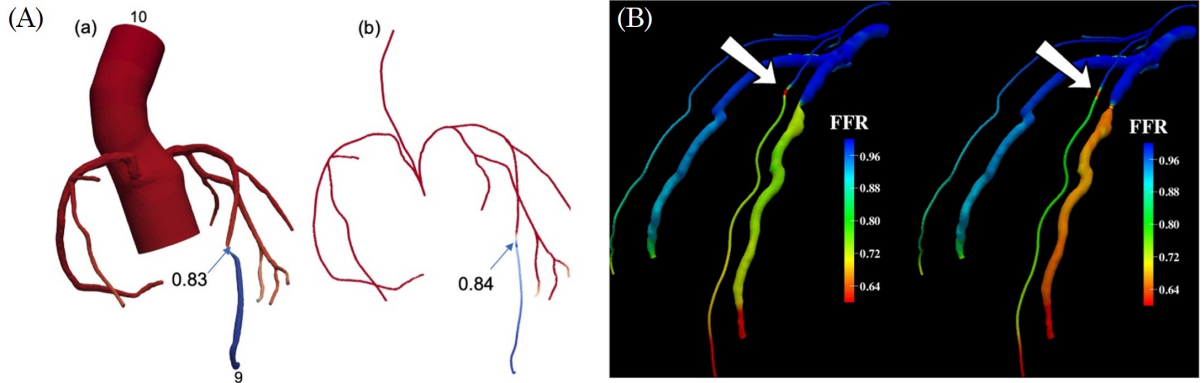


Figure 2.4: Correlation between  $FFR_{CT}$  obtained by the 1D and 3D geometry. (A) Model used by Yin et al [77], considering aorta, LCA and RCA. (B) Boileau et al. [6] results for two different degrees of stenosis. Both the works demonstrated that also the 1D model is able to reproduce accurate results.

Different truncation strategies at the coronary outlets have been adopted in the literature. Shi et al. [60] have studied the influence of subbranches on the accuracy of hemodynamic parameters (e.g. FFR, WSS). The study concluded that the effect of branch removal was very localized if the difference in outflow-rate was  $<5\%$ . The maximum difference resulted to be in the one diameter directly after the cutting position. This led to the deduction that branches can be removed at least five diameters from the region of interest. This results help into reducing the workload and computational power.

### 2.3.2. Impact of Flow Partition Criteria

In order to have realistic and physiological flow-rate and pressure field, proper BCs need to imposed at the outlet surfaces of coronary branches. Flow partition in the coronary vessels is generally done using Murray's law [46], but in the last years different approaches have also been investigated. Herein is e brief description of the adopted methods and the relative obtained results.

Lo et al.[39], have used Positron Emission Tomography (**PET**), the gold standard to assess myocardial perfusion, to understand the local perfusion in the region supplied by each branch. The results have shown that standard morphology based flow subdivision tends to overestimate higher functional severity, especially in patients with reduced vasodilatory response under hyperaemia.  $FFR_{PET}$  have shown higher accuracy with respect to  $FFR_{CT}$ . Specifically, the prediction error using  $FFR_{CT}$  tends to increase as iFFR approaches values  $<0.80$ . It has been proposed that if  $FFR_{CT}$  is ambiguous, a more accurate analysis could be done using PET in order to increase the diagnostic accuracy.

CTP of the hyperaemic state have been used by Xue and colleagues [76] to quantify total hyperaemic coronary blood flow. TCRI resulted to be the most influential parameter in FFR estimation. Hyperaemic coronary flow is an important factor in calculating total coronary outlet resistance and using CTP it is possible to obtain the real physiological state of the specific patient. The study demonstrated that applying CTP on a clinical dataset to calculate hyperaemic flow-rate, increased diagnostic ability of  $FFR_{CT}$  and had a better repeatability.

A different approach was proposed by Tang et al, 2020 [64]. TAG has been used for flow subdivision in the subbranches. TAG is a measure of the linear regression coefficient between the attenuation of contrast medium in the lumen of a coronary artery and the distance from the coronary ostium. It is based on the principle that blood flow in coronary arteries affects the attenuation of contrast medium injected during CCTA. As the contrast medium travels along the artery, its opacification decreases due to the dilution by blood flow. Therefore the rate of change in opacification along the artery is related to the rate of blood flow. Prominent results were reached by this approach.  $FFR_{CT}$  obtained higher specificity, accuracy and area under the curve (AUC) over CCTA and ICA. The method shown a potential diagnostic power in all kind of lesions, comprising intermediate ones, grey zone and patients with high calcium scores. A reference example is shown in **Figure 2.5**.

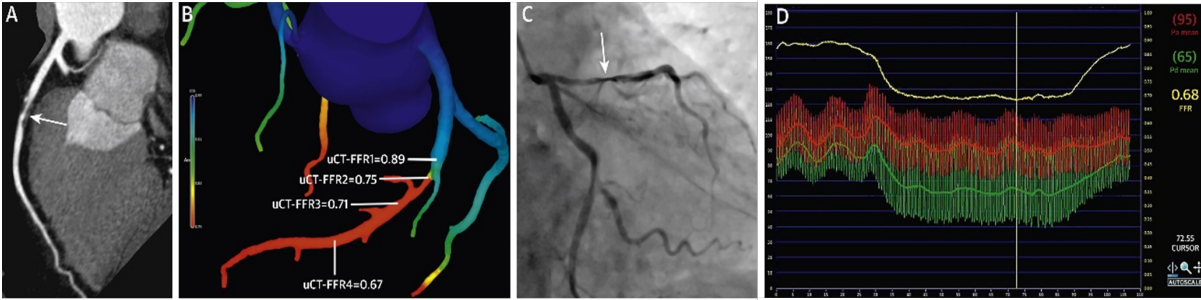


**Figure 2.5:** Results obtained from the simulations run using TAG as a method to distribute the flow-rate in the coronary subbranches. (A) CT-image, (B)  $FFR_{CT}$  map on the coronary tree, (C) ICA image and (D) invasive measured FFR obtained using the pressure-wire and pullback procedure. The results obtained by the computational model agree with the invasive measurement [64].

### 2.3.3. Impact of LPM used as Outlet BC

Most of the works have used an RCRCR model as outlet BC LPM (**Figure 2.2(A)**). Simpler and more complex models have also been examined achieving overall good results when compared against iFFR measurements. Lo and colleagues [38] proposed to use a 2WK,

that is the simplest model that can be used for the purpose of estimating the behaviour of coronary flow in the diastolic phase (as done in the invasive measurement). For this task, the 2WK performs similarly to more complex models. This is related to the fact that the RC model is only able to model the diastolic behaviour as its response is that of an exponential-like discharge of the compliance through the resistance [71]. Some groups have studied the feasibility of using a steady simulation instead of a transient one, with the aim of reducing computational time, and the results are promising. Comparable results have been achieved using the two different simulation approaches. Liu and colleagues [36] (**Figure 2.6**) obtained promising results: the relative error between  $FFR_{SS}$ -FFR was 0.11 and between  $FFR_{SS}$ - $FFR_{CT}$  was 0.067.  $FFR_{SS}$  is the estimation of FFR in the steady-state simulation.

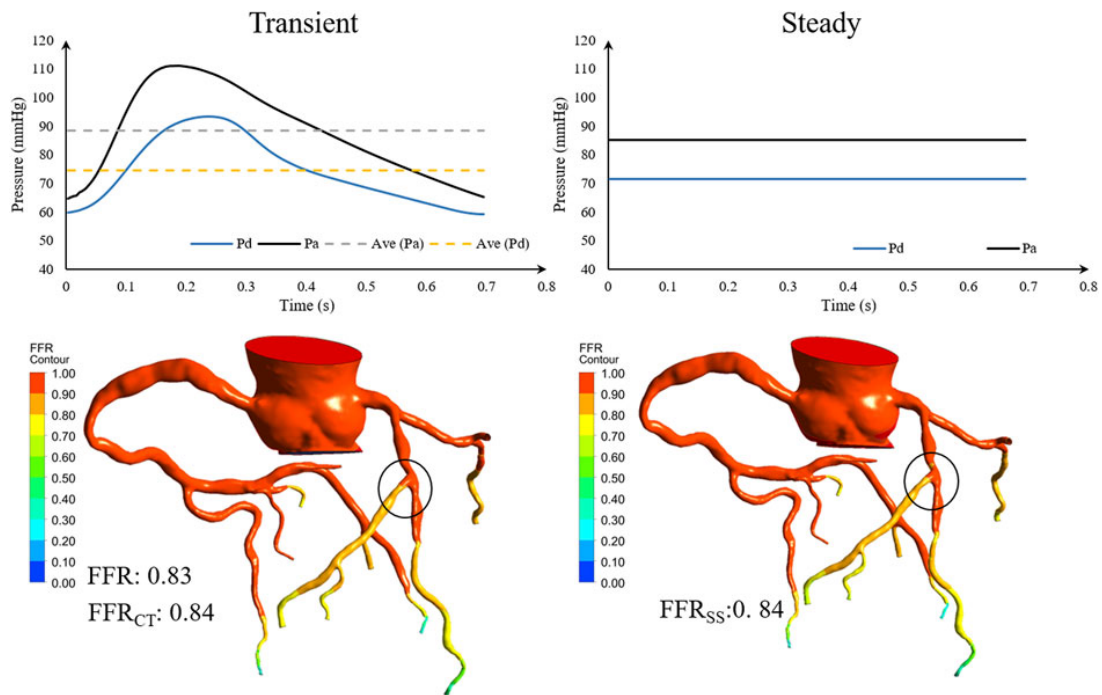


**Figure 2.6:** Comparison between the results obtained by a steady-state or transient simulation with respect also to invasive measured FFR. Both the simulations showed similar results meaning that a simpler and less computational demand model could be used to evaluate the severity of a coronary stenosis.

### 2.3.4. Other Hemodynamic Indices

The hemodynamic index mostly studied is the FFR, but there are also other indices that can help in the identification of coronary significant lesions. Some of these are WSS, iFR, CFR and QFR. Even if their study is not so frequent, their contribution, particularly in lesions close to 0.80, could be very effective. FFR and iFR as pressure-derived indices

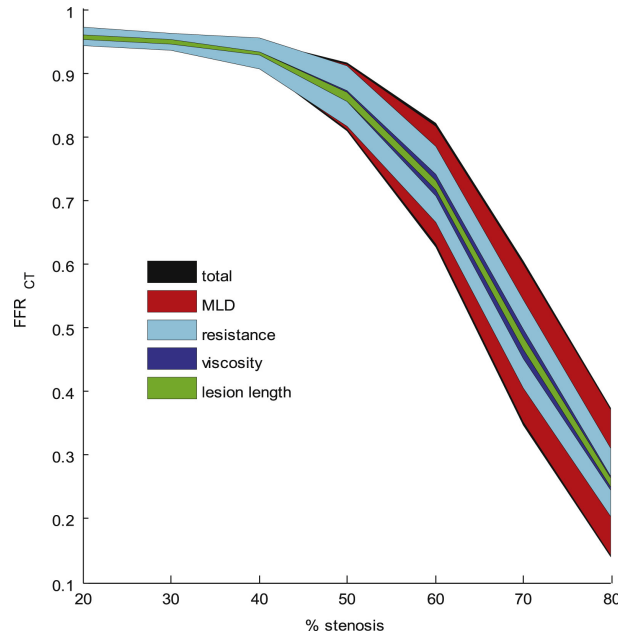


Figure 2.7:  $FFR_{CT}$  for different % stenosis. The influence of the studied parameters in the uncertainty of FFR values is shown. As can be seen, MLD exhibit the highest sensitivity for stenosis  $>50\%$ .

are recommended by clinical practice guidelines such as American College of Cardiology and European Society of Cardiology for decisions on PCI procedures. Stenosis locations are associated with high WSS. High WSS can cause endothelial cells to become damaged, leading to an increase in platelet adhesion and aggregation, which in turns can contribute to the formation of blood clots [33, 62]. Bifurcation sites and areas of high curvature are also considered athero-susceptible regions. These areas are subjected to disturbed flow patterns, which can lead to the accumulation of cholesterol and lipids on the vessel walls, eventually leading to the development of atherosclerotic plaques. The relationship between WSS and atherosclerosis is not yet fully understood but is believed that high WSS can initially cause endothelial cell damage, which can trigger an inflammatory response and build-up of the plaque.

The contribution of different factors as minimum lumen diameter (**MLD**), lesion length (**LL**), boundary resistance and viscosity on the FFR uncertainty has also been analysed. In **Figure 2.7** are reported the results obtained by Sankaran et al. [57] in the ideal model. It has been shown that uncertainty in MLD has the greatest impact on FFR, followed by boundary resistance, viscosity, and lesion length.

Tajeddini and colleagues [62] found out that FFR, iFR and CFR decrease linearly by increasing LL and non-linearly by decreasing MLD. This is due to Hagen-Poiseuille equation. The obtained results are represented by the graphs in **Figure 2.8**.



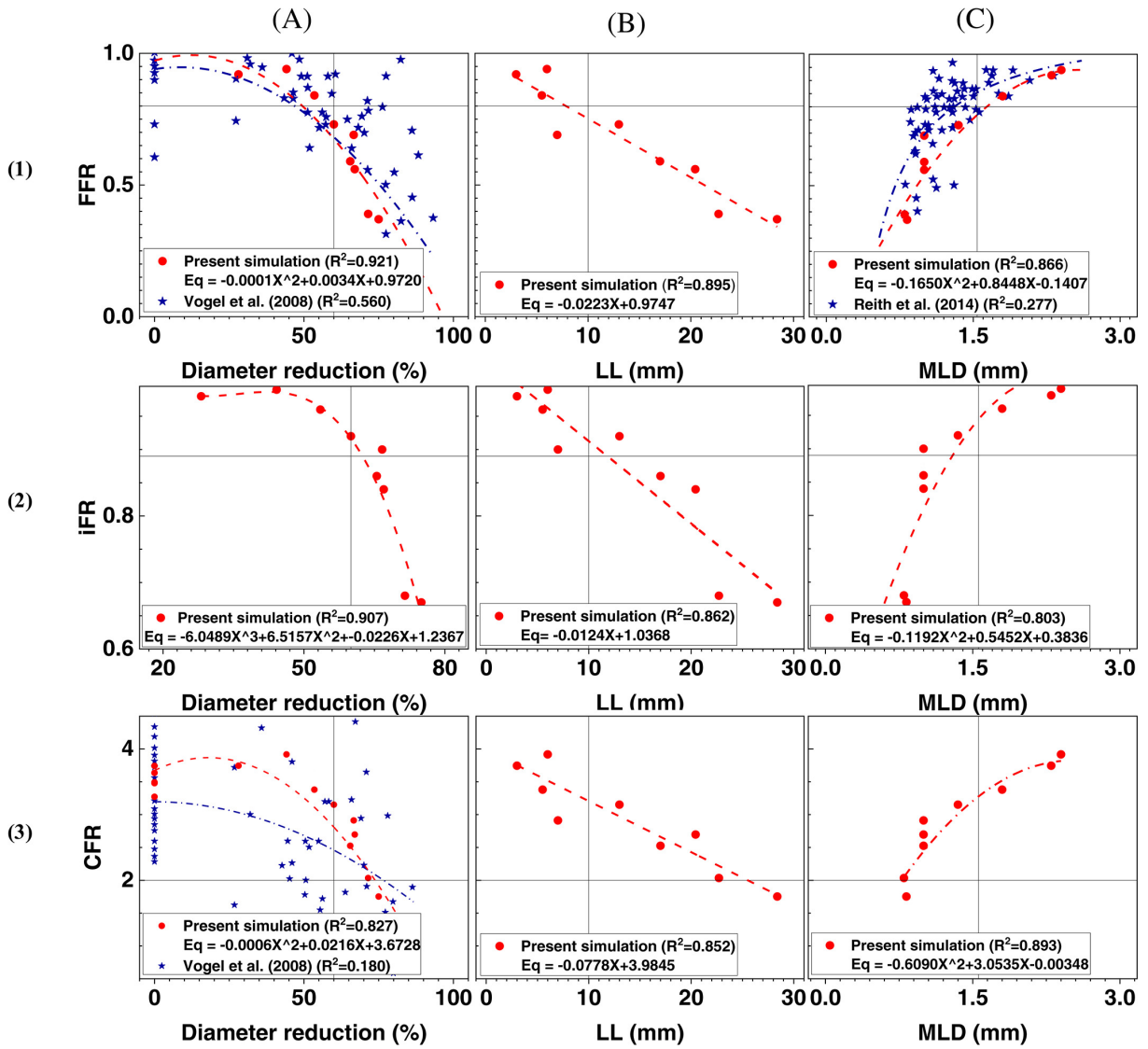


Figure 2.8: Influence of diameter reduction(%), LL and MLD on the different hemodynamic parameters (FFR, iFR and CFR). As can be seen from the reported graphs, the indices decreases with an increase in diameter reduction and LL and a decrease in MLD [62].

The available evidence suggests that the integration of various hemodynamic parameters for evaluating the severity of CAD have demonstrated incremental prognostic value in addition to anatomic stenosis severity. As this approach resulted to increase the diagnostic accuracy, further research is needed to identify the optimal combination of these parameters.

### 2.3.5. Impact of Blood Viscosity

CFD models generally assumed that blood is a Newtonian fluid with constant viscosity. However, blood exhibit a non-Newtonian behaviour especially in small coronary vessels in which stenosis are present. Blood viscosity is not constant and depends on shear rate and in particular blood apparent viscosity lowers at higher shear rates, usually found in small stenotic vessels. In this situation assuming blood to be a Newtonian fluid may lead to inaccurate predictions of flow and pressure. There are different models as Carreau-Yasuda model [8, 67] that could be further examined to incorporate this non-Newtonian behaviour of blood. Yiu et al [77] have demonstrated that especially in mild stenosis blood viscosity highly contributes to FFR uncertainty. Therefore, incorporating a non-Newtonian behaviour of blood into FFR calculations can improve the accuracy of FFR predictions. To the best of the author knowledge, Kwon et al. [33] work is the only one present in literature, in which blood was not modelled as a fluid with constant viscosity value for all the patients but used an equation in which blood viscosity was derived from patient's haematocrit using **Equation 2.6**.

$$\mu = \mu_0(1 + 2.5 \cdot HCT) \quad (2.6)$$

in which  $HCT$  represents patient's haematocrit and  $\mu_0$  is the viscosity of plasma ( $\mu_0 = 0.0015 \text{ kg} \cdot \text{s}/\text{m}$ ). Viscosity is directly related to shear stress but it may or may not affect computed pressure gradient or FFR values [57]. Further research in this area could led to interesting results and an accurate modelling of this parameter could improve the clinical decision-making process in the management of CAD [37, 57, 77].

### 2.3.6. Conclusions on Literature Review

The analysis of the literature revealed that the possibility of obtaining an accurate and simple model is not that far away, and could be accomplished in the next years. Different approaches to reduce the computational time and costs have been implemented and the results have shown comparable results in terms of  $FFR_{CT}$  with respect to the invasive

measured value and more complex and expensive models. This result is important and can be seen as a first-step to be able to include this methodology as a diagnostic tool in clinical practice. 1D and steady-state simulations reduce a lot the computational time bringing it in the order of seconds or few minutes. Further studies should be done but the first results are already promising. More patients with different degrees of stenosis and geometries should be included in future studies and the comparison with the invasive measurement performed in order to validate the proposed method. Something that should be further investigated is the TCRI. Its great influence in the FFR calculation and its variability depending on the geometry of the patient, maximum patient-specific vasodilation and presence of pathologies has been demonstrated. A relationship between patient-specific HR in the hyperaemic condition and TCRI have been proposed by Sharma et al. [59]. Patient-specific TCRI could be calculated as follow:

$$TCRI_{corr} = \begin{cases} 0.0016 \cdot HR_{hyp} + 0.1 & \text{if } HR_{hyp} \leq 100\text{bpm} \\ 0.001 \cdot HR_{hyp} + 0.16 & \text{if } HR_{hyp} > 100\text{bpm} \end{cases} \quad (2.7)$$

In order to have an accurate representation of patient-specific physiology of coronary arteries, great attention should be paid in all the steps, particularly in the segmentation process and in the proper choice of BCs. Inaccurate values of LPM parameters, pressure and flow-rate would led to a wrong estimation of the hemodynamic parameters of interest.

## 2.4. Aim of the Thesis

Non-invasive  $FFR_{CT}$  calculation based on CFD simulations using patient-specific anatomical models is a promising approach for assessing the hemodynamic significance of coronary artery stenosis. However, there are still some limitations and challenges that need to be overcome before it can be widely adopted in clinical practice. One of the major challenges is the complexity of the process. Generating patient-specific anatomical models from medical images is a complicated task which can be challenging in case of complex geometries, calcium artifacts or low CT-image resolution. The interpretation of CCTA requires highly trained readers to ensure diagnostic accuracy and minimize interobserver variability. In addition, CFD simulations can be time-consuming and require high computational resources, which limits their clinical applicability. Another important consideration is the choice of BCs used in the simulations, especially at the outlet surfaces, which should be carefully chosen to replicate physiological flow conditions. Inaccurate BCs can lead to erroneous results, and therefore, the choice of BC should be based on physiological data and patient-specific information. Lastly, the accuracy of the 3D model is crucial, as the

Navier-Stokes equations are solved in a complex and irregular geometry. The resolution of the NSEs depends on the quality of the mesh used, and therefore, it is important to ensure that the mesh is sufficiently refined to capture the flow features accurately.

Considering the promising results obtained in the literature, and the interest in incorporating  $FFR_{CT}$  analysis in a routine clinical setting, the simulation should be as simple and as fast as possible. The aim of this thesis work is to test different approaches for coronary flow CFD simulations and study the feasibility and accuracy of using simpler yet efficient models in the calculation of  $FFR_{CT}$ . For this purpose, we incrementally simulated more complex scenarios, starting with ideal geometries of different degree of stenosis coupled to boundary conditions based on average population pressure and flow data; proceeding with patient-specific geometries reconstructed from CCTA of patient with different degree of stenosis, from mild to severe, coupled with both average population-based and patient-specific boundary conditions. Since diagnostic indexes as FFR are based on average values over the cardiac cycle, with the aim of reducing the computational time, the possibility of using a steady-state simulation instead of a transient one would be investigated. To validate the developed models, the computed  $FFR_{CT}$  will be compared against the invasive-measured FFR value.

# 3 | Materials and Methods

Based on the review of the literature,  $FFR_{CT}$  seems to have the potential to replace the current gold standard for predicting the hemodynamic significance of a coronary stenosis. By providing non-invasive and cost-effective options, this technique could facilitate the diagnosis process and help tailor treatment decisions to individual patients. Different CFD models have been developed, however HeartFlow company software is the only FDA approved and available in clinical practice. One of the main limitation of HeartFlow analysis is the time required for a complete analysis ( $\sim 1$  day) and the non-negligible cost, which can be prohibitive for some patients and healthcare providers.

The present study conducted a comprehensive review of the current non-invasive methods for calculating  $FFR_{CT}$ , with a specific emphasis on less complex models that are computationally efficient. Since a stenosis FFR is measured as the time-averaged ratio of distal over proximal pressure, the primary objective of the study was to investigate the feasibility of using a steady-state simulation instead of a transient one. The analysis was performed for two different types of geometries:

1. Idealized pipe in which different degrees of stenosis were introduced, from mild to severe;
2. CCTA-derived patient-specific geometry of the coronary arteries.

To study the impact of patient geometry alone on the precision of  $FFR_{CT}$ , while disregarding the variations arising from patient-specific BCs, two sets of simulations were conducted. In the first set, BCs based on average population pressure and flow data were imposed, in the second one BCs based on patient-specific data were investigated (**Figure 3.1**). In both cases, a consistent schematic procedure, which will be detailed later, was employed to obtain the desired index.

In all the simulated models, a pressure wave at the inlet and a LPM at the outlet were chosen as BCs.

Among a dataset consisting of 10 CCTA, four subjects were retrieved, based on the iFFR measured (0.94 to 0.57) in order to have a dataset sufficiently representative of the degree

of stenosis variability (**Table 3.1**). The four CCTA were used to reconstruct patient-specific coronary artery geometries and simulate the blood flow in the coronary arteries. The associated iFFR value was used to validate the developed models. Further details on the chosen subjects are reported in Section 3.2.5.2.

Patient ID	Coronary Artery	iFFR	Selected Patients
6	RCA	0.57	✓
8	LAD	0.63	
6	LM	0.68	
1	LAD	0.76	✓
7	LAD	0.77	
7	LCX	0.78	
7	RCA	0.79	
10	LAD	0.83	✓
3	LAD	0.86	
4	LAD	0.86	
5	LAD	0.87	
6	LCX	0.87	
2	LAD	0.88	
9	RCA	0.94	✓
2	LCX	0.96	

**Table 3.1:** Patients with related iFFR measurement. Patients were subdivided according to the degree of stenosis. From severe to mild:  $\text{FFR} \leq 0.7$  (red),  $0.70 < \text{FFR} < 0.80$  (orange),  $0.80 < \text{FFR} < 0.90$  (yellow),  $\text{FFR} \geq 0.90$  (green). One patient from each group was randomly selected.

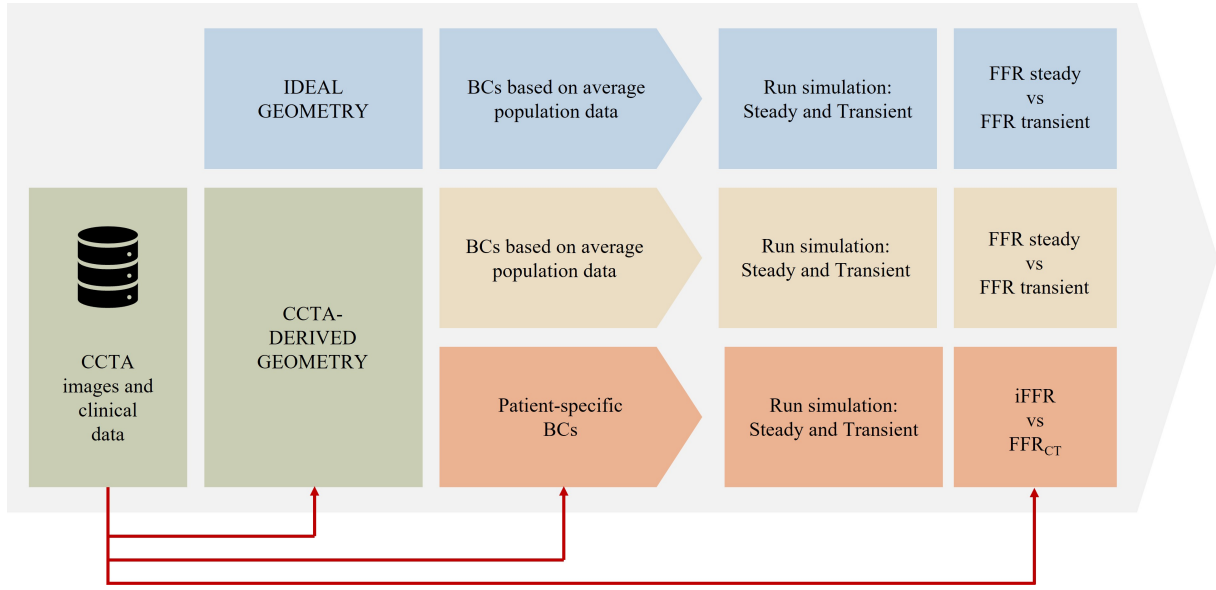


Figure 3.1: Summary of the different models and BCs investigated.

### 3.1. Ideal Geometry

The ideal geometry was designed using the Space Claim CAD (Ansys, Canonsburg, CA, United States) software. Different degrees of stenosis were modelled, specifically, 50%, 60%, 70%, 75% and 80%. The pipe diameter was chosen equal to 3 mm (i.e., the average diameter of the left coronary artery) and the lesion length was set to 6 mm. The degree of stenosis was defined as follow:

$$d_s = d \left(1 - \frac{\%s}{100}\right) \quad (3.1)$$

where  $d_s$  is the diameter in the stenosis region,  $d$  is the pipe diameter and  $\%s$  is the degree of stenosis (expressed as percentage).

The geometry was then meshed using Ansys embedded meshing tool. After a sensitivity analysis, the chosen element size was set to 0.25 mm (based on similar works in the literature) with a body sizing reduction of 0.125 mm in the stenosis region (defined by a 5 mm radius sphere centred in the middle of the stenosis) and three inflation layers with a maximum thickness of 0.3 mm were generated (**Figure 3.2**).

Blood flow velocity and pressure fields were obtained solving incompressible NSEs. Blood was modelled as a Newtonian fluid with a constant viscosity  $\mu = 0.003 \text{ Pa} \cdot \text{s}$  and density  $\rho = 1060 \text{ kg/m}^3$ . At the walls a no-slip condition was enforced, representing a rigid ideal vessel. The inlet and outlet BCs will be discussed in the next paragraph.

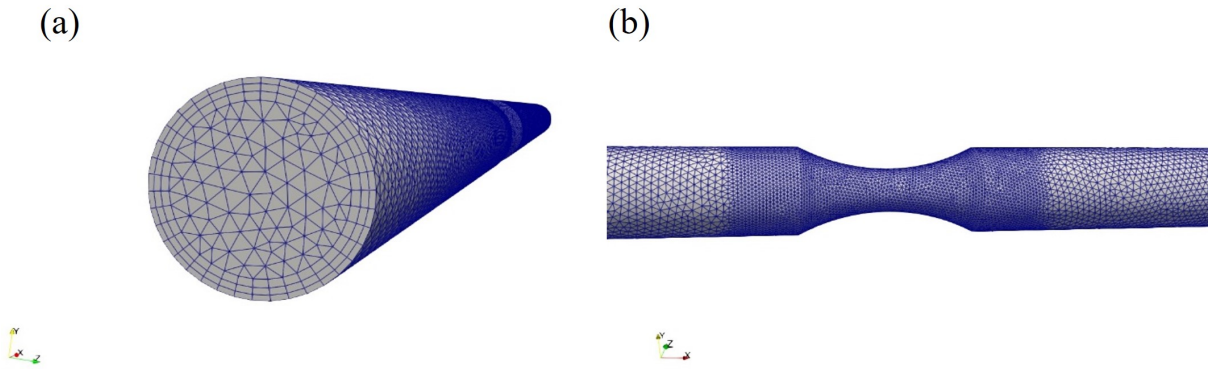


Figure 3.2: Mesh of the ideal geometry with a 50% of stenosis. (a) shows the mesh boundary layer in the inlet section. (b) shows the refinement of the mesh in the stenosis region.

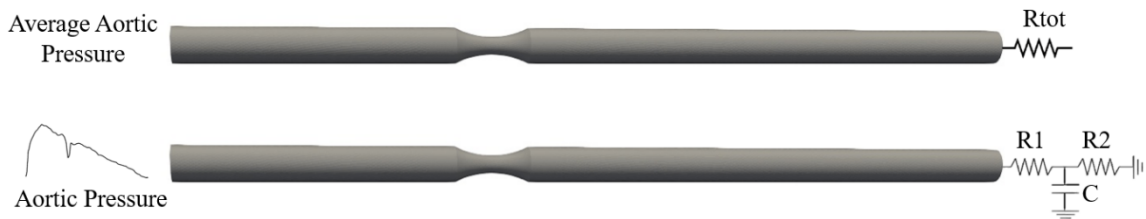


Figure 3.3: Ideal geometry with specified the imposed boundary conditions for either the steady or transient simulation.

### 3.1.1. Boundary Conditions

In order to have a realistic estimation of the FFR value, great attention is needed in the choice of the boundary conditions. Depending on the type of the simulation (i.e., steady or transient), different BCs were used (**Figure 3.3**). In general, BCs were imposed at the boundaries of the domain through a User-defined function (**UDF**). A UDF is a custom function that can be loaded in Ansys Fluent solver to enhance the standard features of the code.

**Quasi-steady simulation.** As inlet BC the mean aortic pressure was applied. Trying to replicate the ideal model developed by Taylor and colleagues [65], a pressure of 90 mmHg was imposed at the inlet surface. When considering the outlet BC, it is important to account for the hyperaemic state induced in the patient during the invasive procedure. To recreate this state, the resting flow-rate was increased by four-folds. A LPM consisting of a resistance was imposed at the outlet surface. The resistance value was taken from Taylor et al. [65]. A venous pressure of 0mmHg was considered.

**Transient simulation.** As inlet BC a literature pressure waveform with a mean pressure



of 90 mmHg was applied. Taking into account the outlet BC, as LPM an electrical circuit corresponding to the 3-element Windkessel (**3WK**) model, was imposed [71]. A 3WK model is an RCR model, consisting in a proximal resistance ( $R1$ ) in series with a parallel arrangement of a capacitance ( $C$ ) and a distal resistance ( $R2$ ). The electrical circuit analogue is shown in (**Figure 3.4**).

The total resistance was set equal to the resistance value used in the steady simulation, then it was split between proximal and distal resistance based on a 3:7 ratio [56]. Compliance value was set equal to literature value from [77]. Resistances and compliance values were finally optimized using Excel (Microsoft, Redmond, Washington, United States) by minimizing the error between the resulting flow obtained for the prescribed inlet pressure wave and a physiological flow-rate waveform of the left coronary artery (**LCA**).

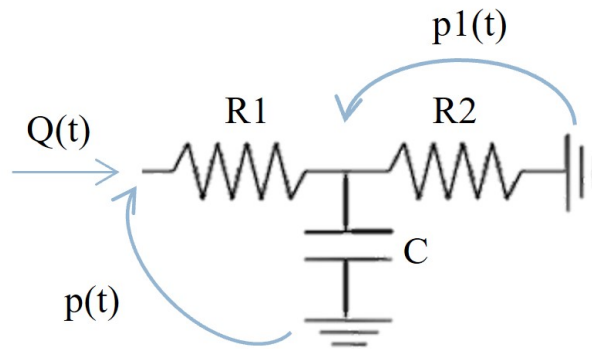


Figure 3.4: 3WK LPM imposed as outlet boundary condition.

### 3.1.2. Computational Scheme and Parameters

The transient simulation was run for 5 cardiac cycles. A fixed time-step of 0.001 s was assigned while limiting to 200 the max number of iterations per timestep. The initialization was computed from the inlet with a velocity of 0.5 m/s. For the simulation the Semi-Implicit Method for Pressure Linked Equations (**SIMPLE**) scheme was used and under-relaxation factors (**URF**) were set to 0.7 for the pressure and 0.3 for the linear momentum. The convergence criteria adopted was a residual of  $10^{-5}$  for both the continuity and the velocity components. Results were post-processed and analysed using Paraview (Kitware, Clifton Park, New York, United States). FFR was calculated in each section of the pipe as the ratio between the pressure along the pipe and the inlet pressure. The difference between the FFR calculated in the steady and transient simulations was also examined.

## 3.2. Patient-Specific Geometry

The adopted workflow used to estimate  $FFR_{CT}$  value from patient-specific coronary artery geometry was devised as shown in **Figure 3.5**.

### 3.2.1. CT-image Acquisition

This study was retrospectively performed on a pool of patient who underwent CCTA scan for anatomical assessment of their coronary vessels. Overall, 10 CCTA scans were retrospectively collected from Centro Cardiologico Monzino (Milan, Italy). Images were acquired with a GE Medical System (Boston, MA, United States) machine with a mean voxel size of  $0.365 \times 0.365 \times 0.650 \text{mm}^3$  and a resolution of  $512 \times 512 \times 256$  in the sagittal, coronal, axial direction, respectively. Three acquisitions were conducted using different methods: *i*) at 40% and 75% of the cardiac cycle; *ii*) the average between 40-80% of the cardiac cycle; *iii*) the SMART sequence which was the time average of the first two acquisitions aimed at eliminating possible artifacts. Whenever possible, the SMART sequence was utilized, otherwise, the one with the best quality was selected. The contrast and brightness of the original Digital Imaging and Communications in Medicine (DICOM) data were manually adjusted to enhance the visibility of the coronary arteries. The present study was performed in accordance to recommendations of the Centro Cardiologico Ethics Committee, with written informed consent from all subjects, in accordance with the Declaration of Helsinki.

### 3.2.2. CT-image Segmentation and 3D Anatomy Reconstruction

Segmentation of LCA, RCA and aorta was performed from CT images acquired by Centro Cardiologico Monzino of Milan. In particular 10 patients anatomies have been reconstructed. The segmentation was achieved using 3DSlicer (version 4.11) [1, 18], a software application for visualization and analysis of medical image computing data sets. The procedure followed these steps: (i) identification of the calcified plaque regions setting an high ( $>600$ ) Hounsfield units (**HU**) intensity threshold; (ii) manual annotation of the segments of interest in some slices of the CT images; (iii) interpolation between slices and *grow from seeds* semi-automatic algorithms were used to complete the segmentation. Regarding the plaque identification, only calcified plaques could be recognized by high attenuation values. Non calcified plaques (i.e fibrotic plaques) were identified by manually passing all the CT- slices. An example of how calcified or non-calcified plaques can be

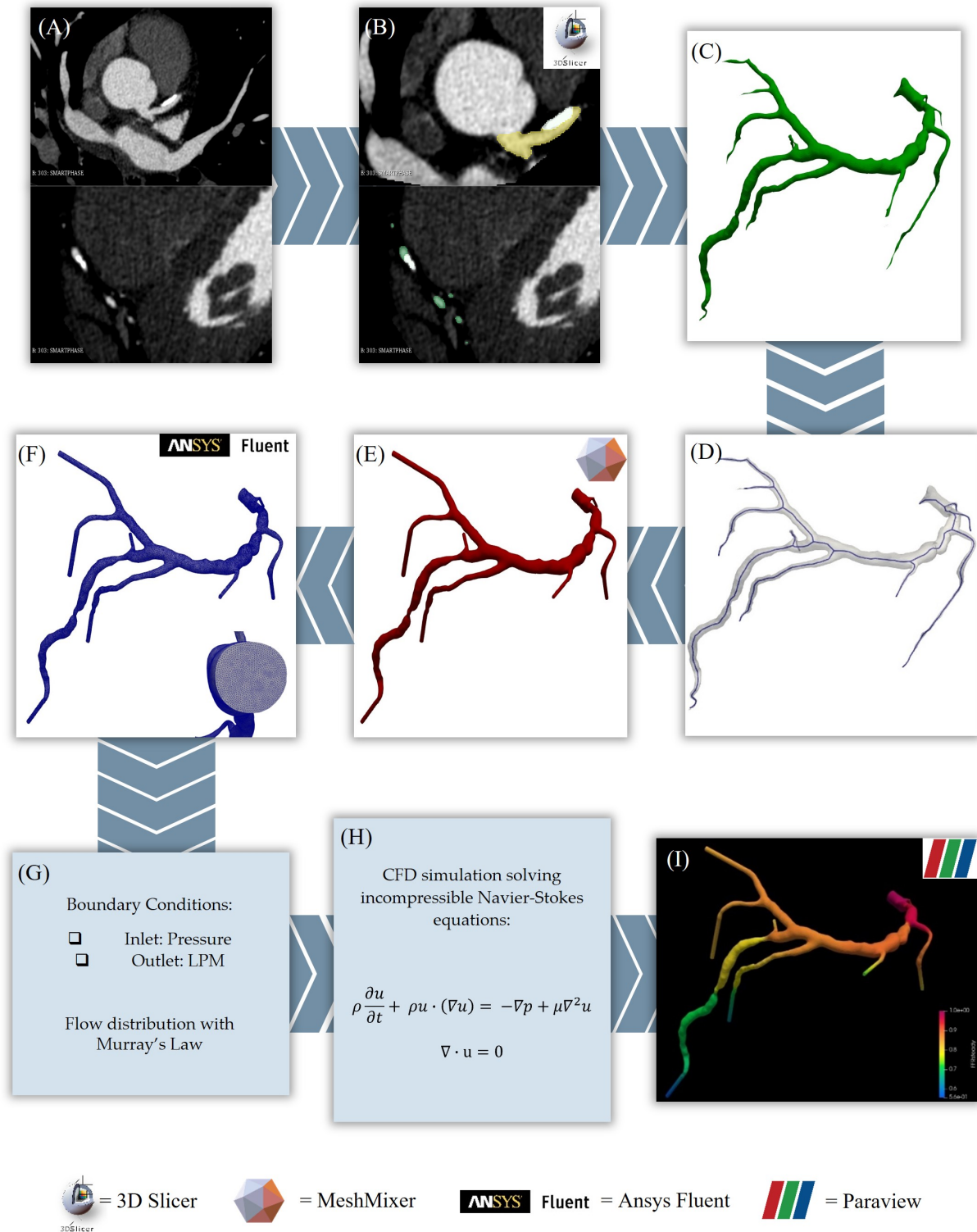
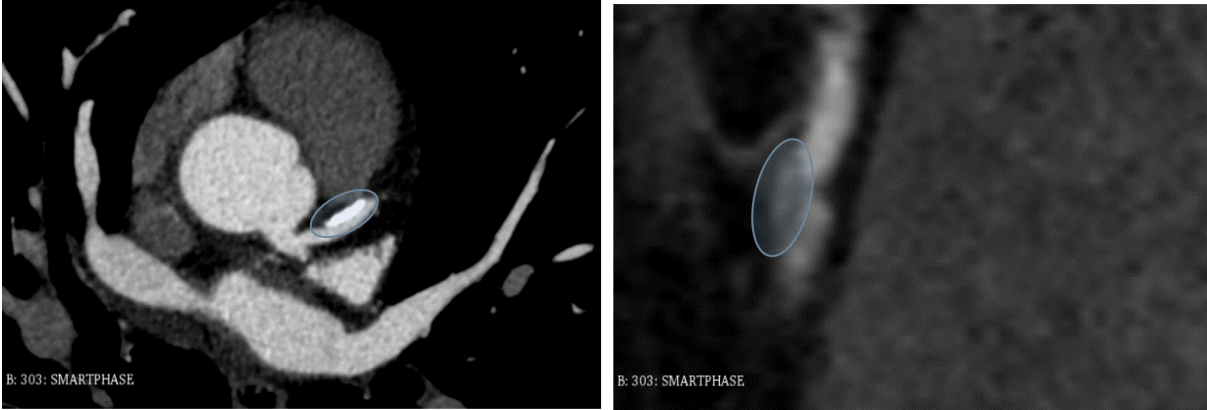


Figure 3.5: Workflow adopted to estimate the  $FFR_{CT}$  starting from medical CT images. (A) CCTA images. (B) Segmentation of LCA (in yellow), RCA (in green) and plaque (in white). (C) 3D model reconstruction. (D) Centreline extraction. (E) Refined geometry ready to be meshed. (F) Meshed geometry. (G) Imposition of appropriate boundary conditions. (H) CFD simulations and (I) analysis of the obtained results. (I) represents the FFR map for a patient with a severe degree of stenosis.

visualized in CT-images is reported in **Figure 3.6**.



**Figure 3.6:** Difference between calcified (on the left) and non-calcified plaque (on the right) in CT-images from the dataset used in this study.

After having obtained a first rough reconstruction of the patient geometry, a smoothing Gaussian filter was applied (standard deviation = 0.35 mm) in order to remove extrusions and refine the whole geometry. The segmentation mask, consisted in three different labels: LCA, RCA and Plaque.

It has been demonstrated that using either a more complex model with the aorta, or a more simplified one, lead to comparable results [33], thus, to perform CFD simulations the LCA or RCA geometry only, depending on the location in which the iFFR was measured, was considered. Finally, the coronary centrelines were extracted and the geometry was exported and saved as STL file.

The raw patient geometry was cut at the inlet and outlet surfaces with planes perpendicular to the centreline in Paraview 5.10.1. The inlet surface was obtained with a cut at the level of the coronary ostium. Prior to performing the cut to define the coronary outlet surfaces, all the branches with a diameter lower than 0.9 mm were removed, as CCTA resolution ranged from 0.3x0.3 mm in-plane to 0.7 mm through-plane, and thus vessels with diameter <0.7 mm cannot be accurately detected. The resulting geometry was then imported in MeshMixer (Autodesk, San Rafael, California, United States). Here the surface of the coronary vessel was smoothed and remeshed where the aspect ratio was too high. The geometry was verified to have a volume difference less than or equal to 3% compared to the segmented geometry. Finally, the coronary outlets were extruded in normal direction by  $\sim 10$  diameters to limit the effect of the imposed BCs [60]. The obtained geometry was then ready to be meshed.

### 3.2.3. Meshing

Once the 3D model of the coronary arteries was obtained, the geometry file was imported in ANSYS. A tetrahedral element mesh was generated using ANSYS Meshing tool. A sensitivity mesh analysis was conducted, using the coronary geometry of Patient-9, to define the most appropriate element size. In particular three different meshes were analysed, from coarser (0.25 mm) to finer (0.07 mm) meshes. A steady-state simulation was run imposing a velocity of 0.4 m/s and a zero pressure at the outlet branches. A mesh example is reported in **Figure 3.7**.

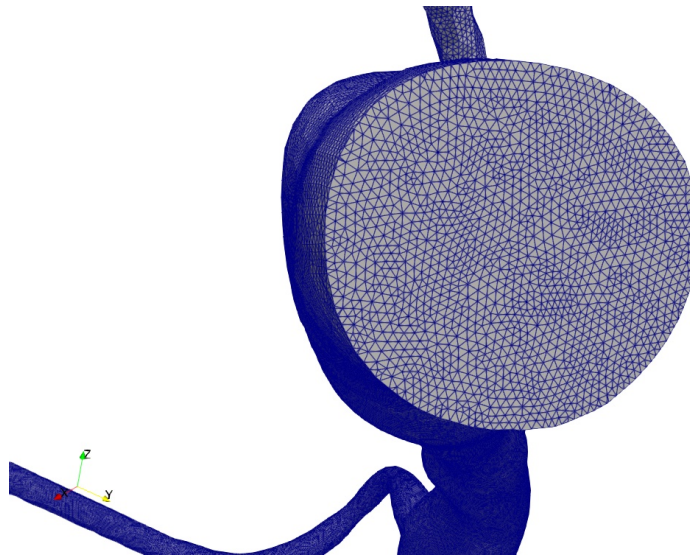


Figure 3.7: Inlet surface of a patient-specific coronary geometry. The applied mesh had a max element size of 0.1 mm.

### 3.2.4. Material Properties

In order to solve the Navier-Stokes equations, blood and flow properties had to be defined. The flow was assumed to be laminar and incompressible, while the blood was assumed to behave as a Newtonian fluid. Blood density was set to  $1060 \text{ kg/m}^3$  and  $0.0035 \text{ Pa} \cdot \text{s}$  was the value associated to blood viscosity.

### 3.2.5. Boundary Conditions

Two different BCs were applied and analysed. For either the first or the second method a pressure at the inlet surface and a LPM at the outlet branches were imposed.

### 3.2.5.1. BCs based on Average Population Pressure and Flow Data

In the first set of simulations, average literature data for pressure and coronary flow-rate were used to estimate the  $FFR_{CT}$ , with the aim of comparing the results obtained with a steady and a transient simulation.

#### *Inlet BC*

At the inlet surface a pressure BC was imposed for either steady or transient simulations. Considering average literature data, a pressure waveform ranging from 80 to 120 mmHg, with a period of 800 ms was set in all the patients. For the steady simulation, the average value of the curve (i.e., 100 mmHg) was imposed. The inlet pressure waveform was fitted in MATLAB by using a 8-terms Fourier series (**Figure 3.8**). The Fourier series is a sum of sine and cosine functions that describes a periodic signal and it is represented as:

$$y = a_0 + \sum_{i=1}^N a_i \cdot \cos(i\omega x) + b_i \cdot \sin(i\omega x) \quad (3.2)$$

The obtained Fourier coefficients were then imported in the UDF implemented to assign personalized BC in Fluent.

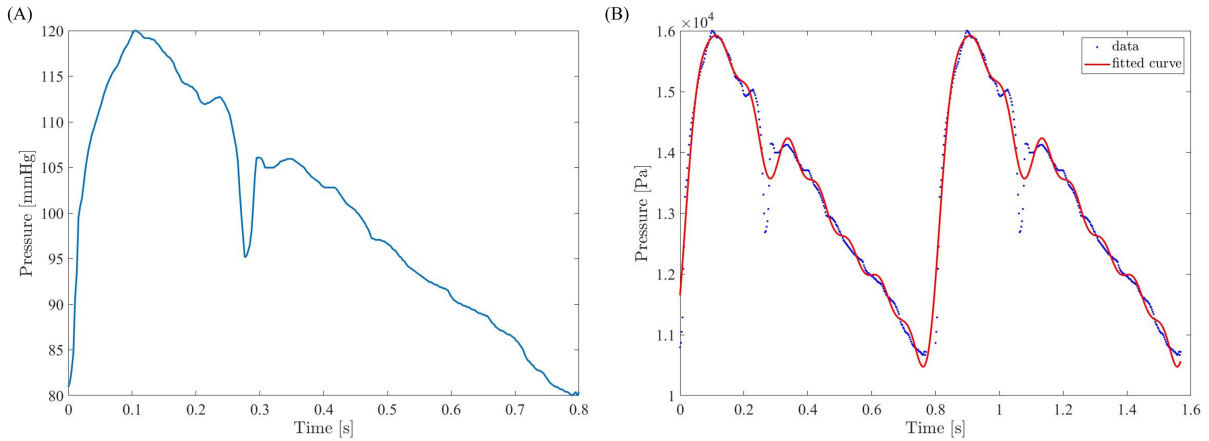


Figure 3.8: (A) Pressure-curve imposed at the inlet BC when using average literature data. (B) Approximation of the pressure-curve with Fourier coefficients.

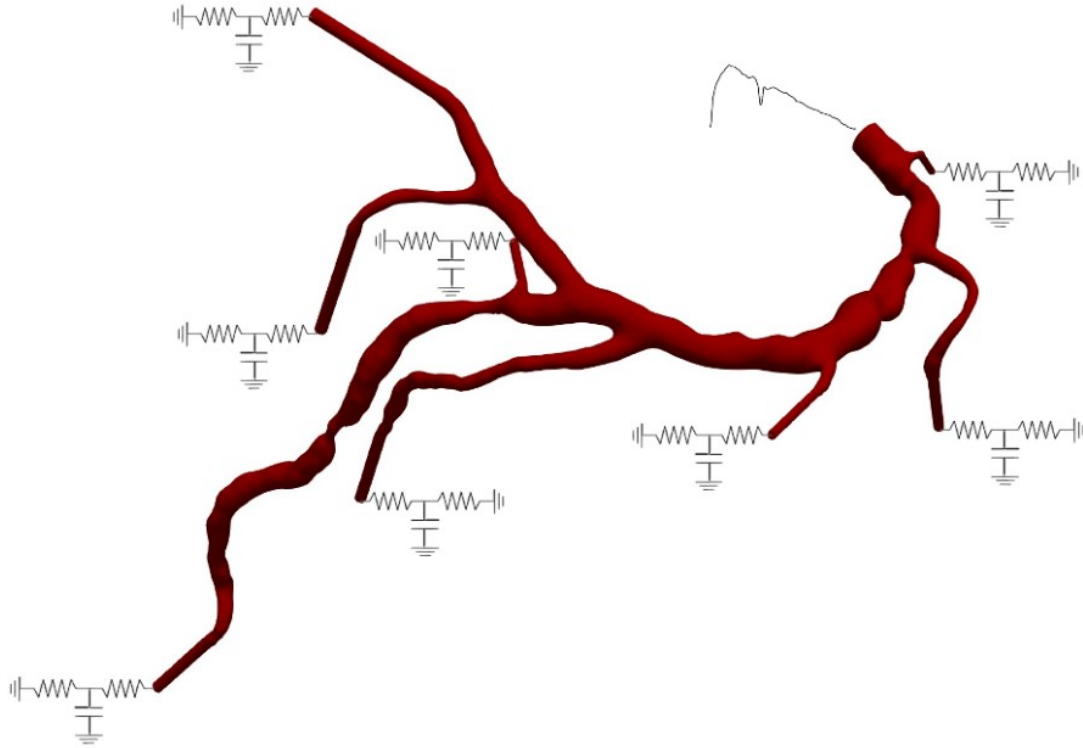


Figure 3.9: Inlet and outlet BC assigned at the boundaries of the domain in the transient simulations. Specifically, a pressure curve at the inlet surface and a 3WK model at the outlet boundaries.

### *Outlet BC*

A LPM was applied as BC at the outlet surfaces of the coronary branches. The literature indicates the use of different models, ranging from the basic 2-element Windkessel to more complex models with multiple resistances and compliances. In this study, an intermediate model, specifically the 3WK model, was employed to represent the removed downstream microcirculation (**Figure 3.9**). In this model, the venous pressure was assumed to be 0 mmHg, and the intramyocardial pressure was not accounted for.

The set of ODEs that fully describes the response of the circuit shown in **Figure 3.4** to an input is the following:

$$\begin{cases} q(t) = \frac{p1(t)}{R2} + C \frac{dp1(t)}{dt} \\ p(t) = p1(t) + R1 \cdot q(t) \end{cases} \quad (3.3)$$

which can be sum up in the governing equation:

$$\frac{dp(t)}{dt} + \frac{p(t)}{C \cdot R2} = R1 \frac{dq(t)}{dt} + \frac{R1 + R2}{R2 \cdot C} q(t) \quad (3.4)$$

The governing equation was the discretized with Backward Euler Method obtaining the following:

$$P_i = \frac{[(R1 + R2 + R1 \cdot \beta)Q_i + \beta \cdot P_{i-1} - R1\beta Q_{i-1}]}{(1 + \beta)}, \quad \beta = \frac{R2C}{\Delta t} \quad (3.5)$$

In order to determine resistance values, the first step is the estimation of total coronary flow. Flow rate in coronary arteries is approximately 4% of CO thus considering a CO of 6 lpm, the adopted resting coronary flow was 250 ml/min. The flow was then subdivided in LCA and RCA with a 6:4 [6, 77] proportion resulting in left total coronary flow ( $Q_{LCAtot}$ ) equal to  $2,5 \cdot 10^{-6} \text{ m}^3/\text{s}$  and right total coronary flow ( $Q_{RCAtot}$ ) corresponding to  $1,67 \cdot 10^{-6} \text{ m}^3/\text{s}$ . In order to reproduce the max hyperaemic condition, the literature works increased the resting flow-rate by 3.5 to 4.5 folds. In this study resting coronary flow was increased by 4-folds.

Flow distribution in each coronary branch was performed according to Murray's Law [46]. Resting coronary flow was then multiplied by four to recreate the hyperaemic condition. Pressure drop in coronary arteries is usually small, thus coronary artery pressure was set to Mean Aortic Pressure (**MAP**). Using Poiseuille equation, each coronary outlet total resistance can be calculated as follow:

$$R_i^{hyp} = \frac{MAP - P_v}{Q_{out_i}^{hyp}} \quad (3.6)$$

$R_i^{hyp}$  was set as initial value for the total resistance of each branch. This value was then subdivided in the proximal and distal resistance with a 3:7 ratio [56]. Total compliance value for either LCA and RCA was taken from the literature. The order of magnitude was  $10^{-10} \text{ m}^3/\text{Pa}$  in all the analysed works. In accordance to Yin et al.[77] study, total coronary LCA and RCA compliances were set respectively to  $2.5 \cdot 10^{-10} \text{ m}^3/\text{Pa}$  and  $3.6 \cdot 10^{-10} \text{ m}^3/\text{Pa}$ . Total coronary compliance was then subdivided in the coronary branches according to their cross-sectional area ( $C \sim A_{branch}$ ), using the following formula:

$$C_i = C_{tot} \frac{A_i}{\sum_{i=1}^N A_i} \quad (3.7)$$



in which  $A_i$  is the average cross-sectional area of the  $i_{th}$  vessel,  $C_{tot}$  is the total coronary compliance and  $N$  is the number of branches.

Once resistances and compliance values were obtained, they were set as initial values of the optimization of the LPM parameters.  $R_1$ ,  $R_2$  and  $C$  needed to be optimized to obtain a flow-rate waveform with an average value approximately equal to the flow calculated with Murray's Law. With this aim a customized MATLAB code was implemented.

The new resistances and capacitance values were then imported in the UDF. In the UDF the pressure for each outlet was calculated using the previously described governing equation of the 3WK. In conclusion, for the transient simulation  $R_1$ ,  $R_2$  and  $C$  values obtained after the optimization have been used. For the steady simulation instead, a total resistance was calculated by the sum of the optimal proximal and distal resistances.

### 3.2.5.2. BCs based on Patient-Specific Data

Finally, the impact (on  $FFR_{CT}$ ) of determining BCs variables based on the available patient-specific data was investigated. The available data for each patient were: gender, age, weight, height, minimum and maximum aortic pressure, heart rate at rest and under hyperaemic condition. In **Table 3.2** and **Table 3.3** are reported the data for each patient and the value of the invasively measured FFR.

<b>PATIENT</b>	<i>Coronary Artery</i>	$iFFR$	$HR_{rest}$ [bpm]	$HR_{stress}$ [bpm]	<i>Aortic Pressure</i> [mmHg]
9	RCA	0.94	59	74	135/65
10	LAD	0.83	60	69	130/80
1	LAD	0.76	59	99	132/85
6	RCA	0.57	51	95	160/85

Table 3.2: Available patient-specific data.

<b>PATIENT</b>	<i>Gender</i>	<i>Age</i>	<i>Weight</i> [Kg]	<i>Height</i> [cm]
9	F	66	53	159
10	M	46	82	175
1	M	62	88	182
6	M	49	72	172

Table 3.3: Available patient-specific data.

***Inlet BC***

For steady simulations, MAP has been calculated based on a relationship found in the literature [59] as a function of HR, SBP and Diastolic Blood Pressure (**DBP**). The considered formula was the following:

$$MAP = DBP + \left[ \frac{1}{3} + (HR \cdot 0.0012) \right] \cdot (SBP - DBP) \quad (3.8)$$

For the transient simulations instead, the pressure wave adopted in the simulation with BCs based on average population data was scaled for each of the simulated subjects in order to match the SBP, DBP and the HR clinically measured.

Considering the patient-specific coronary flow-rate, two different strategies have been implemented in order to estimate it. The available data did not include a patient-specific CO thus some estimations in order to obtain it were necessary. As the pressure gradient is a function of the flow-rate, a wrong flow-rate in the coronary tree could led to inaccurate values of the pressure drop and thus to erroneous results in the  $FFR_{CT}$  values. The two implemented strategies have been compared and then the one in which better results in term of  $FFR_{CT}$  accuracy were achieved, was adopted.

From the available patient-specific data, the CO, has been estimated starting from an average stroke volume (**SV**) available in the literature [28] as a function of patient's age and gender, or from a SV value derived by patient's pulse pressure, age, weight and resting HR [45]. A brief description of the two implemented strategies is given below.

***Strategy1.*** In the first method coronary blood flow was calculated using the following pipeline:

- Based on patient's age and gender Left Ventricular Stroke Volume (**LVSV**) index has been extracted from the average results obtained by Kawel et al. [28]. LVSV index was calculated as  $LVSV/BSA$ , in which BSA is the Body Surface Area;
- BSA was then derived based on Du Bois formula [14]:

$$BSA = 0.007184 \cdot W^{0.425} \cdot H^{0.725} \quad (3.9)$$

in which W is the weight in kilograms and H is the height in centimeters;

- LVSV can be then derived as:

$$LVSV = LVSV_{index} \cdot BSA \quad (3.10)$$

- From the literature is known that patient's CO is related to HR and stroke volume by the given relation:

$$CO^{rest} = LVSV \cdot HR_{rest} \quad (3.11)$$

- Coronary flow at rest ( $Q_{cor}^{rest}$ ) has been then considered as 4% of CO.

**Strategy2.** The second approach instead, was implemented using the workflow adopted in Muller et al. [45] study and herein described:

- SV has been calculated starting from DeSimone formula [12] given as:

$$SV = PP^* \cdot [(0.013 \cdot W) - (0.007 \cdot Y) - (0.004 \cdot HR_{rest}) + 1.307] \quad (3.12)$$

where W is the weight in kilograms, Y the age and  $HR_{rest}$  the resting heart rate.  $PP^*$  is calculated as follows:

$$PP^* = (0.49 \cdot PP) + (0.3 \cdot Y) + 7.11 \quad (3.13)$$

where PP is the pulse pressure calculated as BSP-BDP in which BSP and BDP are respectively blood systolic and diastolic pressure in mmHg;

- CO is then computed as:

$$CO^{rest} = SV \cdot HR_{rest} \quad (3.14)$$

- Total coronary blood flow can be calculated by the given equation:

$$Q_{cor}^{rest} = \gamma \cdot CO^{rest} \quad (3.15)$$

in which  $\gamma$  is the fraction of CO that flows in the coronary arteries and in this case has been considered to be 0.045.

After the resting coronary flow has been calculated, for either the first or second strategy, the last applied steps were the same. Firstly, coronary flow was distributed between left and right coronary artery using a 6:4 proportion [6, 77]. Later, in order to replicate the vasodilation induced by adenosine administration, coronary hyperaemic flow needed to be imposed. TCRI was calculated based on patient's hyperaemic HR, using the formula introduced by Sharma et al. [59]:

$$TCRI_{corr} = \begin{cases} 0.0016 \cdot HR_{hyp} + 0.1 & \text{if } HR_{hyp} \leq 100\text{bpm} \\ 0.001 \cdot HR_{hyp} + 0.16 & \text{if } HR_{hyp} > 100\text{bpm} \end{cases} \quad (3.16)$$

Coronary hyperaemic patient-specific flow-rate was then derived as follows:

$$Q_{cor}^{hyp} = \frac{Q_{cor}^{rest}}{TCRI} \quad (3.17)$$

Finally, the hyperaemic flow-rate was distributed in the coronary branches using Murray's Law [45]. To impose proper outlet BC, the same procedure used with the average literature data to optimized the parameters of the LPM, was applied.

### 3.2.5.3. Wall BCs

An assumption that is often used in the literature is that vessel wall is approximated as rigid. A no-slip boundary condition was imposed in this study. This means that the model ignores wall compliance and the influence of cardiac-induced wall-motion but it has been shown that the incorporation of wall compliance is not so significant for simulation results [67].

### 3.2.6. CFD Simulations

CFD simulations were run in ANSYS Fluent. Both steady-state and transient simulations were performed. Instead of complete steady-state simulations, quasi-steady simulations were run. This choice was done to help reaching the imposed convergence criteria. A transient simulation was thus run imposing steady inlet and outlet BCs. In **Table 3.4** are reported in more details the parameters set before running the simulations.

SETTINGS	
Method	SIMPLE
Computational Scheme	2nd order
URF	0.8 for the pressure and 0.2 for linear momentum
Initialization	All-zones
Convergence	$10^{-5}$
Time Steps	5000
$\Delta t$	0.001 s
Max iterations per timestep	200
Saved variables	Static and Absolute pressure, Velocity

Table 3.4: Simulation settings.

After each simulation was terminated, the resulting inlet flow-rate was compared to the expected one (i.e., the one obtained as inlet coronary flow-rate calculated using the strategies described in Section 3.2.5.1 and 3.2.5.2). The relative error was calculate and an algorithm for decreasing the error below 10% was implemented. Based on the error achieved, the **Algorithm 3.1** was used to modify the resistance values.

---

**Algorithm 3.1** Resistance correction algorithm

---

- 1: **Input:**  $(R_1, \dots, R_i, \dots, R_N)_{init}, Q_{expected}$  {N = number of coronary branches}
  - 2: **Output:**  $(R_1, \dots, R_i, \dots, R_N)_{final}$
  - 3:  $n = 1$  {run first simulation}
  - 4:  $\epsilon_{r_1} \leftarrow \frac{Q_1 - Q_{expected}}{Q_{expected}}$
  - 5:  $(R_1, \dots, R_i, \dots, R_N)_2 \leftarrow (R_1, \dots, R_i, \dots, R_N)_1 * (1 - \epsilon_{r_1})$
  - 6: **while**  $\epsilon_{r_n} > 0.1$  **do**
  - 7:    $n \leftarrow n + 1$  {run the simulation with new R}
  - 8:    $\epsilon_{r_n} \leftarrow \frac{Q_n - Q_{expected}}{Q_{expected}}$
  - 9:    $(R_1, \dots, R_i, \dots, R_N)_{n+1} \leftarrow (R_1, \dots, R_i, \dots, R_N)_n * (1 - \epsilon_{r_n})$
  - 10: **end while**
  - 11:  $(R_1, \dots, R_i, \dots, R_N)_{final} \leftarrow (R_1, \dots, R_i, \dots, R_N)_n$
-

### 3.2.7. Post-Processing

The obtained pressure and velocity fields were imported in Paraview for the post-processing. For the steady simulation, the last time-step was analysed whether for the transient one, the last cardiac cycle was imported in Paraview and the *Temporal Statistic* filter was used to obtain the average values of the variables of interest. In both the simulations the  $FFR_{CT}$  value was obtained by dividing the pressure field in all the points by the inlet pressure. The results of the simulations run imposing patient-specific BCs were compared against the available invasive measurements reported in **Table 3.1**. The binary agreement between iFFR and  $FFR_{CT}$  based on a cut off of 0.80 was also analysed. The agreement is equal to 1 if both  $\leq 0.80$  or  $> 0.80$ , 0 otherwise. The difference between steady and transient  $FFR_{CT}$  was also examined, for both the set of simulations, point by point, to validate the initial hypothesis of the feasibility of using a steady simulation instead of a transient one saving time and computational power.

# 4 | Results

This Section will present the results obtained from the numerical simulations in both the idealized and patient-specific geometry. The first part will focus on the idealized geometry with varying degrees of stenosis, the second one will cover the results obtained from patient-specific simulations for both sets of BCs.

Special attention will be paid to the comparison between the estimated FFR resulting from steady-state and transient simulations. In the post-processing of the CFD simulations, fluid dynamics variables such as pressure (**Appendix B**), FFR, flow rate, and vorticity were analyzed. The estimated FFR was validated against invasively measured FFR in the patient-specific geometries CFD simulations with BCs obtained from patient-specific data.

## 4.1. Idealized Geometry

A map of FFR for pipes with degrees of stenosis ranging from 50% to 80% is presented in **Figure 4.1** for both steady-state and transient simulations. Pressure contour maps and velocity field for the different geometries can be consulted in **Appendix B**. Inlet and outlet BC as well as the flow-rate for each of the levels of disease are reported respectively in **Table 4.1** and **Table 4.2**.

For increasing degrees of stenosis the Steady FFR ( $\mathbf{FFR}_{SS}$ ) becomes significantly lower if compared to Transient FFR ( $\mathbf{FFR}_T$ ). This means a greater pressure drop is present in the steady-state simulations. The relative difference between the FFR computed, sharply increases as the stenosis degree becomes greater (difference is  $\sim 26\%$  for a 70% stenosis). Consistently with this result, in the transient simulations a greater decrease in flow-rate is present.

To further investigate this difference, vorticity was derived from the extracted velocity field. Vorticity is a pseudo-vector field that represents the tendency of an infinitesimal volume of a continuum to rotate with respect to a local observator that moves as the flow.

	Steady	Transient
Inlet BC	$P = 90$	Pressure Waveform $P_{mean} = 90$
Outlet BC	$R_{tot} = 2.63 \cdot 10^9$	$R1 = 7.55 \cdot 10^8$ $R2 = 1.85 \cdot 10^9$ $C = 9.07 \cdot 10^{-5}$

Table 4.1: Boundary conditions imposed at the inlet and outlet surface of the idealized geometry. Pressure, resistance and compliance are respectively in  $mmHg$ ,  $Pa \cdot s/m^3$  and  $m^3/Pa$ .

% Stenosis	Q-Steady $\times 10^{-6}$	Q-Transient $\times 10^{-6}$
50%	3.74	3.86
60%	3.17	3.09
70%	2.29	1.62
75%	1.77	1.21
80%	1.22	0.85

Table 4.2: Inlet flow-rate resulting from the steady-state and transient simulations. Q-Transient is the average value calculated over the last cycle. The reported values are in  $m^3/s$ .

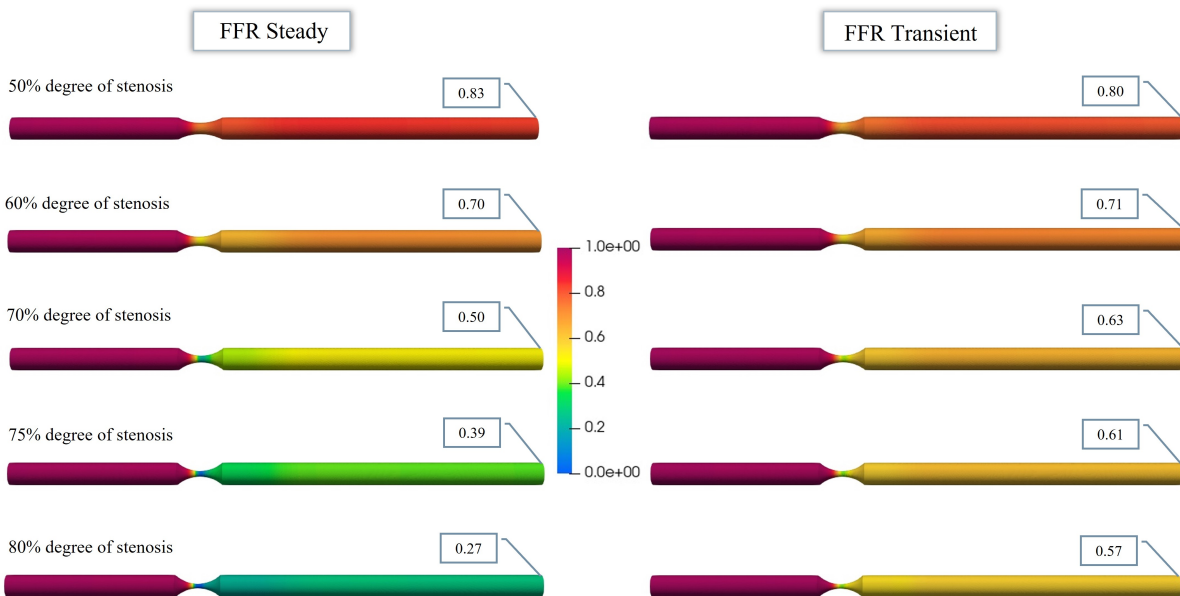


Figure 4.1: Comparison between the FFR maps generated by steady and transient simulations, for progressively increasing degrees of stenosis.



It is defined as the curl of the flow velocity (**Equation 4.1**).

$$\vec{\omega} = \nabla \times \vec{u} \quad (4.1)$$

The variable was plotted on the velocity streamlines. Its maximum values were found in each case at throat section of the stenosis. A plot of the vorticity field on such section and on flow streamlines are illustrated in **Figure 4.2**. The data suggests a relationship between vorticity and the highest pressure gradient identified in the steady simulations. Furthermore, as the obstruction level rises, the difference between vorticity measurements in steady-state and transient simulations increases as well. Specifically, the vorticity values in the steady-state simulations are notably higher. The highest value of vorticity for both steady and transient simulations is reported in **Table 4.3**.

% Stenosis	MaxVorticity-Steady $\times 10^4$	MaxVorticity-Transient $\times 10^4$
50%	2.12	2.58
60%	4.22	4.21
70%	5.75	4.81
75%	6.66	5.11
80%	7.92	5.57

**Table 4.3:** Highest value of vorticity found in the cross-sectional plane positioned at the center of the stenosis.

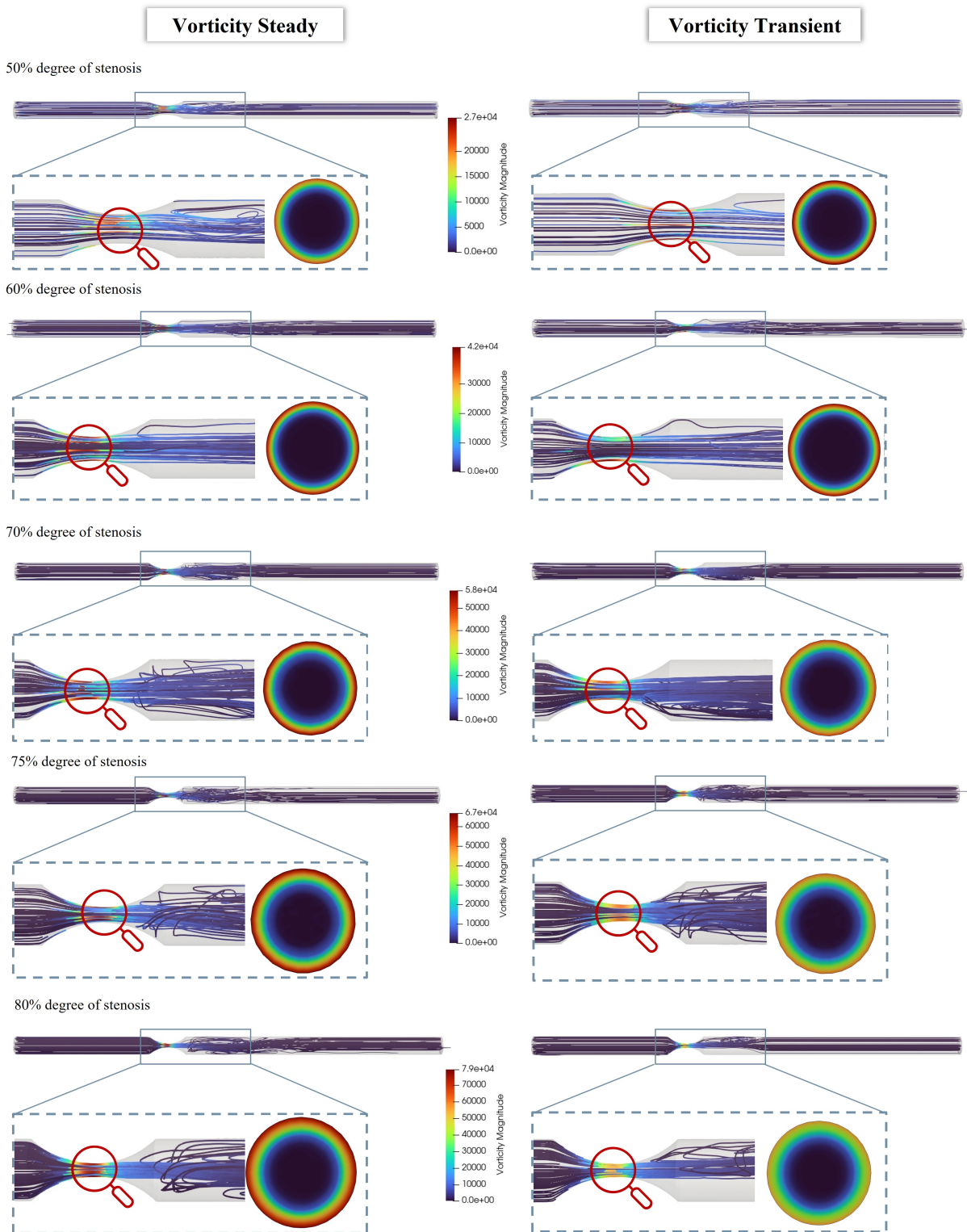


Figure 4.2: Comparison of vorticity (steady-state vs transient simulation) for the different levels of disease. The figure displays streamlines and highlights vorticity values in a cross-sectional plane located within the stenosis region.

## 4.2. Patient-Specific Geometry

The reconstructed coronary artery geometry of the four analysed patients was simulated with both sets of BCs explained in the Materials and Methods' Section.

### 4.2.1. Sensitivity Analysis

Mesh sensitivity results, performed as described in Section 3.2.3, are herein reported. The grid convergence index (**GCI**) selected for the three analyzed meshes (coarse = 1, medium = 2, fine = 3) was the ratio between the pressure in the stenosis region and the inlet pressure. The values obtained for the GCI were  $f1 = 0.886$ ,  $f2 = 0.869$ , and  $f3 = 0.862$ . **Figure 4.3** illustrates the relationship between the considered function and the number of mesh elements. The relative difference between the coarser and medium mesh was found to be  $\sim 2\%$ , whereas between medium and finer mesh, was less than 1%. Based on this findings, the medium mesh, comprising around 15 million tetrahedral elements and a maximum element size of 0.1 mm, was selected. The mesh quality metric parameters for the selected mesh, such as aspect ratio, orthogonal quality, and skewness, are displayed in **Figure 4.4**.

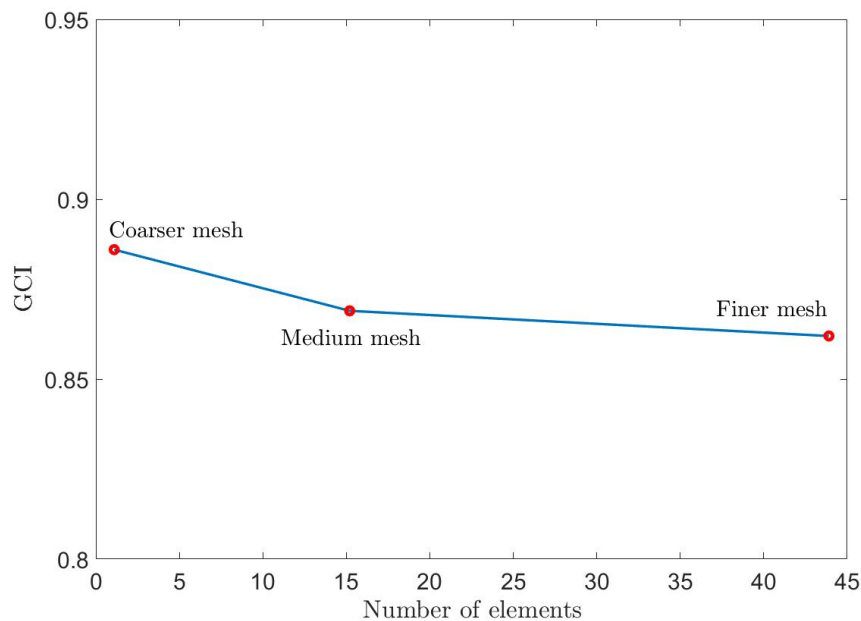


Figure 4.3: Sensitivity mesh analysis results.

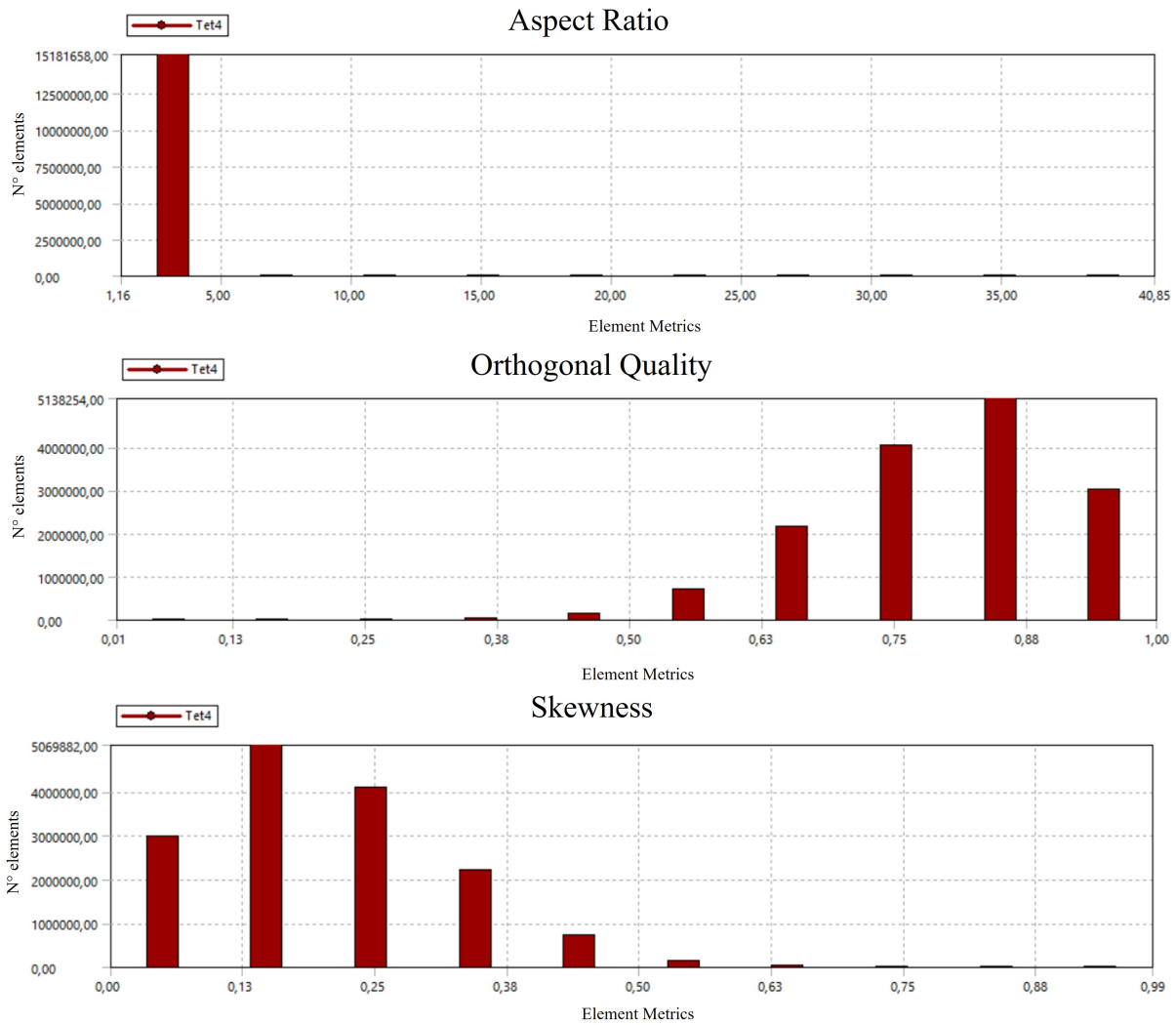


Figure 4.4: The mesh used had an element size of 0.1 mm, and an analysis of the element metrics was conducted. The metrics evaluated were Aspect Ratio, Orthogonal Quality, and Skewness, with the results displayed in a top-to-bottom order. A good mesh quality was indicated by an aspect ratio of approximately 3, an orthogonal quality near 1, and a skewness close to 0.

### 4.2.2. Patient-Specific Geometry with BCs Estimated from Average Population Data

In order to evaluate the feasibility of using a steady-state simulation rather than a transient one,  $FFR_{SS}$  and  $FFR_T$  are herein compared. **Table 4.4** to **Table 4.7** present the LPM values obtained after their optimization and thus used as BCs for running the simulations. Specifically  $R_{tot}$  is the resistance BC imposed in the steady simulations while  $R_1$ ,  $R_2$  and  $C$  are the parameters of the 3WK imposed as outlet BC for the transient simulations.

**Table 4.8** presents the applied pressure at the inlet section, expected (based on literature flow-rate values reported in Section 3.2.5.1) and resulted inlet flow-rate. LPM was tuned in such a way that a difference between expected and obtained flow-rate was  $\leq 10\%$ .

The hemodynamic difference between steady-state and transient results in terms of  $FFR_{CT}$  was first examined. The CFD-derived FFR for the four different geometries is illustrated in **Figure 4.5**. The shown  $FFR_{CT}$  value was taken  $\sim 30$  mm distally to the stenosis region. **Table 4.9** summarizes the results of computation and their relative difference, that was given by:

$$\epsilon_r = \frac{FFR_{SS} - FFR_T}{FFR_T} \quad (4.2)$$

The maximum difference between the two obtained  $FFR_{CT}$  was found to be lower than 1% in all the four analysed geometries. The current findings contradict the results obtained from simulations of the idealized geometry. Specifically, no significant differences were observed between the  $FFR_{CT}$  values obtained from steady and transient simulations, even for more severe degrees of stenosis (i.e. Patient-6).

In the postprocessing of the CFD simulations, vorticity was derived from the velocity field and analysed, as in the idealized geometry scenario. The vorticity streamlines obtained from both steady and transient simulations are presented in **Figure 4.6**, with vorticity examined on a cross-sectional plane in the stenosis region. In contrast to the idealized geometry case, no significant difference in vorticity was noticed (maximum difference of  $\sim 6\%$  in patient-10). **Table 4.10** reports the highest vorticity value found in the stenosis region for all four patients analyzed.

PATIENT 1	Outlet1	Outlet2	Outlet3	Outlet4	Outlet5	Outlet6	Outlet7
$R1 \times 10^{10}$	0.43	0.21	0.28	0.30	0.61	0.35	0.09
$R2 \times 10^{10}$	1.00	0.49	0.65	0.69	1.42	0.82	0.22
$R_{tot} \times 10^{10}$	1.43	0.71	0.93	0.99	2.03	1.17	0.31
$C \times 10^{-11}$	2.08	7.22	5.31	2.08	2.08	2.34	4.40

Table 4.4: Optimized resistance and compliance values for Patient-1, using BCs based on average-population data. The values are reported for each outlet branch. Resistances and compliance are respectively in  $Pa \cdot s/m^3$  and  $m^3/Pa$ .

PATIENT 6	Outlet1	Outlet2	Outlet3	Outlet4	Outlet5	Outlet6	Outlet7	Outlet8
$R1 \times 10^{10}$	1.76	0.23	0.25	0.20	1.42	0.13	0.44	0.26
$R2 \times 10^{10}$	4.12	0.53	0.59	0.47	3.31	0.27	1.03	0.60
$R_{tot} \times 10^{10}$	5.88	0.76	0.84	0.67	4.73	0.38	1.47	0.86
$C \times 10^{-11}$	1.67	3.76	2.01	4.06	1.67	1.31	3.27	7.35

Table 4.5: Optimized resistance and compliance values for Patient-6, using BCs based on average-population data. The values are reported for each outlet branch. Resistances and compliance are respectively in  $Pa \cdot s/m^3$  and  $m^3/Pa$ .

PATIENT 9	Outlet1	Outlet2	Outlet3	Outlet4	Outlet5	Outlet6
$R1 \times 10^{10}$	0.80	0.19	0.77	0.13	0.21	0.40
$R2 \times 10^{10}$	1.86	0.45	1.80	0.31	0.49	0.92
$R_{tot} \times 10^{10}$	2.66	0.64	2.57	0.44	0.70	1.32
$C \times 10^{-11}$	3.12	1.00	4.18	1.11	4.67	3.85

Table 4.6: Optimized resistance and compliance values for Patient-9, using BCs based on average-population data. The values are reported for each outlet branch. Resistances and compliance are respectively in  $Pa \cdot s/m^3$  and  $m^3/Pa$ .

PATIENT 10	Outlet1	Outlet2	Outlet3	Outlet4	Outlet5	Outlet6	Outlet7	Outlet8
$R1 \times 10^{10}$	0.65	0.66	0.29	0.99	0.80	0.15	0.49	0.11
$R2 \times 10^{10}$	1.51	1.53	0.67	2.31	1.86	0.36	1.14	0.25
$R_{tot} \times 10^{10}$	2.15	2.19	0.96	3.30	2.65	0.51	1.63	0.36
$C \times 10^{-11}$	2.56	1.64	2.07	1.84	1.56	5.70	3.09	6.54

Table 4.7: Optimized resistance and compliance values for Patient-10, using BCs based on average-population data. The values are reported for each outlet branch. Resistances and compliance are respectively in  $Pa \cdot s/m^3$  and  $m^3/Pa$ .

	Pressure-Steady	Pressure-Transient	Q <sub>expected</sub> $\times 10^{-6}$	Q- <sub>Steady</sub> $\times 10^{-6}$	Q- <sub>Transient</sub> $\times 10^{-6}$
Patient-1	100	120/80	10.00	9.71	9.81
Patient-6	100	120/80	6.67	5.96	5.91
Patient-9	100	120/80	6.67	6.00	6.06
Patient-10	100	120/80	10.00	9.92	10.10

Table 4.8: Inlet pressure and flow-rate for both the steady-state and transient simulations. Pressure is in *mmHg* while flow-rate is in  $m^3/s$ .



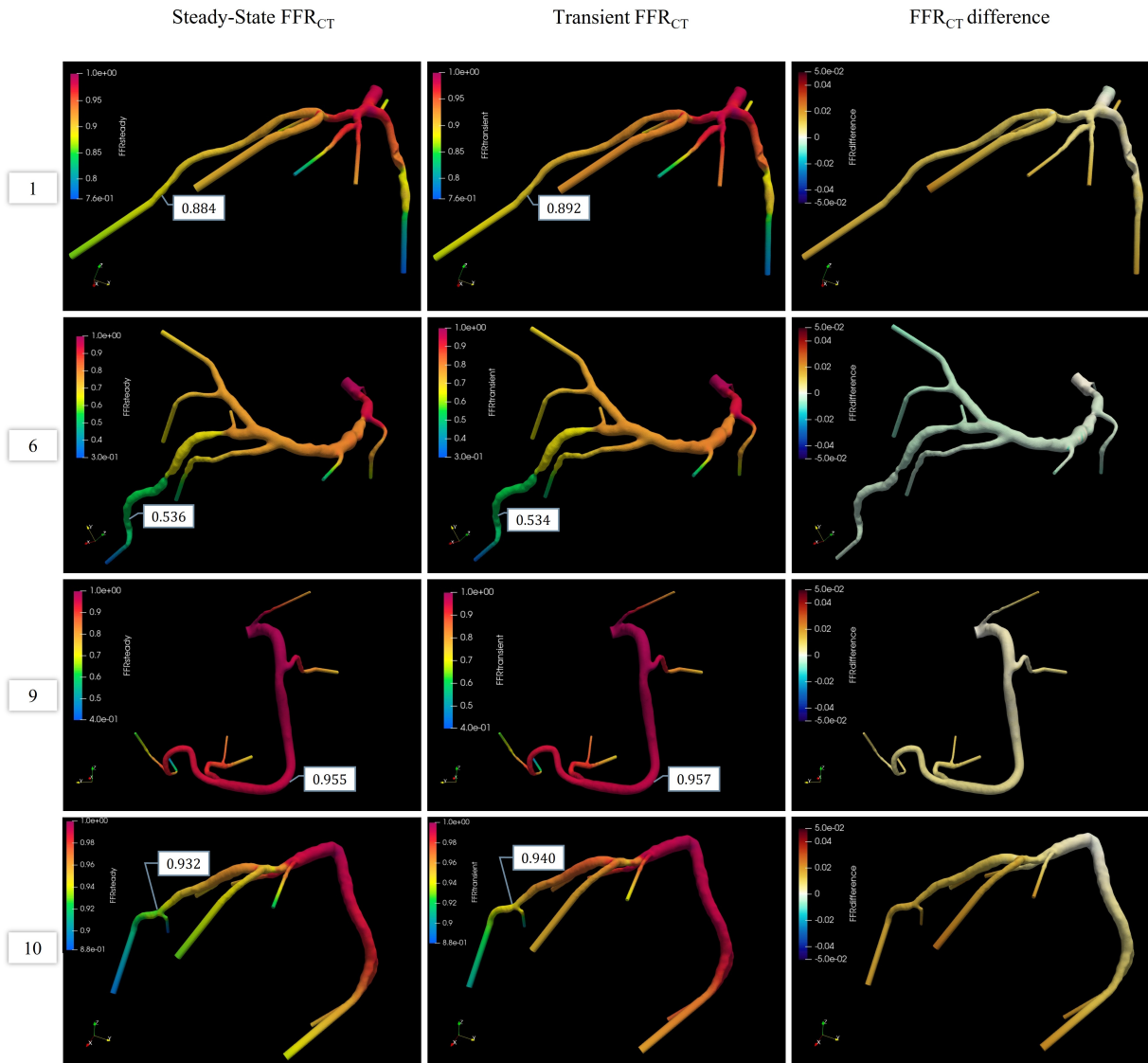


Figure 4.5: Comparison between  $FFR_{CT}$  maps obtained from steady-state and transient simulation. The relative difference between the two is illustrated in the last column.

	FFR-Steady	FFR-Transient	FFR- $\epsilon_r$
Patient-1	0.884	0.892	0.89%
Patient-6	0.536	0.534	0.37%
Patient-9	0.955	0.957	0.21%
Patient-10	0.932	0.940	0.85%

Table 4.9: Comparison between the  $FFR_{CT}$  values obtained from steady-state and transient simulations, with the relative error between the two displayed in the last column.

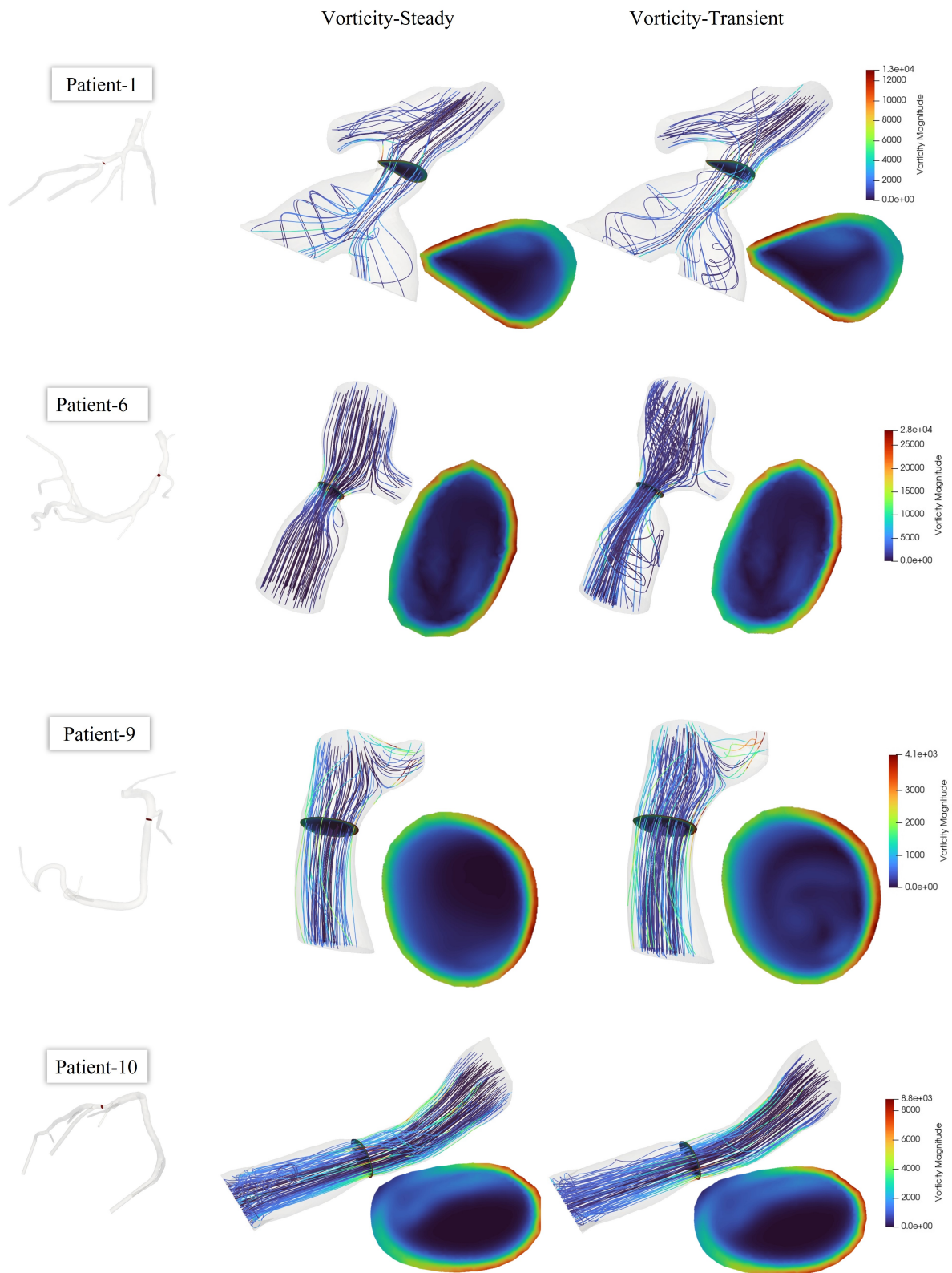


Figure 4.6: Comparison between vorticity generated by steady-state and transient simulations. Particular attention is given to the highest value detected in the cross-sectional plane located at the stenosis center.

PATIENT	MaxVorticity-Steady $\times 10^4$	MaxVorticity-Transient $\times 10^4$
1	1.27	1.3
6	2.81	2.75
9	0.41	0.41
10	0.88	0.83

Table 4.10: Highest value of vorticity found in the cross-sectional plane positioned at the center of the stenosis (Patient-specific geometry with BCs based on average population data).

### 4.2.3. Patient-Specific Geometry with BCs based on Patient-Specific Data

Finally, the proposed method was validated by comparing the obtained  $FFR_{CT}$  value against the invasively measured FFR. As mentioned in Section 3.2.5.2, two different strategies were investigated to estimate the inlet coronary flow-rate. In **Figure 4.7** the results obtained by the two strategies for Patient-6 are illustrated. The difference in the computed  $FFR_{CT}$  resulted to be  $\sim 15\%$ . Flow-rate values for the first and second method were respectively  $5.23 \cdot 10^{-6} m^3/s$  and  $6.08 \cdot 10^{-6} m^3/s$ . Based on the  $FFR_{CT}$  diagnostic performance, the second strategy for the estimation of the inlet flow rate was adopted.

In **Table 4.11** the pressure and inlet flow-rate are reported. Also with this set of simulations, a difference in inlet-flow rate  $\leq 10\%$  was accepted (see Section 3.2.6). The resistance and capacitance values obtained after the tuning and used as outlet BC for the four geometries are summarized in **Tables 4.12 to 4.15**. The main focus with these simulations was the validation of the method: for this purpose both steady and transient simulations derived FFR were compared against iFFR.  $FFR_{CT}$  maps for the four patients are illustrated in **Figure 4.8**. **Table 4.16** summarises the obtained results and the relative difference with respect to the iFFR, calculated as follows:

$$\epsilon_r = \frac{FFR_{CT} - iFFR}{iFFR} \quad (4.3)$$

A good agreement was found for Patient-6 and -9 ( $\epsilon_r \leq 6.5\%$ ), patients with respectively the higher and lower degree of stenosis. iFFR was significantly lower when compared to  $FFR_{CT}$  in Patient-1 ( $\sim 10\%$ ) and -6 ( $\sim 20\%$ ). Considering the agreement based on the standard revascularization threshold of 0.80, the FFR of three over four patients is in

agreement with the invasive measurement.

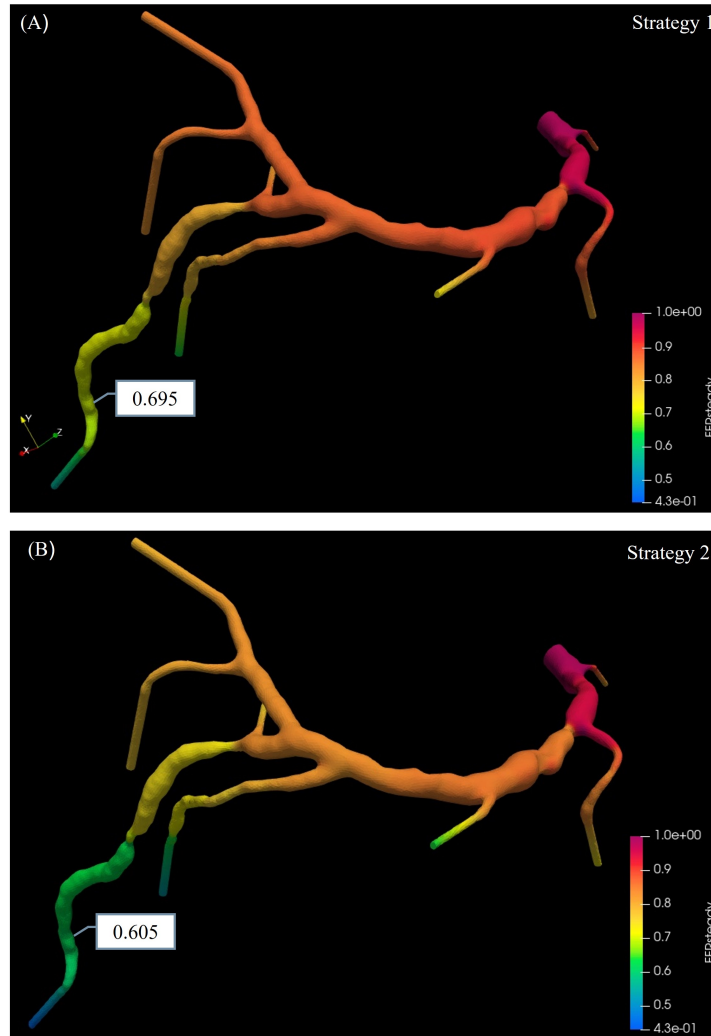


Figure 4.7: Comparison between the  $FFR_{CT}$  map obtained using the first (A) and the second approach (B) for estimating inlet coronary flow-rate.

	Pressure-Steady	Pressure-Transient	$Q_{\text{expected}}$ $\times 10^{-6}$	$Q_{\text{steady}}$ $\times 10^{-6}$	$Q_{\text{transient}}$ $\times 10^{-6}$
Patient-1	106.25	132/85	8.95	8.71	9.01
Patient-6	118.55	160/85	6.08	5.80	5.81
Patient-9	94.55	135/65	6.41	5.80	6.16
Patient-10	100.81	130/80	12.30	11.30	11.90

Table 4.11: Inlet pressure and flow-rate for both steady-state and transient simulations.

PATIENT 1	Outlet1	Outlet2	Outlet3	Outlet4	Outlet5	Outlet6	Outlet7
$R1 \times 10^{10}$	0.53	0.26	0.35	0.37	0.75	0.43	0.11
$R2 \times 10^{10}$	1.23	0.61	0.81	0.85	1.75	1.01	0.27
$R_{tot} \times 10^{10}$	1.76	0.87	1.15	1.22	2.50	1.44	0.38
$C \times 10^{-11}$	2.06	7.14	5.25	2.06	2.06	2.33	4.43

Table 4.12: Optimized resistance and compliance values for Patient-1, using BCs based on patient-specific data. The values are reported for each outlet branch. Resistances and compliance are respectively in  $Pa \cdot s/m^3$  and  $m^3/Pa$ .

PATIENT 6	Outlet1	Outlet2	Outlet3	Outlet4	Outlet5	Outlet6	Outlet7	Outlet8
$R1 \times 10^{10}$	0.77	0.39	0.48	0.23	0.97	0.19	0.80	0.49
$R2 \times 10^{10}$	1.80	0.91	1.12	0.53	2.26	0.45	1.88	1.16
$R_{tot} \times 10^{10}$	2.57	1.30	1.60	0.75	3.23	0.64	2.68	1.65
$C \times 10^{-11}$	1.63	3.67	1.96	3.96	1.63	1.28	3.20	7.18

Table 4.13: Optimized resistance and compliance values for Patient-6, using BCs based on patient-specific data. The values are reported for each outlet branch. Resistances and compliance are respectively in  $Pa \cdot s/m^3$  and  $m^3/Pa$ .

PATIENT 9	Outlet1	Outlet2	Outlet3	Outlet4	Outlet5	Outlet6
$R1 \times 10^{10}$	0.77	0.23	0.67	0.12	0.19	0.36
$R2 \times 10^{10}$	1.79	0.53	1.63	0.28	0.44	0.83
$R_{tot} \times 10^{10}$	2.55	0.76	2.33	0.40	0.63	1.19
$C \times 10^{-11}$	3.21	1.02	4.30	1.15	4.80	3.97

Table 4.14: Optimized resistance and compliance values for Patient-9, using BCs based on patient-specific data. The values are reported for each outlet branch. Resistances and compliance are respectively in  $Pa \cdot s/m^3$  and  $m^3/Pa$ .

PATIENT 10	Outlet1	Outlet2	Outlet3	Outlet4	Outlet5	Outlet6	Outlet7	Outlet8
$R1 \times 10^{10}$	0.56	0.57	0.25	0.86	0.69	0.13	0.42	0.09
$R2 \times 10^{10}$	1.32	1.34	0.58	2.01	1.61	0.31	0.99	0.22
$R_{tot} \times 10^{10}$	1.88	1.91	0.83	2.87	2.30	0.44	1.42	0.31
$C \times 10^{-11}$	2.57	1.64	2.07	1.85	1.56	5.71	3.10	6.56

Table 4.15: Optimized resistance and compliance values for Patient-10, using BCs based on patient-specific data. The values are reported for each outlet branch. Resistances and compliance are respectively in  $Pa \cdot s/m^3$  and  $m^3/Pa$ .

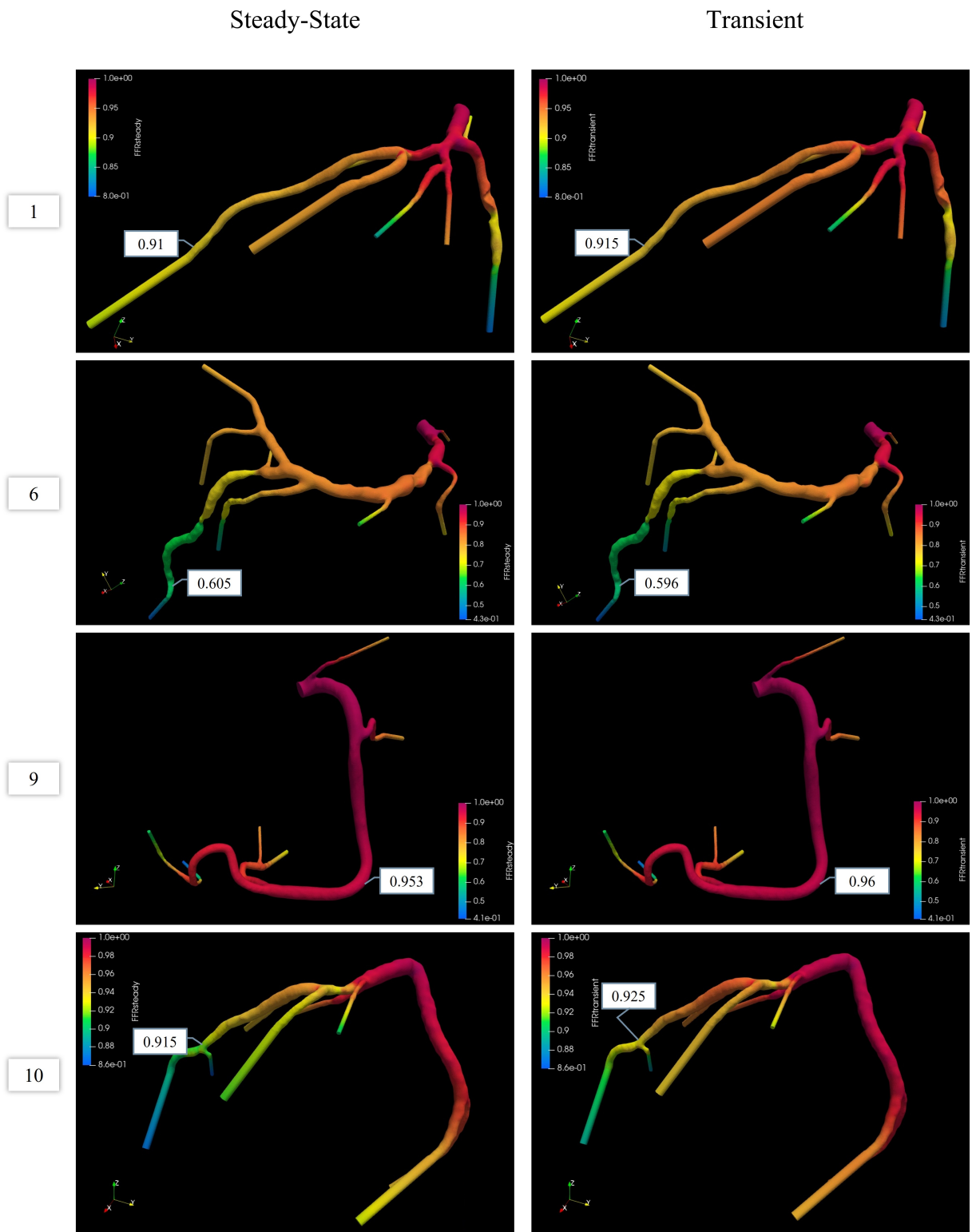


Figure 4.8: CFD-derived FFR for both steady-state and transient simulations run using patient-specific BCs.

	iFFR	$FFR_{SS}$	$FFR_T$	$\epsilon_r$ ( $FFR_{SS}-FFR_T$ )	$\epsilon_r$ ( $FFR_{SS}-iFFR$ )	$\epsilon_r$ ( $FFR_T-iFFR$ )	Agreement
Patient-1	0.76	0.91	0.915	0.55%	19.73%	20.39%	0
Patient-6	0.57	0.605	0.596	1.50%	6.10%	4.56%	1
Patient-9	0.94	0.953	0.96	0.73%	1.38%	2.12%	1
Patient-10	0.83	0.915	0.92	0.55%	10.24%	10.84%	1

Table 4.16: Comparison of the obtained  $FFR_{CT}$  from steady-state and transient simulations against the iFFR. The highlighted columns indicate the relative difference, important to validate the model, while the last column displays the agreement between  $FFR_{CT}$  and iFFR.



## 5 | Discussion

CAD is the leading cause of death globally, primarily caused by the built-up of a plaque that narrows the vessel lumen. This pathology is known as atherosclerosis and results in an inadequate supply of blood and oxygen to the myocardium. Possible consequences can include myocardial infarction and sudden cardiac death. Early diagnosis and adequate treatment of CAD in high-risk patients can prevent premature deaths. To date ICA is considered as the gold standard for the evaluation of coronary artery lumen, even though in the last years CCTA has emerged as a non-invasive, less-expensive, robust and reliable technique. According to consensus guidelines, FFR is the hemodynamic index clinically used to evaluate the hemodynamic importance of a coronary stenosis. It is invasively measured by inserting a pressure wire in the vessel lumen and it tells to what extent blood flow in a coronary artery is limited due to CAD. FFR less or equal to 0.80 is commonly considered the threshold for coronary revascularization. FFR is currently utilized in fewer than 10% of CAD assessments because of its measurement invasiveness. Advancements in clinical images, mathematical models and computational power have led to the emergence of a new diagnostic tool: the  $FFR_{CT}$ . It combines imaging information and CFD simulations to non-invasively assess the functional severity of a stenosis. It could be used as a first step in the screening, diagnosis, decision-making and treatment planning of CAD. The development of different computational techniques has received great attention and nowadays different models, from simpler to more complex ones, have been proposed. The analysis of the literature revealed promising outcomes, showing comparable results in terms of  $FFR_{CT}$  with respect to the iFFR. A simple and fast CFD model is desirable for introducing  $FFR_{CT}$  analysis into clinical practice.

Accordingly, the present thesis work aimed to develop a CFD pipeline for non-invasively estimating  $FFR_{CT}$ . Two types of geometries were investigated: idealized (i.e. pipe with varying degrees of stenosis) and patient-specific. The focus was on study the effectiveness of using steady-state simulations to reduce computational costs and time. To the best of the author's knowledge, only a few studies [36, 38] have compared results obtained from steady-state and transient simulations and further analysis is desirable. Patient-specific geometries were examined using two different sets of BCs: population-average and patient-

specific. To validate the accuracy of the proposed model, the results of patient-specific simulations with patient-specific BCs, were compared with the invasively measured FFR. In all the analysed models, a pressure at the inlet and a LPM at the outlets were imposed as BCs.

Firstly, an idealized geometry with varying degrees of stenosis, ranging from 50% to 80% was simulated. The obtained results showed that both steady-state and transient simulation revealed a reduction in FFR as the percentage of stenosis increases, as expected. The increase in pressure drop can be explained by the higher resistance to flow caused by vessel narrowing, resulting in both distributed losses along the length of the pipe (as described by Poiseuille's Law in laminar flow) and concentrated losses in the narrowing region. The studies conducted by [33, 57, 65] obtained comparable pressure maps for the analysed degree of stenosis. However, none of these studies compared steady-state and transient simulations. When comparing steady and transient simulation results, it can be seen that for 50-60% degree of stenosis the  $FFR_{SS} \sim FFR_T$ , while for more severe narrowings (i.e.  $> 70\%$ ),  $FFR_{SS}$  tends to overestimate the severity of the stenosis, when compared with  $FFR_T$  (**Figure 4.1**). This significant difference may be due to the fact that swirling structures tend to form in the velocity field downstream the narrowing and, while in the transient case they tend to be dissipated, they persist in the steady scenario. Thus, to better understand this phenomenon, an additional analysis on vorticity was performed. Vorticity was observed to increase as pressure drop increased for both steady and transient simulations. Furthermore it resulted significantly and increasingly higher in steady simulations with respect to transient ones as the stenosis degree increased (**Table 4.3**). Specifically, a lower FFR corresponds to a higher vorticity value in the stenosis region. The reason for this can be attributed to the fact that high vorticity is associated with high shear stress in boundary regions, leading to greater resistance to flow [26] and in turn, a higher pressure drop.

$FFR_{CT}$  was then evaluated in patient-specific geometries. To focus only on the impact of the geometry, all of the patients in the pool were simulated with the same BCs estimated from average literature data. The obtained results showed that, contrary to what happened in the idealized geometry, there is no significant difference between  $FFR_{CT}$  estimated from steady-state and transient simulations. The relative difference between the two simulation approaches was found to be less than 1% (**Table 4.9**) indicating that the hemodynamic distribution computed by  $FFR_{SS}$  is essentially identical to that of  $FFR_T$ . Based on these findings and the fact that FFR is clinically determined as the time-average ratio of distal over proximal pressure, it can be concluded that steady-state simulations can be exploited to assess the severity of a stenosis from a hemodynamic point of view,

with the same accuracy that can be obtained using a transient simulation. Comparable results were reported by Lo et al. [38] and Liu et al. [35] through their examination of steady-state and transient simulations. More specifically [38] obtained a maximum discrepancy of 2% while [36] observed a maximum relative error of 6.7%. However, Liu et al. investigated a larger sample size of patients, analysing 154 vessels, which may account for the slightly higher results. Conversely, other groups [37, 45, 63, 64] exclusively employed steady-state simulations and compared the outcomes with iFFR, resulting in an accuracy level of approximately 90%. The high agreement observed between  $FFR_{CT}$  values (i.e., steady and transient) suggests that utilizing a simpler yet efficient simulation approach may be acceptable. Steady simulations are simpler to execute, require fewer parameters and less computational cost.

From the analysis of the vorticity, consistently with  $FFR_{CT}$  results, no significant difference in the highest values obtained in the stenosis region between steady-state and transient simulations was observed (**Table 4.10**). Vorticity resulted higher in the idealized geometry simulations compared to patient-specific geometry ones. This could be attributed to the fact that this geometry had a smaller diameter at the stenosis centre, resulting in higher shear stress and therefore, higher vorticity. Furthermore, the curvature of the vessel may dump the vortical structures that form due to the stenosis that consequently would dissipate sooner. The vorticity resulting from steady-state and transient simulations remains comparable in the pipe for less significant degrees of stenosis (i.e. higher diameter in stenosis region). The patient with the most severe coronary obstruction (e.g. Patient-6) exhibits vorticity values similar to those observed in the idealized geometry with a 50% lesion.

Finally, the proposed approach for the evaluation of  $FFR_{CT}$  was validated in relation to iFFR. Among the two analysed strategies to determine patient-specific coronary flow-rate (Section 3.2.5.2), the second method was employed for all four patients, as it resulted in improved FFR diagnostic performance and incorporated more physiological parameters of the patient. The two strategies produced distinct inlet flow-rate values ( $\sim 14\%$  difference), and the findings indicate how this disparity can result in inaccurate  $FFR_{CT}$  values. The observed variability indicates the need for more precise estimation of patient-specific flow-rate to achieve reliable and accurate  $FFR_{CT}$  results. Since resting coronary flow-rate is mainly determined by myocardial demand, starting from LVM may be a feasible approach to estimate it. More accurate estimation of the coronary flow can be achieved with emerging approaches, such as directly calculating hyperaemic coronary flow using CTP [76].

When examining the results in terms of  $FFR_{CT}$ , both steady-state and transient simula-

tions were conducted, and their outcomes were comparable (**Table 4.16**). The proposed computational approach demonstrated relatively robust performance for Patient-6 and -9, whose RCA was analysed. A good agreement (error  $\leq 6.5\%$ ) with the iFFR was observed. However, Patient-1 and -10, whose stenotic vessel was in the LAD, exhibited greater errors.  $FFR_{CT}$  estimated for Patient-10 resulted in a 10% error. This discrepancy may be due to the fact that the imposed BCs could not be perfectly tuned to real patient parameters. Furthermore during the invasive procedure a pressure wire is inserted in the coronary vessel to achieve the measurement and this introduce an additional pressure drop that was neglected in the CFD simulations carried out in the present study.

The relatively higher  $FFR_{CT}$  compared to iFFR in patients who underwent LAD revascularization, may have various potential explanations to be considered. As previously mentioned, the inlet coronary flow-rate had to be estimated from the available patient-specific data. However, other, more accurate, methods should be further explored to obtain more reliable patient-specific values. A possible supposition could be related to the imposed BCs. In this study, a 3WK model was utilized to enforce outlet boundary conditions, which may fail to fully catch the coronary flow characteristic at the level of the microcirculation. Many researchers have exploited a more complex RCRCR model, while few used a 2WK model [38]. The employed 3WK did not account for intramyocardial pressure which is taken into account in the RCRCR and 2WK models. Thus, the pressure exerted by the ventricle on the coronary wall was not taken into account. As suggested by the literature, this contribution affects the LCA more than the RCA, as the pressure exerted by the ventricle is lower in the RCA. While the potential contribution of intramyocardial pressure remains uncertain, further investigations are necessary. Another possible consideration could be done examining the coronary geometry of the two patients. Errors may have been introduced during the segmentation and 3D anatomical reconstruction process as no inter-operator cross-validation was performed. CT-based  $FFR_{CT}$  calculations are very sensitive to image quality and segmentation accuracy. More in details, considering the stenosis region, there is no sudden decrease in diameter and the lower diameter was found to be approximately 2.5-3 mm for both geometries. Previous work by Sankaran et al [57] has shown that the minimum lumen diameter has the highest impact on  $FFR_{CT}$  uncertainty, with a greater effect in the LAD compared to the RCA where the uncertainty is generally small. Another study by Tajeddini and colleagues [62] also found a relationship between MLD and FFR, with FFR dropping below the 0.80 threshold for MLD lower than 1.5 mm.

While these presented are some possible explanations for the discrepancies obtained in some of the simulations, further investigations should be conducted.

*Limitations and Future Developments*

The CFD model that was developed to estimate the  $FFR_{CT}$  is subject to certain limitations and approximations, which serve as a foundation for future development. The main aspects that need to be improved are:

- Patient pool: the present study only analysed four patients, specifically focusing on the LAD and RCA. To fully establish a non-invasive and simple diagnostic tool for  $FFR_{CT}$  estimation, future research should expand the patient pool to include a wider range of patients, including also those with coronary lesions in the LCX;
- Coronary flow-rate: the two strategies used to estimate coronary flow-rate in this study led to highly variable results, indicating a need for further investigation into additional methods. Given the significant impact of flow-rate on the resulting  $FFR_{CT}$ , it is important to explore alternative ways for both estimating flow subdivision between LM and RCA, and flow partition in coronary branches. A possible direction for future development could be exploring other used techniques such as TAG or PET, in addition to Murray's Law. Additionally, this study allowed for a relative error ( $\leq 10\%$ ) to exist between the expected and actual inlet flow-rate. It is recommended that future research focuses on improving this aspect;
- Boundary Conditions: in the literature simple models (2WK) with fewer assumptions, but with limitations, especially when trying to capture phenomena at high frequencies, are available as well as more complex models (RCRCR) that require more complex tuning. We have tested a 3WK as it allows us to have a more accurate description than a 2WK, by introducing fewer approximations. However, some aspects that the RCRCR captures and the WK does not may be crucial. Future research could investigate the impact of the intramyocardial pressure on  $FFR_{CT}$  and improve the determination and optimization of patient-specific physiological parameters of the reduced-order model by using morphometric studies. Additionally, it would be beneficial to explore the difference between setting venous pressure to 0 or 5 mmHg;
- Hemodynamic indexes: while  $FFR_{CT}$  was the only hemodynamic index studied, other parameters as iFR, CFR, QFR, and WSS could be taken into account. It would be worthwhile to identify the optimal combination of these parameters for the identification of critical lesions;
- Viscosity: the analysis in this study used a constant viscosity for all patients. To investigate the impact, it would be useful to explore the effect of employing a patient-

specific viscosity calculated from their haematocrit levels;

- Hyperaemic conditions: in this work, a TCRI based on patient's specific hyperaemic HR [59] was utilized. However, it would be beneficial to further explore the impact of this index as it has been shown to significantly influence  $FFR_{CT}$  [76, 77];
- iFFR location: the exact location where iFFR was measured was not specified, which is an important factor to consider when comparing estimated  $FFR_{CT}$  with iFFR. The values should be taken in the same location;
- Computational cost: steady-state simulations require less time and parameters than a transient one. It may be worth exploring also the use of a 1D-0D model to further decrease the computational cost. Another method that could be investigated to improve the computational speed is the use of an automatic deep learning algorithm for image segmentation and prediction of coronary flow.

## 6 | Conclusions

Rapid development of CFD simulations and imaging technologies has led to encouraging results in combining these two fields for clinical diagnosis. In particular, the use of coronary CCTA to provide  $FFR_{CT}$  as a physiological parameter to non-invasively assess the hemodynamic significance of a coronary stenosis, is a promising application. Patient-specific coronary simulations can be challenging due to the complexity of coronary circulation and the need for accurate geometry and BCs, but the potential benefits of using this new tool in clinical practice are significant. It can provide clinicians with more precise and personalized information and can help make more informed decisions about treatment options thus increasing patients outcomes.

The proposed CFD model has demonstrated promising results in non-invasively estimating  $FFR_{CT}$ . In efforts to decrease the computational time, accordingly to the results obtained, adopting steady-state simulations over transient ones is recommended. Both patients with mild to severe degrees of stenosis have been included in this work. A strong agreement was observed when comparing  $FFR_{CT}$  values with iFFR for patients with measurement performed in the RCA, but further investigations are necessary for patients who had a stenosis in the LAD. While the preliminary results are positive, the impact of different parameters (i.e. TCRI, viscosity, intramyocardial pressure ...) requires further exploration. Future research should be conducted with a wider range of patients.





# Bibliography

- [1] 3dslicer. URL <https://www.slicer.org/>.
- [2] Heartflow. URL <https://www.heartflow.com/>.
- [3] *Coronary artery disease therapeutics and drug discovery*. Advances in Experimental Medicine and Biology, v. 1177. Springer, Singapore, 2020. ISBN 9789811525179.
- [4] K. M. Abdelrahman, M. Y. Chen, A. K. Dey, R. Virmani, A. V. Finn, R. Y. Khamis, A. D. Choi, J. K. Min, M. C. Williams, A. J. Buckler, C. A. Taylor, C. Rogers, H. Samady, C. Antoniadis, L. J. Shaw, M. J. Budoff, U. Hoffmann, R. Blankstein, J. Narula, and N. N. Mehta. Coronary computed tomography angiography from clinical uses to emerging technologies: Jacc state-of-the-art review, 9 2020. ISSN 15583597.
- [5] R. K. Banerjee, L. H. Back, M. R. Back, and Y. I. Cho. Physiological flow simulation in residual human stenoses after coronary angioplasty. *J. Biomech. Eng.*, 122(4):310–320, 2000.
- [6] E. Boileau, S. Pant, C. Roobottom, I. Sazonov, J. Deng, X. Xie, and P. Nithiarasu. Estimating the accuracy of a reduced-order model for the calculation of fractional flow reserve (ffr). *International journal for numerical methods in biomedical engineering*, 34(1):e2908, 2018.
- [7] C. W. A. P. Carlos. The cardiovascular system and associated disorders, 2022.
- [8] V. Carvalho, D. Pinho, R. A. Lima, J. C. Teixeira, and S. Teixeira. Blood flow modeling in coronary arteries: A review. *Fluids*, 6(2):53, 2021.
- [9] N. Curzen, Z. Nicholas, B. Stuart, S. Wilding, K. Hill, J. Shambrook, Z. Eminton, D. Ball, C. Barrett, L. Johnson, et al. Fractional flow reserve derived from computed tomography coronary angiography in the assessment and management of stable chest pain: the forecast randomized trial. *European heart journal*, 42(37):3844–3852, 2021.
- [10] I. Danad, P. G. Raijmakers, R. S. Driessen, J. Leipsic, R. Raju, C. Naoum, J. Knuuti, M. Mäki, R. S. Underwood, J. K. Min, et al. Comparison of coronary ct angiography,

- spect, pet, and hybrid imaging for diagnosis of ischemic heart disease determined by fractional flow reserve. *JAMA cardiology*, 2(10):1100–1107, 2017.
- [11] B. De Bruyne, N. H. Pijls, B. Kalesan, E. Barbato, P. A. Tonino, Z. Piroth, N. Jagic, S. Möbius-Winkler, G. Rioufol, N. Witt, et al. Fractional flow reserve–guided pci versus medical therapy in stable coronary disease. *New England Journal of Medicine*, 367(11):991–1001, 2012.
- [12] G. de Simone, M. J. Roman, M. J. Koren, G. A. Mensah, A. Ganau, and R. B. Devereux. Stroke volume/pulse pressure ratio and cardiovascular risk in arterial hypertension. *Hypertension*, 33(3):800–805, 1999.
- [13] M. Diodato and E. G. Chedrawy. Coronary artery bypass graft surgery: the past, present, and future of myocardial revascularisation. *Surgery research and practice*, 2014, 2014.
- [14] D. Du Bois. A formula to estimate the approximate surface area if height and weight be known. 1916. *Nutrition*, 5(5):312–313, 1989.
- [15] T. Edvardsen, F. M. Asch, B. Davidson, V. Delgado, A. DeMaria, V. Dilsizian, O. Gaemperli, M. J. Garcia, O. Kamp, D. C. Lee, et al. Non-invasive imaging in coronary syndromes: recommendations of the european association of cardiovascular imaging and the american society of echocardiography, in collaboration with the american society of nuclear cardiology, society of cardiovascular computed tomography, and society for cardiovascular magnetic resonance. *European Heart Journal-Cardiovascular Imaging*, 23(2):e6–e33, 2022.
- [16] P. Eslami, V. Thondapu, J. Karady, E. M. Hartman, Z. Jin, M. Albaghdadi, M. Lu, J. J. Wentzel, and U. Hoffmann. Physiology and coronary artery disease: emerging insights from computed tomography imaging based computational modeling. *The international journal of cardiovascular imaging*, 36:2319–2333, 2020.
- [17] W. F. Fearon, P. A. Tonino, B. De Bruyne, U. Siebert, N. H. Pijls, F. S. Investigators, et al. Rationale and design of the fractional flow reserve versus angiography for multivessel evaluation (fame) study. *American heart journal*, 154(4):632–636, 2007.
- [18] A. Fedorov, R. Beichel, J. Kalpathy-Cramer, J. Finet, J.-C. Fillion-Robin, S. Pujol, C. Bauer, D. Jennings, F. Fennessy, M. Sonka, et al. 3d slicer as an image computing platform for the quantitative imaging network. *Magnetic resonance imaging*, 30(9):1323–1341, 2012.
- [19] S. Fezzi, J. Huang, M. Lunardi, D. Ding, F. Ribichini, S. Tu, and W. Wijns. Coronary

- physiology in the catheterisation laboratory: An a to z practical guide. *AsiaIntervention*, 8:86–109, 2022.
- [20] D. H. Fitchett, M. Gupta, M. E. Farkouh, and S. Verma. Coronary artery revascularization in patients with diabetes mellitus. *Circulation*, 130(12):e104–e106, 2014.
- [21] G. Gajanan, S. Samant, C. Hovseth, and Y. S. Chatzizisis. Case report: Invasive and non-invasive hemodynamic assessment of coronary artery disease: Strengths and weaknesses. *Frontiers in Cardiovascular Medicine*, 9, 4 2022. ISSN 2297055X. doi: 10.3389/fcvm.2022.885249.
- [22] I. C. Glenn, G. M. Iacona, and A. A. Mangi. Percutaneous coronary intervention with stenting versus coronary artery bypass grafting in stable coronary artery disease. *International Journal of Angiology*, 30(03):221–227, 2021.
- [23] G. R. Heyndrickx and G. G. Tóth. The fame trials: impact on clinical decision making. *Interventional Cardiology Review*, 11(2):116, 2016.
- [24] K. Johnson, P. Sharma, and J. Oshinski. Coronary artery flow measurement using navigator echo gated phase contrast magnetic resonance velocity mapping at 3.0 t. *Journal of biomechanics*, 41(3):595–602, 2008.
- [25] S. E. H. Kathryn L. McCance. 8th edition edition, 2018. ISBN 9780323402804.
- [26] N. Katopodes. Vorticity dynamics. *Free-Surface Flow*, pages 516–565, 2019.
- [27] H. Kawashima, G. Pompilio, D. Andreini, A. L. Bartorelli, S. Mushtaq, E. Ferrari, F. Maisano, R. R. Buechel, K. Tanaka, M. La Meir, J. De Mey, U. Schneider, T. Doenst, U. Teichgräber, G. W. Stone, F. Sharif, R. de Winter, B. Thomsen, C. Taylor, C. Rogers, J. Leipsic, W. Wijns, Y. Onuma, and P. W. Serruys. Safety and feasibility evaluation of planning and execution of surgical revascularisation solely based on coronary cta and ffrc in patients with complex coronary artery disease: study protocol of the fasttrack cabg study. *BMJ Open*, 10(12), 2020. ISSN 2044-6055. doi: 10.1136/bmjopen-2020-038152. URL <https://bmjopen.bmj.com/content/10/12/e038152>.
- [28] N. Kawel-Boehm, S. J. Hetzel, B. Ambale-Venkatesh, G. Captur, C. J. Francois, M. Jerosch-Herold, M. Salerno, S. D. Teague, E. Valsangiacomo-Buechel, R. J. van der Geest, and D. A. Bluemke. Reference ranges (“normal values”) for cardiovascular magnetic resonance (cmr) in adults and children: 2020 update. *Journal of Cardiovascular Magnetic Resonance*, 22, 12 2020. ISSN 1532429X. doi: 10.1186/s12968-020-00683-3.

- [29] H. J. Kim, I. Vignon-Clementel, J. Coogan, C. Figueroa, K. Jansen, and C. Taylor. Patient-specific modeling of blood flow and pressure in human coronary arteries. *Annals of biomedical engineering*, 38:3195–3209, 2010.
- [30] P. Knaapen. Computed tomography to replace invasive coronary angiography?: Close, but not close enough, 2 2019. ISSN 19420080.
- [31] B.-K. Koo, A. Erglis, J.-H. Doh, D. V. Daniels, S. Jegere, H.-S. Kim, A. Dunning, T. DeFrance, A. Lansky, J. Leipsic, et al. Diagnosis of ischemia-causing coronary stenoses by noninvasive fractional flow reserve computed from coronary computed tomographic angiograms: results from the prospective multicenter discover-flow (diagnosis of ischemia-causing stenoses obtained via noninvasive fractional flow reserve) study. *Journal of the American College of Cardiology*, 58(19):1989–1997, 2011.
- [32] M. Kruk, Ł. Wardziak, M. Demkow, W. Pleban, J. Pręgowski, Z. Dzielińska, M. Witulski, A. Witkowski, W. Rużyło, and C. Kępką. Workstation-based calculation of cta-based ffr for intermediate stenosis. *JACC: Cardiovascular Imaging*, 9(6):690–699, 2016.
- [33] S. S. Kwon, E. C. Chung, J. S. Park, G. T. Kim, J. W. Kim, K. H. Kim, E. S. Shin, and E. B. Shim. A novel patient-specific model to compute coronary fractional flow reserve. *Progress in Biophysics and Molecular Biology*, 116:48–55, 9 2014. ISSN 00796107. doi: 10.1016/j.pbiomolbio.2014.09.003.
- [34] J. S. Lawton, J. E. Tamis-Holland, S. Bangalore, E. R. Bates, T. M. Beckie, J. M. Bischoff, J. A. Bittl, M. G. Cohen, J. M. DiMaio, C. W. Don, S. E. Fremes, M. F. Gaudino, Z. D. Goldberger, M. C. Grant, J. B. Jaswal, P. A. Kurlansky, R. Mehran, T. S. Metkus, L. C. Nnacheta, S. V. Rao, F. W. Sellke, G. Sharma, C. M. Yong, and B. A. Zwischenberger. 2021 acc/aha/scai guideline for coronary artery revascularization: A report of the american college of cardiology/american heart association joint committee on clinical practice guidelines. *Journal of the American College of Cardiology*, 79:e21–e129, 1 2022. ISSN 15583597. doi: 10.1016/j.jacc.2021.09.006.
- [35] H. Liu, A. Wingert, J. Wang, J. Zhang, X. Wang, J. Sun, F. Chen, S. G. Khalid, J. Jiang, and D. Zheng. Extraction of coronary atherosclerotic plaques from computed tomography imaging: A review of recent methods. *Frontiers in Cardiovascular Medicine*, 8, 2021. ISSN 2297055X. doi: 10.3389/fcvm.2021.597568.
- [36] J. Liu, X. Wang, B. Li, S. Huang, H. Sun, L. Zhang, Y. Sun, Z. Liu, J. Liu, L. Wang, et al. Non-invasive quantification of fraction flow reserve based on steady-state geometric multiscale models. *Frontiers in Physiology*, page 690, 2022.

- [37] X. Liu, C. Xu, S. Rao, Y. Zhang, D. Ghista, Z. Gao, and G. Yang. Physiologically personalized coronary blood flow model to improve the estimation of noninvasive fractional flow reserve. *Medical Physics*, 49(1):583–597, 2022.
- [38] E. W. Lo, L. J. Menezes, and R. Torii. Impact of inflow boundary conditions on the calculation of ct-based ffr. *Fluids*, 4(2):60, 2019.
- [39] E. W. Lo, L. J. Menezes, and R. Torii. On outflow boundary conditions for ct-based computation of ffr: Examination using pet images. *Medical Engineering & Physics*, 76:79–87, 2020.
- [40] A. K. Malakar, D. Choudhury, B. Halder, P. Paul, A. Uddin, and S. Chakraborty. A review on coronary artery disease, its risk factors, and therapeutics. *Journal of cellular physiology*, 234(10):16812–16823, 2019.
- [41] F. H. Martini. *Anatomia umana / Frederic H. Martini, Michael J. Timmons, Robert B. Tallitsch ; con William C. Ober ... [et al.] ; revisione a cura di Lucio Cocco ... [et al.]*. EdiSES, Napoli, 5. ed edition, 2012. ISBN 9788879597302.
- [42] J. K. Min, J. Leipsic, M. J. Pencina, D. S. Berman, B.-K. Koo, C. Van Mieghem, A. Erglis, F. Y. Lin, A. M. Dunning, P. Apruzzese, et al. Diagnostic accuracy of fractional flow reserve from anatomic ct angiography. *Jama*, 308(12):1237–1245, 2012.
- [43] J. K. Min, C. A. Taylor, S. Achenbach, B. K. Koo, J. Leipsic, B. L. Nørgaard, N. J. Pijls, and B. De Bruyne. Noninvasive fractional flow reserve derived from coronary ct angiography: clinical data and scientific principles. *Cardiovascular Imaging*, 8(10):1209–1222, 2015.
- [44] P. D. Morris, D. A. S. Soto, J. F. Feher, D. Rafiroiu, A. Lungu, S. Varma, P. V. Lawford, D. R. Hose, and J. P. Gunn. Fast virtual fractional flow reserve based upon steady-state computational fluid dynamics analysis results from the virtu-fast study, 2017.
- [45] L. O. Müller, F. E. Fossan, A. T. Bråten, A. Jørgensen, R. Wiseth, and L. R. Hellevik. Impact of baseline coronary flow and its distribution on fractional flow reserve prediction. *International journal for numerical methods in biomedical engineering*, 37(11):e3246, 2021.
- [46] C. D. Murray. The physiological principle of minimum work: Ii. oxygen exchange in capillaries. *Proceedings of the National Academy of Sciences*, 12(5):299–304, 1926.
- [47] P. I. Ngam, C. C. Ong, P. Chai, S. S. Wong, C. R. Liang, and L. L. San Teo.

- Computed tomography coronary angiography—past, present and future. *Singapore medical journal*, 61(3):109, 2020.
- [48] B. L. Nørgaard, J. Leipsic, S. Gaur, S. Seneviratne, B. S. Ko, H. Ito, J. M. Jensen, L. Mauri, B. De Bruyne, H. Bezerra, et al. Diagnostic performance of noninvasive fractional flow reserve derived from coronary computed tomography angiography in suspected coronary artery disease: the next trial (analysis of coronary blood flow using ct angiography: Next steps). *Journal of the American College of Cardiology*, 63(12): 1145–1155, 2014.
- [49] M. R. Patel, B. L. Nørgaard, T. A. Fairbairn, K. Nieman, T. Akasaka, D. S. Berman, G. L. Raff, L. M. Hurwitz Koweek, G. Pontone, T. Kawasaki, et al. 1-year impact on medical practice and clinical outcomes of ffrc: the advance registry. *Cardiovascular Imaging*, 13(1\_Part\_1):97–105, 2020.
- [50] N. H. Pijls and B. De Bruyne. *Coronary pressure*, volume 195. Springer Science & Business Media, 2013.
- [51] N. H. Pijls, B. Van Gelder, P. Van der Voort, K. Peels, F. A. Bracke, H. J. Bonnier, and M. I. El Gamal. Fractional flow reserve: a useful index to evaluate the influence of an epicardial coronary stenosis on myocardial blood flow. *Circulation*, 92(11): 3183–3193, 1995.
- [52] N. H. Pijls, B. de Bruyne, K. Peels, P. H. van der Voort, H. J. Bonnier, J. Bartunek, and J. J. Koolen. Measurement of fractional flow reserve to assess the functional severity of coronary-artery stenoses. *New England Journal of Medicine*, 334(26): 1703–1708, 1996.
- [53] R. Prajapati, P. Patel, and U. Upadhyay. A review on coronary artery disease. 2021.
- [54] S. Rehman, A. Khan, and A. Rehman. Physiology, coronary circulation. In *StatPearls [Internet]*. StatPearls Publishing, 2021.
- [55] S. Sakamoto, S. Takahashi, A. U. Coskun, M. I. Papafaklis, A. Takahashi, S. Saito, P. H. Stone, and C. L. Feldman. Relation of distribution of coronary blood flow volume to coronary artery dominance. *The American journal of cardiology*, 111(10): 1420–1424, 2013.
- [56] S. Sankaran, M. Esmaily Moghadam, A. M. Kahn, E. E. Tseng, J. M. Guccione, and A. L. Marsden. Patient-specific multiscale modeling of blood flow for coronary artery bypass graft surgery. *Annals of biomedical engineering*, 40:2228–2242, 2012.
- [57] S. Sankaran, H. J. Kim, G. Choi, and C. A. Taylor. Uncertainty quantification in

- coronary blood flow simulations: impact of geometry, boundary conditions and blood viscosity. *Journal of biomechanics*, 49(12):2540–2547, 2016.
- [58] P. W. Serruys, H. Hara, S. Garg, H. Kawashima, B. L. Nørgaard, M. R. Dweck, J. J. Bax, J. Knuuti, K. Nieman, J. A. Leipsic, S. Mushtaq, D. Andreini, and Y. Onuma. Coronary computed tomographic angiography for complete assessment of coronary artery disease: Jacc state-of-the-art review, 8 2021. ISSN 15583597.
- [59] P. Sharma, L. Itu, X. Zheng, A. Kamen, D. Bernhardt, C. Suci, and D. Comaniciu. A framework for personalization of coronary flow computations during rest and hyperemia. pages 6665–6668, 2012. ISBN 9781424441198. doi: 10.1109/EMBC.2012.6347523.
- [60] Y. Shi, J. Zheng, N. Yang, Y. Chen, J. Sun, Y. Zhang, X. Zhou, Y. Gao, S. Li, H. Zhu, J. Acosta-Cabronero, P. Xia, and Z. Teng. The effect of subbranch for the quantification of local hemodynamic environment in the coronary artery: A computed tomography angiography-based computational fluid dynamic analysis. *Emergency and Critical Care Medicine*, 2:181–190, 12 2022. ISSN 2693860X. doi: 10.1097/EC9.000000000000062.
- [61] M. Solecki, M. Kruk, M. Demkow, U. J. Schoepf, M. A. Reynolds, Ł. Wardziak, Z. Dzielińska, M. Śpiewak, B. Miłosz-Wieczorek, Ł. Małek, et al. What is the optimal anatomic location for coronary artery pressure measurement at ct-derived ffr? *Journal of Cardiovascular Computed Tomography*, 11(5):397–403, 2017.
- [62] F. Tajeddini, M. R. Nikmaneshi, B. Firoozabadi, H. A. Pakravan, S. H. Ahmadi Tafti, and H. Afshin. High precision invasive ffr, low-cost invasive ifr, or non-invasive cfr?: optimum assessment of coronary artery stenosis based on the patient-specific computational models. *International Journal for Numerical Methods in Biomedical Engineering*, 36(10):e3382, 2020.
- [63] A. Tang. *Establishing the Clinical Feasibility of a Transparent Computed-Tomography Based Fractional Flow Reserve (CT-FFR) Algorithm*. PhD thesis, 2018.
- [64] C. X. Tang, C. Y. Liu, M. J. Lu, U. J. Schoepf, C. Tesche, R. R. Bayer, H. T. Hudson, X. L. Zhang, J. H. Li, Y. N. Wang, C. S. Zhou, J. Y. Zhang, M. M. Yu, Y. Hou, M. W. Zheng, B. Zhang, D. M. Zhang, Y. Yi, Y. Ren, C. W. Li, X. Zhao, G. M. Lu, X. H. Hu, L. Xu, and L. J. Zhang. Ct ffr for ischemia-specific cad with a new computational fluid dynamics algorithm: A chinese multicenter study. *JACC: Cardiovascular Imaging*, 13:980–990, 4 2020. ISSN 18767591. doi: 10.1016/j.jcmg.2019.06.018.
- [65] C. A. Taylor, T. A. Fonte, and J. K. Min. Computational fluid dynamics applied

to cardiac computed tomography for noninvasive quantification of fractional flow reserve: Scientific basis. *Journal of the American College of Cardiology*, 61:2233–2241, 6 2013. ISSN 15583597. doi: 10.1016/j.jacc.2012.11.083.

- [66] P. A. Tonino, W. F. Fearon, B. De Bruyne, K. G. Oldroyd, M. A. Leesar, P. N. Ver Lee, P. A. MacCarthy, M. Van’t Veer, and N. H. Pijls. Angiographic versus functional severity of coronary artery stenoses in the fame study: fractional flow reserve versus angiography in multivessel evaluation. *Journal of the American College of Cardiology*, 55(25):2816–2821, 2010.
- [67] R. Torii and M. H. Yacoub. Ct-based fractional flow reserve: Development and expanded application. *Global Cardiology Science and Practice*, 2021, 10 2021. ISSN 23057823. doi: 10.21542/gcsp.2021.20.
- [68] N. G. Uren, J. A. Melin, B. De Bruyne, W. Wijns, T. Baudhuin, and P. G. Camici. Relation between myocardial blood flow and the severity of coronary-artery stenosis. *New England Journal of Medicine*, 330(25):1782–1788, 1994.
- [69] I. E. Vignon-Clementel, C. Figueroa, K. Jansen, and C. Taylor. Outflow boundary conditions for 3d simulations of non-periodic blood flow and pressure fields in deformable arteries. *Computer methods in biomechanics and biomedical engineering*, 13(5):625–640, 2010.
- [70] T. Vos, A. A. Abajobir, K. H. Abate, C. Abbafati, K. M. Abbas, F. Abd-Allah, R. S. Abdulkader, A. M. Abdulle, T. A. Abebo, S. F. Abera, et al. Global, regional, and national incidence, prevalence, and years lived with disability for 328 diseases and injuries for 195 countries, 1990–2016: a systematic analysis for the global burden of disease study 2016. *The Lancet*, 390(10100):1211–1259, 2017.
- [71] N. Westerhof, J.-W. Lankhaar, and B. E. Westerhof. The arterial windkessel. *Medical & biological engineering & computing*, 47(2):131–141, 2009.
- [72] WHO. World health organization, cardiovascular diseases. URL <https://www.who.int/health-topics/cardiovascular-diseases>.
- [73] R. F. Wilson, K. Wyche, B. V. Christensen, S. Zimmer, and D. D. Laxson. Effects of adenosine on human coronary arterial circulation. *Circulation*, 82(5):1595–1606, 1990.
- [74] X. Wu, B. Wu, W. He, X. Wang, K. Wang, Z. Yan, Z. Cheng, Y. Huang, W. Zhang, R. Chen, J. Liu, . J. Wang, and X. Hu. Expanding the coronary



- tree reconstruction to smaller arteries improves the accuracy of ffr ct. 2021. doi: 10.1007/s00330-021-08012-7/Published.
- [75] X. Xi, J. Liu, H. Sun, K. Xu, X. Wang, L. Zhang, T. Du, J. Liu, and B. Li. Accurate calculation of ffr based on a physics-driven fluid-structure interaction model. *Frontiers in Physiology*, page 684, 2022.
- [76] X. Xue, X. Liu, Z. Gao, R. Wang, L. Xu, D. Ghista, and H. Zhang. Personalized coronary blood flow model based on ct perfusion to non-invasively calculate fractional flow reserve. *Computer Methods in Applied Mechanics and Engineering*, 404:115789, 2023.
- [77] M. Yin, A. Yazdani, and G. E. Karniadakis. One-dimensional modeling of fractional flow reserve in coronary artery disease: Uncertainty quantification and bayesian optimization. *Computer Methods in Applied Mechanics and Engineering*, 353:66–85, 2019.
- [78] J. M. Zhang, L. Zhong, B. Su, M. Wan, J. S. Yap, J. P. Tham, L. P. Chua, D. N. Ghista, and R. S. Tan. Perspective on cfd studies of coronary artery disease lesions and hemodynamics: A review. *International Journal for Numerical Methods in Biomedical Engineering*, 30:659–680, 2014. ISSN 20407947. doi: 10.1002/cnm.2625.
- [79] L. Zhong, J.-M. Zhang, B. Su, R. S. Tan, J. C. Allen, and G. S. Kassab. Application of patient-specific computational fluid dynamics in coronary and intra-cardiac flow simulations: Challenges and opportunities. *Frontiers in physiology*, 9:742, 2018.



# A | Appendix A

Authors	Imaging	Geometry	Steady/ Transient	Inlet BC	Outlet BC	Indexes
<i>Kim et al., 2010 [29]</i> (1)	CCTA	Model of the heart and arterial system	Transient	Inflow BC coupling the heart and a closed loop model	Upper branch vessels and thoracic aorta: WK3 Coronary outlets: RCRCR+Pmyo	WSS
<i>Taylor et al., 2012 [65]</i> (1)	CCTA	Aorta+LCA+RCA Idealized	Idealized: steady Patient-specific: transient	LPM of the heart	Aorta outlet: WK3 Coronary outlet: RCRCR+Pmyo Pv: 0mmHg	FFR, $FFR_{CT}$
<i>Kwon et al., 2014[33]</i> (3)	CCTA	Aorta+LCA+RCA RCA/LCA alone Idealized	Transient	LCA/RCA simulation: Pao waveform based on patient's HR, SBP, DBP Model with the aorta: inlet flow-rate	Aorta outlet: Pao Coronary outlets: RCRCR+Pmyo Pv: 0mmHg	FFR, $FFR_{CT}$ WSS
<i>Sankaran et al., 2016[57]</i> (1)	CCTA	Aorta+LCA+RCA Idealized	Idealized: steady Patient-specific: transient	Idealized: Pao Patient-specific:paraboli velocity profile	Resistance model	$FFR_{CT}$ + impact of MLD, LL, R, viscosity
<i>Lo et al., 2019[38]</i> (7)	CCTA	Aorta+LCA+RCA	Quasi-steady + transient	4 different flow-rates: steady, pulsatile patient-specific, population average	2WK (transient) R (quasi-steady) Pmyo in LAD Pv: 0mmHg	FFR,iFR baseline Pd/Pa

<i>Yin et al., 2019[77]</i> (8)	3D model from an open source imaging repository	3D-0D 1D-0D	Aorta+LCA+RCA	Transient	Patient-specific flow waveform	RCRCR+Pmyo Pv: 0mmHg	$FFR_{CT}$
	<i>Tang et al., 2020[64]</i> (10)	CCTA	3D-0D 1D-0D	Aorta+LCA+RCA	Steady	MAP Hyperemia: $Phyp = 0.8 \cdot P_{rest}$	R FFR, $FFR_{CT}$
<i>Lo et al., 2020[39]</i> (7)	CCTA	3D-0D	Aorta+LCA+RCA	Steady	Patient-specific steady inflow	2WK	FFR
<i>Wu et al., 2021[74]</i> (13)	CCTA	3D-0D	Aorta+LCA+RCA	Transient	Patient-specific inflow	Resistive model [69]	FFR, $FFR_{CT}$
<i>Liu et al., 2022[36]</i> (14)	CCTA	3D-0D	Aorta+LCA+RCA	Steady	$MAP = DBP + [1/3 + (HR \cdot 0.0012)] \cdot (SBP - DBP)$	RL	FFR, $FFR_{CT}$

Table A.1: Authors using a model comprising Aorta, LCA and RCA. The subscripts denote which works belong to the same research group. (Pmyo: intramyocardial pressure, Pv: venous pressure, OSI:oscillatory shear index, TAWSS: time-average wall shear stress, RRT: relative resistance time, TAP: time-average pressure).

Authors	Imaging	Geometry	Steady/ Transient	Inlet BC	Outlet BC	Indexes
<i>Sharma et al., 2012[59]</i> (2)	CCTA	LAD	Steady	$MAP = DBP + [1/3 + (HR \cdot 0.0012)] \cdot (SBP - DBP)$	R	$FFR_{CT}$
<i>Kwon et al., 2014[53]</i> (3)	CCTA	Aorta+LCA+RCA RCA/LCA alone Idealized	Transient	LCA/RCA simulation: Pao waveform based on patient's HR, SBP, DBF Model with the aorta: inlet flow-rate	Aorta outlet: Pao Coronary outlets: RCRCR+Pmyo Pv: 0mmHg	$FFR, FFR_{CT}$ WSS
<i>Boileau et al., 2017[6]</i> (4)	CCTA	LAD with artificial stenosis	Transient	Flow waveform	RCRCR+Pmyo Pv: 5mmHg	$FFR_{CT}$
<i>Morris et al., 2017[44]</i> (5)	Angiography	Vessel of interest	Pseudo-transient	Patient-specific pressure invasively measured	R	$FFR, vFFR$
<i>Tang et al., 2018[63]</i> (6)	CCTA	LCA/RCA	Steady	$MAP = SBP/3 + 2 \cdot DBP/3$	R	$FFR, FFR_{CT}$ ESS
<i>Muller et al., 2019[45]</i> (9)	CCTA	LCA/RCA	Steady	Pressure	Prescribed flow-rate or resistive elements	$FFR, FFR_{CT}$
<i>Tajeddini et al., 2020[62]</i> (11)	CCTA	LAD/LCX	Transient	Pao waveform	RCRCR+Pmyo	$FFR_{CT}, iFR$ CFR+influence LL, MLD, D% +WSS, OSI, TAWSS, RRT
<i>Liu et al., 2021[37]</i> (12)	CCTA	LCA/RCA	Steady	$MAP = 0.4 \cdot (SBP - DBP) + DBP$	R	$FFR, FFR_{CT}$

	CCTA	FSI-0D	Vessel of interest	Transient	Pao waveform	RLC	FFR, $FFR_{CT}$
<i>Xi et al., 2022[75]</i> <sup>(14)</sup>				Transient	Pao waveform	RLC	FFR, $FFR_{CT}$
<i>Shi et al., 2022[60]</i> <sup>(15)</sup>	CCTA	3D-0D	LCA	Transient	Pressure waveform	Time dependent blood flow	TAP, TAWSS OSI, RRT
<i>Xue et al., 2023[76]</i> <sup>(12)</sup>	CCTA	3D-0D	LCA/RCA	Steady	$MAP = 0.4 \cdot (SBP - DBP) + DBP$	R Pv: 5mmHg	FFR, $FFR_{CT}$

Table A.2: Authors using a more simplified model without the aorta. The subscripts denote which works belong to the same research group. (Pmyo: intramyocardial pressure, Pv: venous pressure, OSI: oscillatory shear index, TAWSS: time-average wall shear stress, RRT: relative resistance time, TAP: time-average pressure).

Authors	Imaging	Geometry	Steady/ Transient	Inlet BC	Outlet BC	Indexes
<i>Taylor et al., 2012 [65]</i> (1)	CCTA	Aorta+LCA+RCA Idealized	Idealized: steady Patient-specific: transient	LPM of the heart	Aorta outlet: WK3 Coronary outlet: RCRCR+Pmyo Pv: 0mmHg	FFR, $FFR_{CT}$
<i>Kwon et al., 2014[33]</i> (3)	CCTA	Aorta+LCA+RCA RCA/LCA alone Idealized	Transient	LCA/RCA simulation: Pao waveform based on patient's HR, SBP, DBF Model with the aorta: inlet flow-rate	Aorta outlet: Pao Coronary outlets: RCRCR+Pmyo Pv: 0mmHg	FFR, $FFR_{CT}$ WSS
<i>Boileau et al., 2017[6]</i> (4)	CCTA	LAD with artificial stenosis	Transient	Flow waveform	RCRCR+Pmyo Pv: 5mmHg	$FFR_{CT}$
<i>Morris et al., 2017[44]</i> (5)	Angiography	Vessel of interest	Pseudo-transient	Patient-specific pressure invasively measured	R	FFR, vFFR
<i>Tang et al., 2018[63]</i> (6)	CCTA	LCA/RCA	Steady	$MAP =$ $SBP/3 + 2 \cdot DBP/3$	R	FFR, $FFR_{CT}$ ESS
<i>Lo et al., 2019[38]</i> (7)	CCTA	Aorta+LCA+RCA	Quasi-steady + transient	4 different flow-rates: steady, pulsatile patient-specific, population average	2WK (transient) R (quasi-steady) Pmyo in LAD Pv: 0mmHg	FFR, iFR baseline Pd/Pa
<i>Muller et al., 2019[45]</i> (9)	CCTA	LCA/RCA	Steady	Pressure	Prescribed flow-rate or resistive elements	FFR, $FFR_{CT}$



<i>Tang et al., 2020[64]</i> (10)	CCTA	3D-0D 1D-0D	Aorta+LCA+RCA	Steady	MAP Hyperemia: $P_{hyp} = 0.8 \cdot P_{rest}$	R	FFR, FFR <sub>CT</sub>
<i>Lo et al., 2020[39]</i> (7)	CCTA	3D-0D	Aorta+LCA+RCA	Steady	Patient-specific steady inflow	WK2	FFR
<i>Liu et al., 2021[37]</i> (12)	CCTA	3D-0D	LCA/RCA	Steady	$MAP = 0.4 \cdot (SBP - DBP) + DBP$	R	FFR, FFR <sub>CT</sub>
<i>Wu et al., 2021[74]</i> (13)	CCTA	3D-0D	Aorta+LCA+RCA	Transient	Patient-specific inflow	Resistive model [69]	FFR, FFR <sub>CT</sub>
<i>Liu et al., 2022[36]</i> (14)	CCTA	3D-0D	Aorta+LCA+RCA	Steady	$MAP = DBP + [1/3 + (HR \cdot 0.0012)] \cdot (SBP - DBP)$	RL	FFR, FFR <sub>CT</sub>
<i>Xi et al., 2022[75]</i> (14)	CCTA	FSI-0D	Vessel of interest	Transient	Pao waveform	RLC	FFR, FFR <sub>CT</sub>
<i>Xue et al., 2023[76]</i> (12)	CCTA	3D-0D	LCA/RCA	Steady	$MAP = 0.4 \cdot (SBP - DBP) + DBP$	R Pv: 5mmHg	FFR, FFR <sub>CT</sub>

Table A.3: Works in which a comparison of FFR<sub>CT</sub> against iFFR have been performed. The subscripts denote which works belong to the same research group. (Pmyo: intramyocardial pressure, Pv: venous pressure, OSI: oscillatory shear index, TAWSS: time-average wall shear stress, RRT: relative resistance time, TAP: time-average pressure).

Authors	Imaging	Geometry	Steady/ Transient	Inlet BC	Outlet BC	Indexes
<i>Sharma et al., 2012[59]</i> (2)	CCTA	3D-0D LAD	Steady	$MAP = DBP + [1/3 + (HR \cdot 0.0012)] \cdot (SBP - DBP)$	R	$FFR_{CT}$
<i>Tang et al., 2018[63]</i> (6)	CCTA	3D-0D LCA/RCA	Steady	$MAP = SBP/3 + 2 \cdot DBP/3$	R	$FFR, FFR_{CT}$ ESS
<i>Lo et al., 2019[38]</i> (7)	CCTA	3D-0D Aorta+LCA+RCA	Quasi-steady + transient	4 different flow-rates: steady, pulsatile patient-specific, population average	2WK (transient) R (quasi-steady) Pmyo in LAD Pv: 0mmHg	$FFR, iFR$ baseline Pd/Pa
<i>Muller et al., 2019[45]</i> (9)	CCTA	3D-0D 1D-0D LCA/RCA	Steady	Pressure	Prescribed flow-rate or resistive elements	$FFR, FFR_{CT}$
<i>Tang et al., 2020[64]</i> (10)	CCTA	3D-0D 1D-0D Aorta+LCA+RCA	Steady	MAP Hyperemia: $Phyp = 0.8 \cdot Prest$	R	$FFR, FFR_{CT}$
<i>Lo et al., 2020[39]</i> (7)	CCTA	3D-0D Aorta+LCA+RCA	Steady	Patient-specific steady inflow	WK2	FFR
<i>Liu et al., 2021[37]</i> (12)	CCTA	3D-0D LCA/RCA	Steady	$MAP = 0.4 \cdot (SBP - DBP) + DBP$	R	$FFR, FFR_{CT}$
<i>Liu et al., 2022[36]</i> (14)	CCTA	3D-0D Aorta+LCA+RCA	Steady	$MAP = DBP + [1/3 + (HR \cdot 0.0012)] \cdot (SBP - DBP)$	RL	$FFR, FFR_{CT}$

<i>Xue et al.</i> , 2023[76]	(12)	CCTA	3D-0D	LCA/RCA	Steady	$MAP = 0.4 \cdot (SBP - DBP) + DBP$	R Pv: 5mmHg	FFR, FFR <sub>CT</sub>
---------------------------------	------	------	-------	---------	--------	-------------------------------------	----------------	------------------------

Table A.4: Analysed works in which a steady-state simulation was used to estimate FFR<sub>CT</sub> value. The subscripts denote which works belong to the same research group. (Pmyo: intramyocardial pressure, Pv: venous pressure, OSI: oscillatory shear index, TAWSS: time-average wall shear stress, RRT: relative resistance time, TAP: time-average pressure).

Authors	Imaging	Geometry	Steady/ Transient	Inlet BC	Outlet BC	Indexes
<i>Kim et al., 2010 [29]</i> <sup>(1)</sup>	CCTA	Model of the heart and arterial system	Transient	Inflow BC coupling the heart and a closed loop model	Upper branch vessels and thoracic aorta: WK3 Coronary outlets: RCRCR+Pmyo	WSS
<i>Taylor et al., 2012 [65]</i> <sup>(1)</sup>	CCTA	Aorta+LCA+RCA Idealized	Idealized: steady Patient-specific: transient	LPM of the heart	Aorta outlet: WK3 Coronary outlet: RCRCR+Pmyo Pv: 0mmHg	FFR, $FFR_{CT}$
<i>Kwon et al., 2014[33]</i> <sup>(3)</sup>	CCTA	Aorta+LCA+RCA RCA/LCA alone Idealized	Transient	LCA/RCA simulation: Pao waveform based on patient's HR, SBP, DBP Model with the aorta: inlet flow-rate	Aorta outlet: Pao Coronary outlets: RCRCR+Pmyo Pv: 0mmHg	FFR, $FFR_{CT}$ WSS
<i>Sankaran et al., 2016[57]</i> <sup>(1)</sup>	CCTA	Aorta+LCA+RCA Idealized	Idealized: steady Patient-specific: transient	Idealized: Pao Patient-specific:paraboli velocity profile	Resistance model	$FFR_{CT}$ + impact of MLD, LL, R, viscosity
<i>Boileau et al., 2017[6]</i> <sup>(4)</sup>	CCTA	LAD with artificial stenosis	Transient	Flow waveform	RCRCR+Pmyo Pv: 5mmHg	$FFR_{CT}$
<i>Morris et al., 2017[44]</i> <sup>(5)</sup>	Angiography	Vessel of interest	Pseudo-transient	Patient-specific pressure invasively measured	R	FFR, vFFR

<i>Lo et al., 2019[38]</i> (7)	CCTA	3D-0D	Aorta+LCA+RCA	Quasi-steady + transient	4 different flow-rates: steady, pulsatile patient-specific, population average	2WK (transient) R (quasi-steady) Pmyo in LAD Pv: 0mmHg	FFR <sub>i</sub> FR baseline Pd/Pa
<i>Yin et al., 2019[77]</i> (8)	3D model from an open source imaging repository	3D-0D 1D-0D	Aorta+LCA+RCA	Transient	Patient-specific flow waveform	RCRCR+Pmyo Pv: 0mmHg	$FFR_{CT}$
<i>Tajeddini et al., 2020[62]</i> (11)	CCTA	3D-0D 1D-0D	LAD/LCX	Transient	Pao waveform	RCRCR+Pmyo	$FFR_{CT}$ , iFR CFR+influence LL, MLD, D% +WSS, OSI, TAWSS, RRT
<i>Wu et al., 2020[74]</i> (13)	CCTA	3D-0D	Aorta+LCA+RCA	Transient	Patient-specific inflow	Resistive model [69]	FFR, $FFR_{CT}$
<i>Xi et al., 2022[75]</i> (14)	CCTA	FSI-0D	Vessel of interest	Transient	Pao waveform	RLC	FFR, $FFR_{CT}$
<i>Shi et al., 2022[60]</i> (15)	CCTA	3D-0D	LCA	Transient	Pressure waveform	Time dependent blood flow	TAP, TAWSS OSI, RRT

Table A.5: Analysed works in which a Transient simulation was used to estimate  $FFR_{CT}$  value. The subscripts denote which works belong to the same research group. (Pmyo: intramyocardial pressure, Pv: venous pressure, OSI: oscillatory shear index, TAWSS: time-average wall shear stress, RRT: relative resistance time, TAP: time-average pressure).



# B | Appendix B

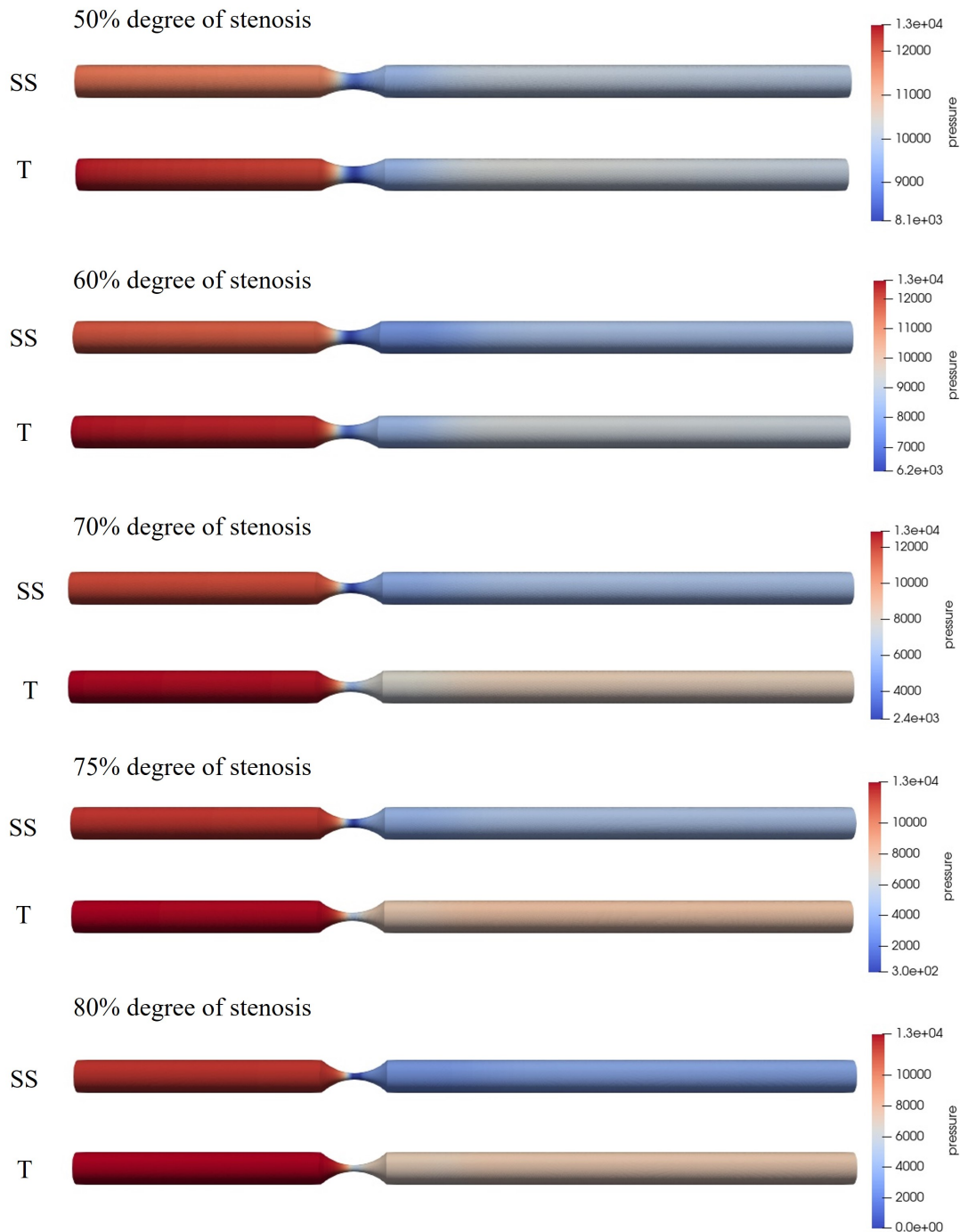


Figure B.1: Pressure field obtained in the idealized geometry with varying degrees of stenosis.



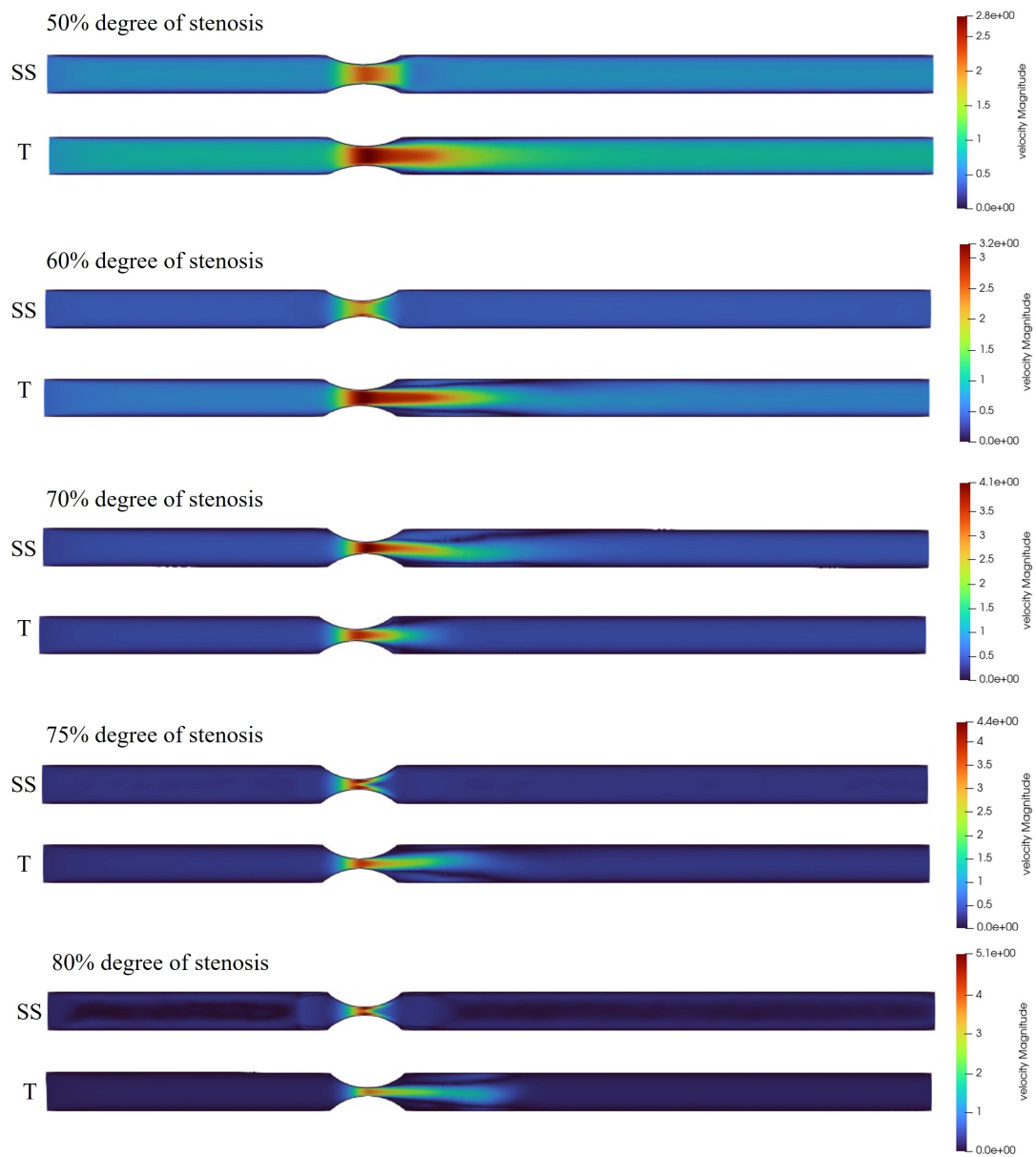


Figure B.2: Velocity field obtained in the idealized geometry with varying degrees of stenosis.

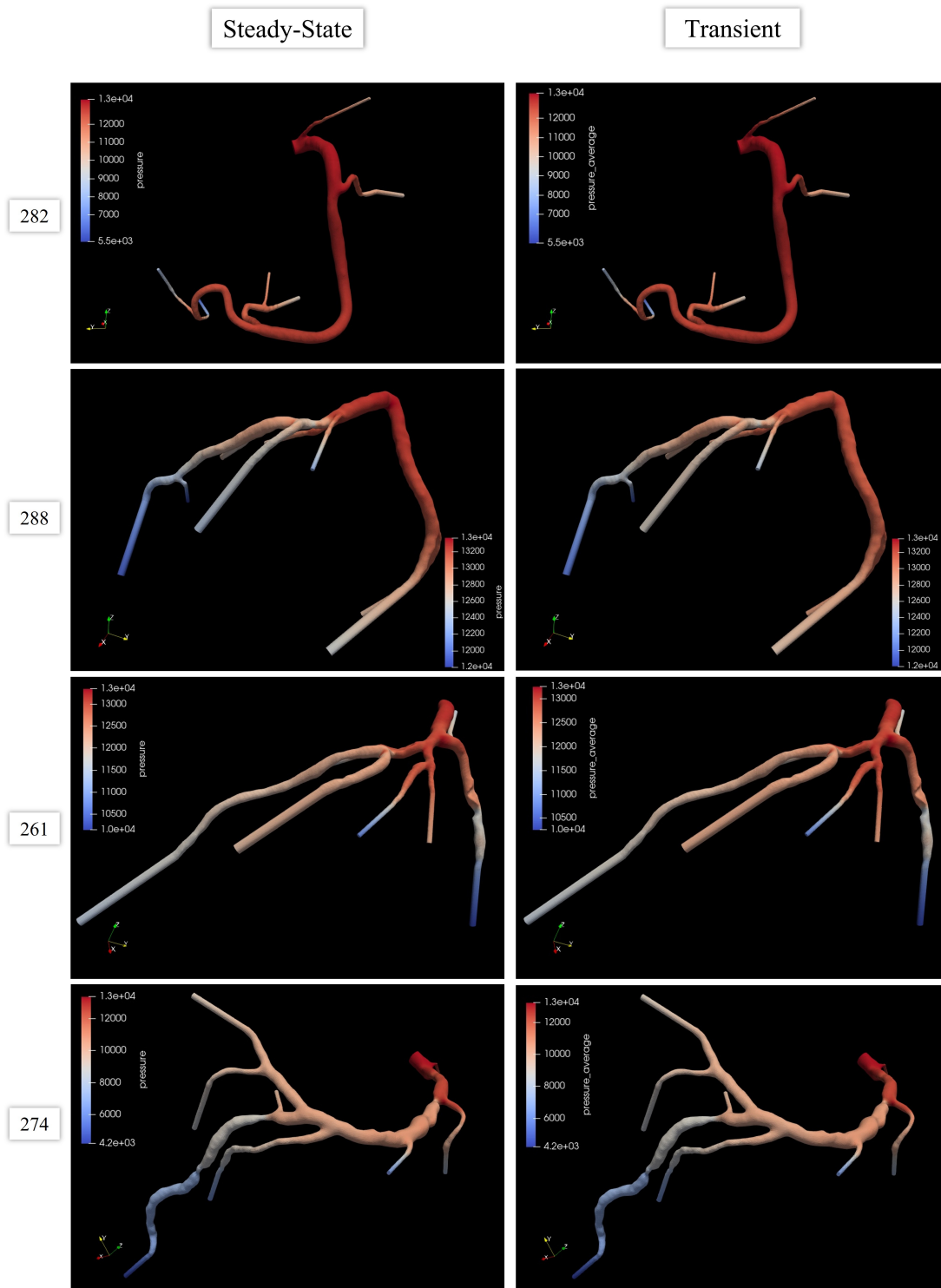


Figure B.3: Pressure field obtained in the patient-specific geometry for the four analysed patients. BCs were derived from average literature data.

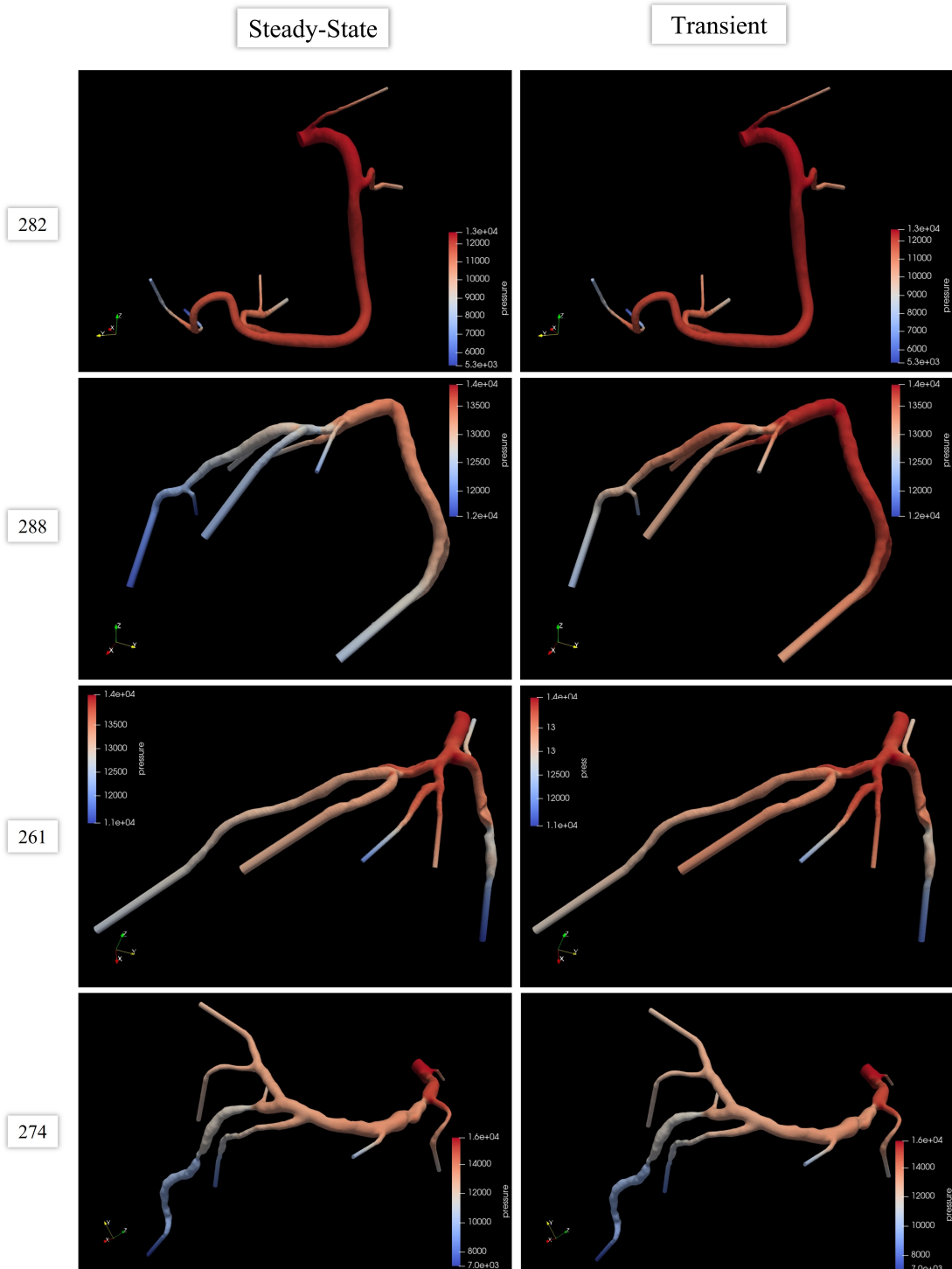


Figure B.4: Pressure field obtained in the patient-specific geometry for the four analysed patients. BCs were derived from the available patient-specific data.



# Acknowledgements

